

1-1-2013

# Chalcogenide Sol-Gel Assembly: Controlling The Kinetics Of Nanocrystal Aggregation And Film Formation For Applications In Optoelectronics

Lasantha Korala  
*Wayne State University,*

Follow this and additional works at: [http://digitalcommons.wayne.edu/oa\\_dissertations](http://digitalcommons.wayne.edu/oa_dissertations)

 Part of the [Science and Mathematics Education Commons](#)

---

## Recommended Citation

Korala, Lasantha, "Chalcogenide Sol-Gel Assembly: Controlling The Kinetics Of Nanocrystal Aggregation And Film Formation For Applications In Optoelectronics" (2013). *Wayne State University Dissertations*. Paper 732.

This Open Access Dissertation is brought to you for free and open access by DigitalCommons@WayneState. It has been accepted for inclusion in Wayne State University Dissertations by an authorized administrator of DigitalCommons@WayneState.

**CHALCOGENIDE SOL–GEL ASSEMBLY: CONTROLLING THE KINETICS OF  
NANOCRYSTAL AGGREGATION AND FILM FORMATION FOR APPLICATIONS  
IN OPTOELECTRONICS**

by

**LASANTHA KORALA**

**DISSERTATION**

Submitted to the Graduate School

of Wayne State University,

Detroit, Michigan

in partial fulfillment of the requirements

for the degree of

**DOCTOR OF PHILOSOPHY**

2013

MAJOR: CHEMISTRY (Inorganic)

Approved by

\_\_\_\_\_  
Advisor

\_\_\_\_\_  
Date

\_\_\_\_\_  
\_\_\_\_\_  
\_\_\_\_\_

## **DEDICATION**

To my parents, my brother and my wife for their unconditional love

## ACKNOWLEDGEMENTS

Life in Detroit has been an amazing experience for me. It wasn't easy with all of the overwhelming challenges I faced during the past five years. Nevertheless, I survived that experience by maintaining a positive attitude and with the help of many people. Here, I would like to thank all those people who were behind me all this time. First, I would like to thank Prof. Stephanie L. Brock, my advisor. I don't know how to thank her for her kindness and support throughout all of these years. She was really patient and supportive, even financially, during the time when I was struggling immensely with my health. Simply put, I owe her for my life. Her great mentorship is the reason behind the success of in my research career. I am really grateful to her for her guidance in becoming a successful professional.

I would like to thank my dissertation committee members, Prof. Claudio N. Verani, Prof. Colin Poole and Prof. Guangzhao Mao, for their valuable advice and time during my PhD career. Also, I offer my sincere gratitude to Prof. Claudio N. Verani and Prof. Guangzhao Mao for writing recommendation letters on my behalf and use of their research facilities.

It is hard to have a successful PhD career without interaction of professionals from various disciplines. I really enjoyed collaborating with many talented researchers in my graduate life. I would like to express my appreciation to all of them, not only for their contribution to this dissertation research, but also for the knowledge and skills that I have acquired from them. I would like to begin with Dr. Ambesh Dixit. After undergoing two back surgeries and intense rehabilitation, I was really in need of some help to continue my research. Then, I met Dr. Ambesh. I have never met a person who is so passionate about research. We worked late night to understand some of the concepts in colloidal aggregation. He taught me how to do use Origin for data fitting, and helped me with van der Paw measurements. Li Li helped me with AFM

measurements. She was always ready to perform AFM measurements whenever I needed. Collaboration with Prof. Ana Flavia Nogueira and Dr. Jilian Freitas at University of Campinas, Brazil took my research career to the next level. I learned a lot about thin film fabrication and photoelectrochemistry from Dr. Freitas, and she helped me greatly throughout my visit in Brazil. I did my final collaborative work with Prof. Stephen Maldonado and Dr. Zhijie Wang at University of Michigan. Both of them were extremely helpful to me during my time in their lab, and they also helped me to interpret some of the photoelectrochemical results.

I am grateful to researchers from Weinberg Physics, LLC: Dr. Irving Weinberg, Dr. Pavel Stepanov and Dr. Mario Urdaneta, for providing me with financial support and allowing me to contribute to their project involving fabrication of radiation devices. I am also very grateful to Dr. Yi Liu and Mei Zhi (Mike) for their assistance with TEM and FESEM measurements, and to Dr. Mary Jane Heeg for her help with PXRD measurements. I also collaborated with Dr. Liu for STEM imaging after he moved to Oregon. I would like to thank Prof. Charles Winter for allowing me to use his instruments which were critical for my research. I had a nice time with both Winter and Verani Group members who also taught me how to use some of their instruments. I greatly appreciate all of them for providing me a nice collaborative working environment throughout my PhD career.

I want to thank all the staff members in the Department of Chemistry, especially Melissa Barton, Debbie McCreless, Diane Kudla, Bernie Miesik, Diane Klimas, and Mary Wood. I would like to express my heartfelt gratitude for all of them for their kindness and support during the time I was struggling with my health. I also thank the staff members of the Science Stores for always being kind to me and willing to help me any time I needed assistance from them. I am

grateful to Nestor Ocampo, our computer guru, who was always willing to help me with my computer matters and also for his encouraging words whenever I met him.

I would like to thank former Brock group members: Dr. Hongtao Yu, Dr. Elayaraja Muthuswamy, Dr. Qinghong Yao, Dr. Shreyashi Ganguly, Dr. Layan Savithra and Dr. Yanhua Zhang. I thank Dr. Yu for teaching me the Schlenk line techniques and all the others for teaching me various characterization techniques. Dr. Muthuswamy is a good friend of mine and I was always inspired by his work ethic. Both Dr. Muthuswamy and Dr. Savithra helped me a lot outside the lab, and I want to thank them for their great support during the most difficult time of my life. I also would like to thank current group members: Asha, Derak, Roshini, Jessica, Ruchira, Da, and Indika. Derak and I had some great discussions of various subjects ranging from science to politics. He also proofread some of my documents.

I also thank all my friends and the Michigan Sri Lankan community for being supportive throughout my time here.

I especially thank my uncle, Saman, and aunt, Sanjeevani, who helped me greatly during the toughest time of my life.

Finally, I would like to use this space to thank my family who has dedicated their lives to me. I am so lucky to have parents who always think about their children before themselves. I have a brother who is very kind and honest, and always wishes the best for me. As for my wife, I can't imagine a life without her. There are no words to convey how much I love her.

Lasantha Korala  
Wayne State University  
May 2013

## TABLE OF CONTENTS

Dedication.....	ii
Acknowledgements.....	iii
List of Tables.....	vii
List of Figures.....	viii
List of Schemes.....	xiii
Chapter 1 – Introduction .....	1
Chapter 2 – Experimental Methods .....	29
Chapter 3 – Aggregation Kinetics of Metal Chalcogenide Nanocrystals: Generation of transparent CdSe/ZnS Core/shell Gels.....	64
Chapter 4 – Fabrication of Chalcogenide Sol–gel Films for Applications in Optoelectronics .....	83
Chapter 5 – Connecting the (Quantum) Dots: Towards Hybrid Photovoltaic Devices based on Chalcogenide Gels.....	112
Chapter 6 – Conclusions and Prospectus .....	122
References.....	131
Abstract.....	143
Autobiographical Statement.....	145

## LIST OF TABLES

<b>Table 3.1.</b>	Core size and optical properties of CdSe/ZnS core/shell NCs .....	69
<b>Table 3.2.</b>	Gel point, $t_{gel}$ , and average cluster size near the gel point for green- and orange-emitting gels formed from different amounts of TNM .....	77
<b>Table 3.3.</b>	Fractal dimension, $D$ , correlation length, $\xi$ , and relative cluster mass, $m$ , values of the green-emitting gels formed from different amounts of TNM .....	79

## LIST OF FIGURES

<b>Figure 1.1.</b>	Schematic illustration of the density of states (DOS) in different sized systems of (a) metal, and (b) semiconductor .....	3
<b>Figure 1.2.</b>	Schematic illustration of (a) a typical experimental setup for the hot-injection method, and (b) La Mer model for nucleation and growth events occurring during the synthesis of colloidal NCs by the hot-injection technique .....	5
<b>Figure 1.3.</b>	Two models describing NC growth at an early stage: (a) traditional “focusing of size distribution” model, and (b) “self-focusing” model .....	6
<b>Figure 1.4.</b>	Simple two band model band diagram for a direct gap (a) bulk semiconductor, and (b) semiconductor QD .....	9
<b>Figure 1.5.</b>	Schematic illustration of (a) the potential well formed in the conduction and valence band of the QD in any one dimension (x, y or z), and (b) the absorption spectrum of a bulk semiconductor and QD .....	11
<b>Figure 1.6.</b>	Illustration of (a) density of states for semiconductor structures with different confined dimensions, and (b) band gap as a function of the length of the confined dimension .....	12
<b>Figure 1.7.</b>	(a) Band structure of a diamond-like bulk semiconductor (b) Band structure of a QD .....	14
<b>Figure 1.8.</b>	(a) Electron and hole quantized states of CdSe QDs. (b) Absorption spectrum of a CdSe QDs (mean radius 4.1 nm) .....	15
<b>Figure 1.9.</b>	Schematic representation of (a) band-edge (I) and surface state (II) emission in QDs, and (b) energy level alignment in different core/shell QD systems .....	16
<b>Figure 1.10.</b>	Schematic representation of metal chalcogenide aerogel/xerogel synthesis .....	19
<b>Figure 1.11.</b>	Proposed gelation mechanism for metal chalcogenide NCs .....	20
<b>Figure 1.12.</b>	Electronic interactions in a NC film where (a) weak electronic coupling results in unperturbed energy levels whereas (b) strong electron coupling results in miniband formation .....	22
<b>Figure 2.1.</b>	A phase diagram showing the liquid-vapor phase boundary and the critical point above which densities of the liquid and vapor are similar .....	31
<b>Figure 2.2.</b>	Two types of elastic light scattering: Rayleigh scattering and Mie scattering .....	33

<b>Figure 2.3.</b>	Schematic diagram of a DLS instrument .....	34
<b>Figure 2.4.</b>	Geometrical illustration of X-ray diffraction on a set of parallel crystal planes .....	36
<b>Figure 2.5.</b>	Types of diffraction geometries (a) reflection mode and (b) transmission mode .....	38
<b>Figure 2.6.</b>	Outlines of (a) sequential mode data collection using a point detector, (b) parallel mode data collection using a position sensitive detector, and (c) data collection using an array of solid state detectors in SAXS experiments .....	41
<b>Figure 2.7.</b>	Two possibilities of relaxation of an inner-shell excited atom: (a) Emission of a characteristic X-ray; (b) emission of an Auger electron, and (c) effects resulting from the interaction of primary electron beam and specimen .....	44
<b>Figure 2.8.</b>	Schematic of a conventional TEM .....	46
<b>Figure 2.9.</b>	Schematic showing the main components of a SEM .....	48
<b>Figure 2.10.</b>	Common X-ray transitions that lead to lines appearing in an EDS spectrum .....	49
<b>Figure 2.11.</b>	Schematic of a dedicated STEM .....	51
<b>Figure 2.12.</b>	Schematic of an AFM .....	53
<b>Figure 2.13.</b>	Block diagram of a UV–vis spectrometer .....	54
<b>Figure 2.14.</b>	Jablonski diagram illustrating the processes occurring in the absorption and emission of light .....	56
<b>Figure 2.15.</b>	Block diagram of a PL spectrometer .....	57
<b>Figure 2.16.</b>	Sheet resistance measurements by van der Pauw method .....	60
<b>Figure 2.17.</b>	Experimental set up for controlled-potential experiments .....	61
<b>Figure 2.18.</b>	Schematic of the optical bench that was used for the photoelectrochemical measurements described in Chapter 5 .....	62
<b>Figure 2.19.</b>	Schematic diagram of an IPCE experimental setup with an electrochemical cell .....	63

<b>Figure 3.1.</b>	(a) HRTEM images of (a) green- and (b) orange-emitting CdSe core NCs .....	68
<b>Figure 3.2.</b>	(a) Time evolution, as a function of the amount of TNM, of $\bar{R}_h$ for green- and orange-emitting CdSe/ZnS NCs; and (b) $\log \bar{R}_h$ vs time for green-emitting CdSe/ZnS NCs .....	71
<b>Figure 3.3.</b>	(a) Photographs, and (b) transmittance of green-emitting wet gels formed from different TNM concentrations; (c) Photographs of orange-emitting wet gels formed from different TNM concentrations; (d) Photographs of green-emitting wet gels (10-fold increase in concentration) formed by different TNM concentrations .....	72
<b>Figure 3.4.</b>	Time evolution of $\bar{R}_h$ for green-emitting concentrated CdSe/ZnS sols oxidized by (a) 15 $\mu\text{L}$ and (b) 20 $\mu\text{L}$ of 3% TNM .....	73
<b>Figure 3.5.</b>	$\log \bar{R}_h$ vs time and $\log \bar{R}_h$ vs $\log$ time for orange-emitting CdSe/ZnS sols oxidized by (a) 4 $\mu\text{L}$ , (b) 6 $\mu\text{L}$ , (c) 8 $\mu\text{L}$ , and (d) 10 $\mu\text{L}$ of 3% TNM .....	74
<b>Figure 3.6.</b>	Intensity correlation functions, $g^2(\tau) - 1$ of the (a) green-, and (b) orange-emitting CdSe/ZnS NC sols oxidized by 4 $\mu\text{L}$ of TNM as a function of time .....	77
<b>Figure 3.7.</b>	SAXS spectra of green-emitting wet gels formed from different amounts of TNM. Lines composed of open circles represent the fitting of Equation 12 to the experimental curves .....	79
<b>Figure 3.8.</b>	TEM images of gel clusters formed by (a), (b) 8 $\mu\text{L}$ , and (c), (d) 50 $\mu\text{L}$ of TNM .....	81
<b>Figure 3.9.</b>	SAXS spectrum of an orange-emitting wet gel formed from 4 $\mu\text{L}$ of TNM.....	82
<b>Figure 4.1.</b>	Schematic illustration of the fabrication of a CdSe/ZnS xerogel film .....	91
<b>Figure 4.2.</b>	UV–vis spectrum and PL spectrum of CdSe/ZnS NC sol and xerogel films deposited from 4 and 5 mL of sol .....	92
<b>Figure 4.3.</b>	XRD pattern of a xerogel film deposited on a glass slide from 5 mL of sol .....	93
<b>Figure 4.4.</b>	(a), (b) FESEM images, and (c), (d) AFM images of the CdSe/ZnS xerogel films deposited from 4 mL (left) and 5 mL (right) of sol .....	94
<b>Figure 4.5.</b>	UV–vis and PL spectra of TOPO/stearic acid-capped CdSe and thioglycolic acid-capped CdSe NCs dispersed in toluene and methanol, respectively .....	96

<b>Figure 4.6.</b>	TEM images at two magnifications of (a) TOPO/Stearic acid-capped CdSe NCs, and (b) thioglycolic acid-capped CdSe NCs. (c) Corresponding TEM images of sample (b) after gelation showing formation of NC network .....	98
<b>Figure 4.7.</b>	(a) Thermogravimetric scans (under N <sub>2</sub> flow, 10 °C/min) of CdSe NCs before and after ligand exchange. (b) UV–vis spectra of a thioglycolic acid-capped CdSe film before (sol film) and after gelation (sol–gel film), and after annealing. (c) XRD patterns of a TOPO/stearic acid-capped CdSe film, thioglycolic acid-capped CdSe film (sol film), a sol–gel film, and an annealed sol–gel film .....	99
<b>Figure 4.8.</b>	Bottom graph: C–H stretching region of the reflectance FTIR spectra of a TOPO/stearic acid-capped CdSe film, and thioglycolic acid-capped CdSe film before (sol film) and after gelation (sol–gel film). Top graph: IR spectra of a thioglycolic acid-capped CdSe film before (sol film) and after gelation (sol–gel film), scaled up by a factor of 8.5 .....	100
<b>Figure 4.9.</b>	(a) Photographs of sol–gel films before and after annealing. FESEM images of a (b) thioglycolic acid-capped CdSe NC film (sol film) (c) sol–gel film, and (d) annealed sol–gel film. AFM images of a (e) thioglycolic acid-capped CdSe NC film (sol film) (f) sol–gel film, and (g) annealed sol–gel film .....	102
<b>Figure 4.10.</b>	(a) Photocurrent response of a TOPO/stearic acid-capped CdSe NC film, and CdSe and CdSe/ZnS sol–gel films (annealed at 250 °C), to chopped white light irradiation (100 mW/cm <sup>2</sup> ) at -0.57 V (solution redox potential) with respect to a Ag/AgCl reference electrode. (b) <i>I</i> – <i>V</i> characteristics of the CdSe and CdSe/ZnS sol–gel films (annealed at 250 °C) .....	104
<b>Figure 4.11.</b>	(a) A HAADF-STEM image of TOPO/stearic acid-capped CdSe NCs, and (b), (c), (d) EDS elemental mapping for Cd and Se. (e) A HAADF-STEM image of thioglycolic acid-capped CdSe NCs after gelation, and (f), (g), (h) EDS elemental mapping for Cd and Se .....	105
<b>Figure 4.12.</b>	(a) UV–vis and PL spectra of TOPO/stearic acid-capped CdSe and CdSe/ZnS NCs dispersed in toluene. (b) UV–vis and (c) PL spectra of a thioglycolic acid-capped CdSe/ZnS film before gelation (sol film), after gelation (sol–gel film), and after gelation and annealing (sol–gel film annealed at 250 °C) .....	107
<b>Figure 4.13.</b>	External quantum yield of CdSe and CdSe/ZnS sol–gel films (annealed at 250 °C) at -0.57 V (solution redox potential) with respect to a Ag/AgCl reference electrode. (b) Rest potential response of CdSe and CdSe/ZnS sol–gel films (annealed at 250 °C) to on-off cycles of white light irradiation .....	109

<b>Figure 4.14.</b>	(a) EDS elemental mapping of TOPO/stearic acid-capped CdSe/ZnS NCs for Cd, Se, Zn and S shows that the CdSe cores are only partially covered by the ZnS shell. (b) A HAADF-STEM image of thioglycolic acid-capped CdSe/ZnS NCs after gelation, and (c) EDS elemental mapping for Cd, Se, Zn and S in CdSe/ZnS .....	110
<b>Figure 5.1.</b>	Schematic representation of the synthesis of aerogels from MUA-capped NCs, and TEM images (right) and a FTIR spectrum (left) of a CdSe/ZnS aerogel .....	115
<b>Figure 5.2.</b>	(a) P3HT:NC and (b) P3HT:aerogel mixtures containing 50 wt% inorganic material .....	117
<b>Figure 5.3.</b>	AFM images obtained in tapping mode for P3HT films containing (a) 90 wt% and (b) 50 wt% of CdSe/ZnS NCs, and (c) 90 wt% and (d) 50 wt% of CdSe/ZnS aerogel, deposited onto glass slides .....	118
<b>Figure 5.4.</b>	UV–vis absorption spectra of toluene dispersions of CdSe/ZnS NCs and aerogel, and a P3HT film .....	119
<b>Figure 5.5.</b>	Steady-state absorption spectra of hybrid films of (a) P3HT:NCs (b) P3HT:aerogel with different weight ratios of CdSe/ZnS .....	120
<b>Figure 5.6.</b>	Photocurrent response of NC, aerogel and P3HT films under white light illumination ( $100 \text{ mW cm}^{-2}$ ) .....	121
<b>Figure 5.7.</b>	Photocurrent response of (a) P3HT:NC and (b) P3HT:aerogel films under white light ( $100 \text{ mW cm}^{-2}$ ) .....	122
<b>Figure 5.8.</b>	Scheme of charge transfer processes expected for systems containing electrodes based on (a) P3HT, (b) CdSe/ZnS NCs or aerogel, and (c) P3HT:CdSe/ZnS NCs or aerogel hybrid films, in the presence of a 0.1 M $\text{Na}_2\text{SO}_4$ electrolyte saturated with $\text{O}_2$ and under white light irradiation .....	123
<b>Figure 6.1.</b>	Schematic illustration of a NC sensitized solar cell .....	130
<b>Figure 6.2.</b>	Schematic illustration of a depleted heterojunction NC solar cell .....	131

## LIST OF SCHEMES

- Scheme 4.1.** Schematic illustration of the fabrication of a CdSe/ZnS xerogel film .....91
- Scheme 4.2.** Mechanism of oxidative ([OX]) gelation of a thioglycolic acid-capped NC film (sol film) submerged in a TNM solution .....97

## CHAPTER 1

### INTRODUCTION

The dissertation research is focused on achieving two main goals: (1) optimization of the conditions of sol–gel assembly of semiconductor metal chalcogenide nanocrystals (NCs) in order to tune the properties of resultant gel structures with the aim of addressing application-specific needs, and (2) incorporation of gel materials into device architectures and evaluation of the properties related to relevant applications. In order to accomplish these goals, the physical mechanism of gelation was ascertained to control the optical quality of the gels, methods were established to prepare sol–gel films and their optoelectronic properties were determined, and chalcogenide gel materials were utilized to fabricate photovoltaic devices. This chapter provides background information relevant to achieving the overall goals of the dissertation research. First, semiconductor NCs and their solution-phase synthesis procedures are briefly introduced. Secondly the electronic structure and optical properties of semiconductor NCs are discussed, common assembly methods are described and sol–gel assembly is introduced. Finally, charge transport in semiconductor NC films is briefly discussed.

#### 1.1 Colloidal Semiconductor Nanocrystals (NCs)

In the last two decades, the application of size control in the synthesis of extended solids in order to tune the properties has brought about a new class of materials enabling increased efficiency in devices and the development of new applications. Colloidal semiconductor NCs [Group IV (Si, Ge), I-VI ( $\text{Ag}_2\text{S}$ ,  $\text{Ag}_2\text{Se}$ ,  $\text{Ag}_2\text{Te}$ )<sup>1</sup>, II-V ( $\text{Cd}_3\text{P}_2$ ,<sup>2</sup>  $\text{Cd}_3\text{As}_2$ )<sup>3</sup> II-VI ( $\text{ZnO}$ ,  $\text{ZnS}$ ,  $\text{ZnSe}$ ,  $\text{CdS}$ ,<sup>4</sup>  $\text{CdSe}$ ,<sup>4</sup>  $\text{CdTe}$ ,<sup>4</sup>  $\text{HgTe}$ )<sup>5</sup>, III-V ( $\text{GaAs}$ ,<sup>6</sup>  $\text{GaP}$ ,<sup>6</sup>  $\text{InP}$ ,<sup>7</sup>  $\text{InAs}$ ,<sup>7</sup>  $\text{InSb}$ )<sup>8</sup> and IV-VI ( $\text{PbS}$ ,<sup>9</sup>  $\text{PbSe}$ ,<sup>10</sup>  $\text{PbTe}$ )<sup>11</sup>] composed of hundreds to a few thousand atoms (sizes typically less than  $\sim 10$  nm)<sup>12</sup> are a technologically important class of inorganic materials that exhibits size tunable optical and

electronic properties that are extremely useful in developing next generation light-emitting diodes (LEDs),<sup>13</sup> photodetectors,<sup>14</sup> and photovoltaic devices.<sup>15</sup> The optical and electronic properties of a material are primarily determined by the density of electronic energy levels [density of states (DOS)] of the material near the Fermi level. In semiconductor NCs, the DOS varies as a function of NC size, leading to size dependant optical and electronic properties, and this phenomenon is known as the quantum size effect. Thus, for instance, optical emission of CdSe can be tuned throughout the visible region by altering the band gap via varying the NC size.

Compared to metal NCs, semiconductor NCs show more pronounced size dependant optical and electronic properties. This can be explained by considering the position of the Fermi level,  $E_f$ , in the band structure of metal and semiconductor NCs. Figure 1.1 schematically illustrates the DOS for atomic-, nano-, and bulk-scale metal and semiconductor materials. In bulk semiconductors or metals, a large number of atomic orbitals overlap to form energy bands with continuous energy levels. As the band develops with the addition of atoms, the center of the band develops first and edge develops last. Therefore, in the nanometer size regime, the energy level spacing is very small in the center of the band compared to the edge of the band.<sup>16</sup> Once the energy level spacing in the band exceeds the given temperature, electrical and optical properties of a material vary with the size. The Fermi level of metals lies in the center of the band where the energy level spacing is very small. Hence, the optical and electronic properties are similar to bulk metal even at very small size (tens or hundreds of atoms) and temperature above a few Kelvin. In contrast, the Fermi level of semiconductors lies between bands so that the optical and electronic properties are strongly dependent on the NC size even for relatively larger size (~10,000 atoms).

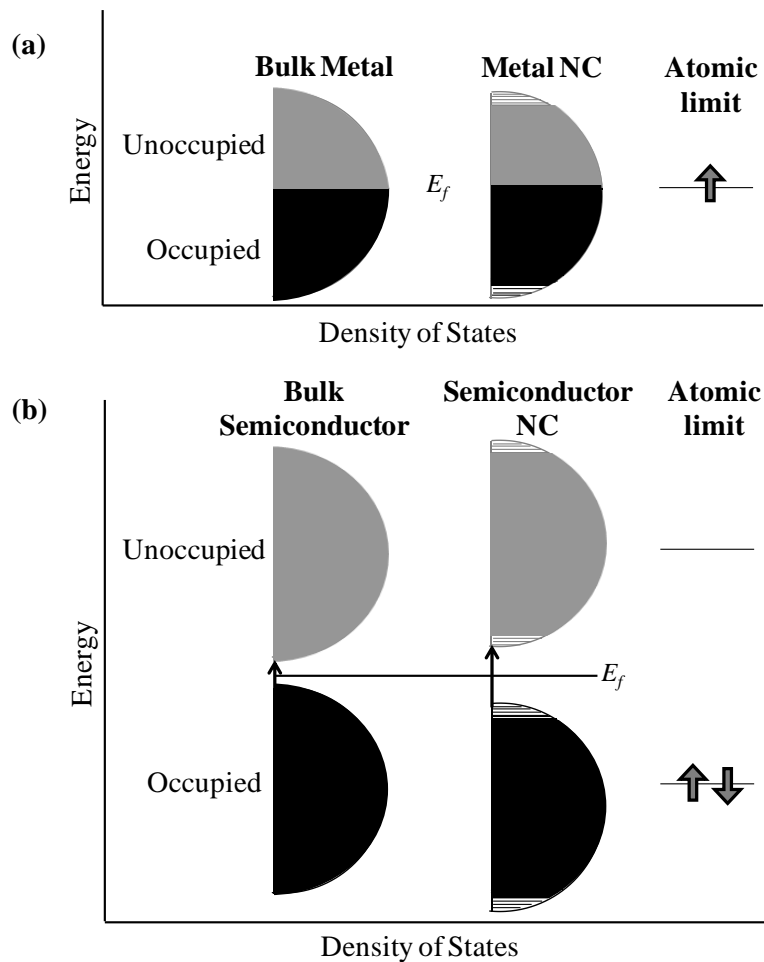


**Figure 1.1** Schematic illustration of the density of states (DOS) in different sized systems of (a) metal, and (b) semiconductor (adapted from Alivisatos).<sup>16</sup>

The size of the semiconductor NCs also has a significant impact on other physical properties. For example, the increase in the fraction of surface atoms with the decrease of NC size leads to depression of the melting temperature (solid-liquid transition) and increase of the pressure required to induce transformation to a denser phase (solid-solid transition).<sup>16</sup>

## 1.2 Colloidal NC Synthesis

Colloidal NCs consist of inorganic nanocrystal cores surrounded by a layer of surface organic ligands. High quality, spherical NCs with narrow size distribution can be synthesized by

hot-injection techniques in which anionic precursors are rapidly injected into a solution containing cationic precursors at high temperature in the presence of organic surfactants, as illustrated in Figure 1.2a. At high temperature, the precursors, which are typically inorganic salts (e.g. cadmium oxide, cadmium acetate, or cadmium carbonate for CdSe)<sup>17</sup> or organometallic compounds (e.g. dimethylcadmium for CdSe)<sup>4</sup> chemically transform into reactive atomic or molecular species (monomers) leading to nucleation and growth of NCs.<sup>18</sup> The Classical La Mer model of colloidal particle nucleation and growth can be utilized to describe the nucleation and growth events occurring in the synthesis of NCs by hot-injection methods.<sup>12</sup> As shown in Figure 1.2b, quick injection of the precursors causes supersaturation of formed monomers followed by a nucleation burst of NCs resulting in lowering of monomer concentration below the nucleation threshold. Alternatively, burst nucleation can also be realized by heating the reaction mixture consisting of precursors, organic surfactants and solvent (“heating up” method). After the nucleation event, NCs grow by adding monomers to the nuclei until the concentration of monomers is considerably decreased, and then growth occurs according to Oswald ripening mechanism in which larger NCs grow due to dissolution of smaller NCs and consequently the average NC size increases while the overall NC concentration decreases. A monolayer of organic surfactant ligands are dynamically adhered to the growing NC surface, preventing aggregation of NCs in the solution while allowing monomers to incorporate into the inorganic core. Common surfactants include long-chain carboxylic and phosphonic acids (e.g. oleic acid and n-octadecylphosphonic acid), alkanethiols (e.g. dodecanethiol), alkyl phosphines, alkylphosphine oxides [e.g. trioctylphosphine (TOP), trioctylphosphine oxide (TOPO)] and alkylamines (e.g. hexadecylamine).<sup>19</sup>

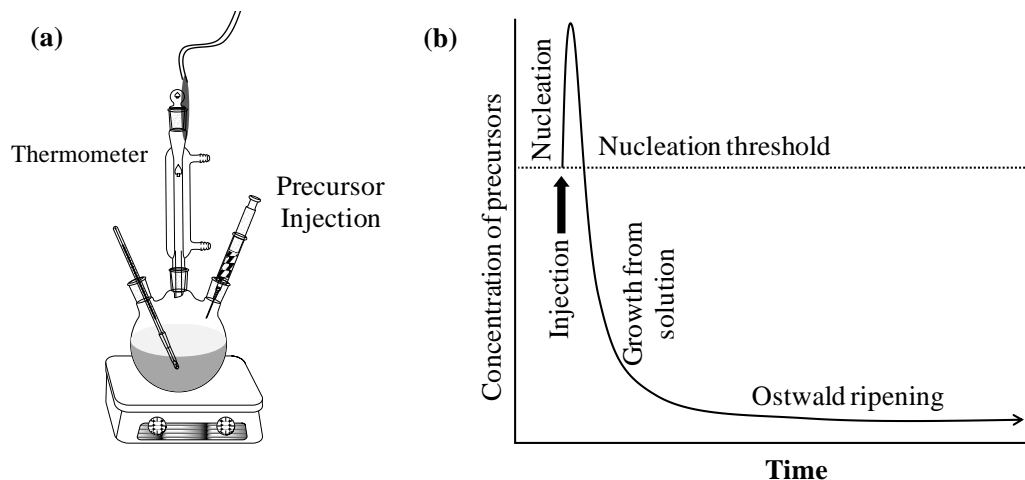


**Figure 1.2** Schematic illustration of (a) a typical experimental setup for the hot-injection method, and (b) La Mer model for nucleation and growth events occurring during the synthesis of colloidal NCs by the hot-injection technique (adapted from Klimov).<sup>12</sup>

The growth regime that occurs prior to Ostwald ripening has a significant impact on the size distribution. The early stage of NC growth can be described using a “focusing of size distribution” model.<sup>20</sup> According to this model, a rapid growth rate of smaller NCs compared to larger NCs results in a relatively narrow size distribution as the size tends to focus (Figure 1.3a). In contrast, during the Ostwald ripening stage, the size tends to defocus as a consequence of the growth of larger NCs due to the sacrificial dissolution of smaller NCs and this results in a broader size distribution. Peng et al. introduced an alternative model known as the “self-focusing” model to explain the early stage of the growth process. According to the self-focusing model, a narrow size distribution in the pre-Ostwald regime is a consequence of rapid dissolution of smaller NCs due to inter-NC diffusion, as illustrated in Figure 1.3b.

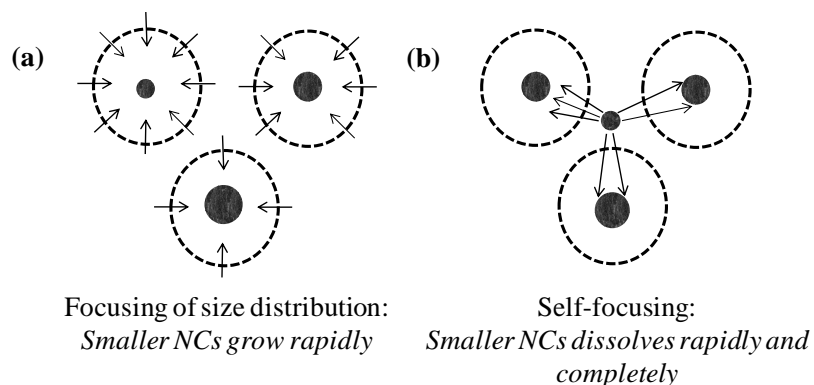


**Figure 1.3** Two models describing NC growth at an early stage: (a) traditional “focusing of size distribution” model, and (b) “self-focusing” model (adapted from Chen).<sup>20</sup>

Tuning of NC size, size distribution and shape are key aspects of colloidal NC synthesis. Longer growth time, higher growth temperature, higher precursor concentration and lower surfactant/precursor ratio yield larger NCs. However, longer growth time typically results in a broad size distribution due to Ostwald ripening. Nevertheless, NCs with narrow size distribution can be obtained by means of size-selective separation methods such as size-selective precipitation. On the other hand, monodisperse spherical NCs can be obtained by arresting the reaction before the Ostwald ripening begins; i.e. during the rapid growth stage. This allows size tuning with narrow size distribution since size can be controlled by varying the nucleation size by adjusting the precursor concentration and nucleation temperature. Alternatively, injection of additional precursors without exceeding the nucleation threshold i.e. supersaturation can be employed to delay the Ostwald ripening, thus NCs can grow for a longer time at the fast growth stage where the size is focused.

As discussed above, nucleation of NCs is followed by fast-growth regime (at high monomer concentration) where size is focused and Ostwald ripening (at low monomer concentration) where size tends to defocus. However entire growth process is thermodynamically

controlled and thus the resultant NCs are spherical due to lower surface energy of spherical NCs compared to that of more anisotropic NCs. Therefore, a transition from a thermodynamic growth regime to a kinetic growth regime, where high-energy facets grow faster than low energy facets, is needed for the NCs with highly anisotropic shapes.<sup>18</sup> The kinetic growth regime can be accessed at very high monomer concentrations. In the kinetic growth regime, shape can be more effectively engineered by adding surfactant molecules that bind to certain crystal facets strongly, and this selective adhesion slows the growth rate of those facets and results in rod- or disc-shaped NCs (e.g. rod-shaped CdSe NCs<sup>21</sup>). At these growth conditions, NCs with more complex shapes, such as arrow-shaped and branched NCs, can be synthesized by using mixtures of surfactants with different concentrations and varying the growth time (e.g. arrow-, teardrop-, and tetrapod-shaped CdSe NCs<sup>22</sup>). Other approaches to engineer the NC shape include oriented attachment of NC building blocks to synthesize nanowires (e.g. straight, zigzag, helical, branched, and tapered PbSe nanowires),<sup>23</sup> Solution-liquid-solid (SLS) growth of nanowires (e.g. GaAs nanowires),<sup>24,25</sup> and use of the nanoscale Kirkendall effect (e.g. hollow CoSe NCs)<sup>26</sup> or galvanic displacement reactions to synthesize hollow nanostructures (e.g. hollow Au nanocubes).<sup>27</sup>

Although the kinetic growth regime can also be accessed in hot-injection synthesis, enabling control of shape, the resultant NCs have almost exclusively thermodynamically stable crystal phase. The cation exchange reaction is a unique strategy to synthesize NCs with metastable phases.<sup>28</sup> In this technique, NCs with ionic lattices are used as templates for kinetically controlled cation exchange reactions. For example, less stable zinc blende CdSe nanorods can be synthesized by cation exchange of rocksalt PbSe nanorods that act as not only a shape but also a crystallographic template.<sup>29</sup> Moreover, NCs that can be synthesized with

excellent size and shape control by hot-injection techniques can be used as templates for synthesis of other NCs (e.g. Ag<sub>2</sub>Se synthesis using CdSe NC templates).<sup>30</sup> Alivisatos et al. have extended the cation exchange method to synthesize semiconductors with covalent lattices.<sup>6</sup> For example gallium pnictide NCs such as Ga<sub>3</sub>P<sub>2</sub> and Ga<sub>3</sub>As<sub>2</sub> that have covalent lattices can be synthesized by cation exchange reactions using Cd<sub>3</sub>P<sub>2</sub> and Cd<sub>3</sub>As<sub>2</sub> as templates, respectively.

Apart from single component nanostructures, colloidal synthesis can be used to prepare multicomponent nanoheterostructures in elaborate concentric/eccentric onion-like or oligomer-type architectures by a seeded-growth method in hot-injection synthesis.<sup>31</sup> Examples of heterostructures include core/shell structures such as concentric spherical structures (e.g. CdSe/ZnS,<sup>32</sup> CdSe/ZnSe/ZnS<sup>33</sup>), eccentric rod-shaped structures [e.g. CdSe/CdS (spherical CdSe core and rod-like CdS shell)],<sup>34</sup> and dumbbell structures such as CoPt<sub>3</sub>-Au (spherical CoPt<sub>3</sub> and spherical Au),<sup>34</sup> PbSe-CdSe-PbSe (CdSe nanorods with PbSe tips),<sup>35</sup> and highly anisotropic structures such as tetrapod-shaped structures [e.g. ZnTe/CdTe (spherical ZnTe core and CdTe arms),<sup>36</sup> CdSe/Au (tetrapod-shaped CdSe core and Au tips)],<sup>37</sup> and even branched tetrapod-shaped structures [e.g. CdSe/CdTe (tetrapod-shaped CdSe core with branched CdTe tips)].<sup>38</sup> Additionally, cation exchange can be utilized to synthesize heteronanostructures that are difficult to synthesize by hot-injection synthesis (e.g. PbSe/PbS (spherical PbSe core and rod-like PbS shell) by cation exchange with CdSe/CdS)<sup>39</sup> or more complex structures such as CdS/Au<sub>2</sub>S segmented nanoheterostructures.<sup>40</sup>

### 1.3 Electronic Structure and Optical Properties of Semiconductor NCs

Optical spectroscopy is one of the most important tools to explore the electronic structure of semiconductor NCs. Figure 1.4a shows the band diagram for a direct-gap bulk semiconductor that is plotted in terms of wave vector,  $k$  ( $k = 2\pi/\lambda$ ), of electron and  $k$  is proportional to

electron's momentum. Band gap,  $E_g$ , (e.g. the bulk band gap of CdSe is 1.76 eV) corresponds to the energy difference between the top of the valence band and the bottom of the conduction band, and is dependent on the composition. In direct gap semiconductors electronic transitions are allowed by electrical dipole (i.e. electronic transitions follow the  $\Delta k = 0$  selection rule); absorption of a photon of energy greater than  $E_g$  excites an electron from valence band to the conduction band leaving a negatively charged electron and a positively charged hole in conduction band and valence band respectively.

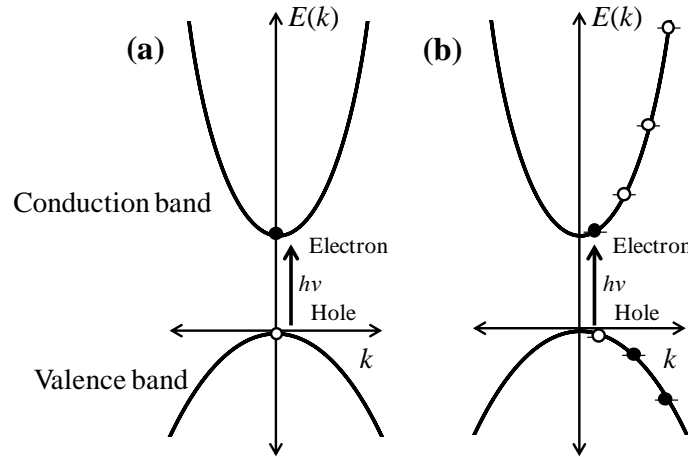


**Figure 1.4** Simple two band model band diagram for a direct gap (a) bulk semiconductor, and (b) semiconductor QD (adapted from Klimov).<sup>12</sup>

An electrostatically bound electron-hole pair is known as an exciton. The concept of effective mass,  $m^*$ , is introduced for mass of an electron ( $m_e^*$ ) [or hole ( $m_h^*$ )] in a solid due to the difference in masses with a free electron  $m_e$ .  $m^*$  can be defined as<sup>41</sup>

$$m^* = \frac{1}{\hbar^2} \frac{d^2 E}{dk^2} \quad (1.1)$$

where  $E$  is energy as a function of wave vector,  $k$ , in momentum space ( $p = \hbar k$ ),  $\hbar = h/2\pi$  and  $h$  is Planck's constant. For an exciton, the effective reduced mass,  $\mu$ , can be expressed as

$$\mu = \frac{m_e^* m_h^*}{m_e^* + m_h^*} \quad (1.2)$$

The natural length scale of the electron-hole pair,  $a_{exc}$  which is known as the exciton Bohr radius can be defined as<sup>41</sup>

$$a_{exc} = \frac{\epsilon_0 \epsilon h^2}{\pi \mu e^2} \quad (1.3)$$

where  $\epsilon$  is the dielectric constant of the material and  $\epsilon_0$  is the dielectric constant or permittivity of the free space. Apart from excitons, a Bohr radius can be defined for the electrons ( $a_e$ ) and holes ( $a_h$ ) separately. When the size of the semiconductor NC is comparable or smaller than the exciton Bohr radius, charge carriers are confined by the boundaries of the material, giving rise to quantum size effect as described in section 1.1. Spherical semiconductor NCs that show this phenomenon are known as quantum dots (QDs). The quantum size effect results in a quantization of the bulk band as illustrated in Figure 1.4b. This can be understood by modeling the QD as a semiconductor inclusion embedded in an insulating matrix which gives rise to a ladder of discrete electron and hole states, as shown in Figure 1.5a.<sup>12</sup> In contrast to bulk semiconductors, which show a continuous absorption spectrum above the band gap, ideally, QDs exhibit discrete absorption events (Figure 1.5b) and because of these discrete electronic transitions, QDs are also referred to as “artificial atoms”.

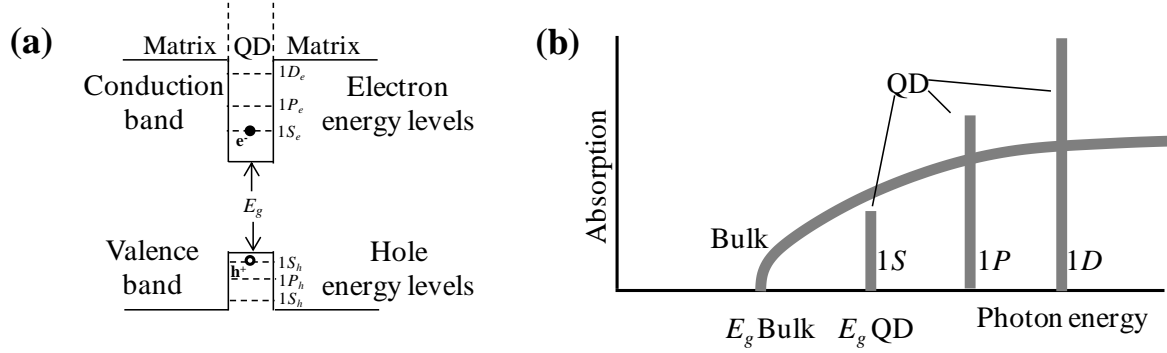


**Figure 1.5** Schematic illustration of (a) the potential well formed in the conduction and valence band of the QD in any one dimension (x,y, or z), and (b) the absorption spectrum of a bulk semiconductor and QD (adapted from Klimov).<sup>12</sup>

The Energy of the electron and hole states of QDs depends on the extent of quantum confinement, which is directly related to the size of the QD. Three regimes of quantum confinement can be defined based on the QD size: The strong confinement regime ( $r < a_e, a_h, a_{exc}$ ), the intermediate confinement regime ( $a_h < r < a_e, a_{exc}$ ) and the weak confinement regime ( $a_e, a_h < r < a_{exc}$ ), where  $r$  is the QD radius.<sup>12</sup> For example,  $a_{exc}$  of a prototype CdSe QD is 6 nm, and therefore, depending on the size of the CdSe QD, electrons and holes are either strongly or weakly confined by the QD boundary. A quantitative description of the quantum size effect can be obtained using the particle-in-a-sphere model with a series of approximations. The band gap of the QD can be estimated using the effective mass approximation, in which conduction and valence bands are approximated as single parabolic conduction and valence bands (Figure 1.3b), and the effective band gap can be approximated as<sup>12</sup>

$$E_g(\text{QD}) = E_g + \frac{\hbar^2 \pi^2}{2\mu r^2} \quad (1.4)$$

In the strong confinement regime, an additional term is used to account for the Coulombic attraction between electrons and holes.<sup>12</sup>

$$E_g(\text{QD}) = E_g + \frac{\hbar^2 \pi^2}{2\mu r^2} - \frac{1.8e^2}{\epsilon r} \quad (1.5)$$

The electron and hole states can then be described using two quantum numbers,  $nL_e$  or  $nL_h$ , where  $L$  is the angular momentum associated with the particle-in-a-sphere envelope function, and  $n$  is the number of the state in a series of states of a given symmetry. As shown in Figure 1.5a, electron and hole states can be denoted as  $1S_e, 1P_e, 1D_e, 1S_h, 1P_h, 1D_h$  ( $S$  for  $L = 0$ ,  $P$  for  $L = 1$ ,  $D$  for  $L = 2$ ) etc.

The shape of the semiconductor NC also has a significant effect on the electronic structure. The degree of confinement decreases as the number of confined dimensions decreases (three (QD) > two [quantum rods and wires] > one (quantum disks and wells]). Figure 1.6 illustrates the idealized density of electronic states in one band of 2-dimensional, 1-dimensional and 0-dimensional semiconductor structures along with their band gap as a function of  $d$  (thickness or diameter).

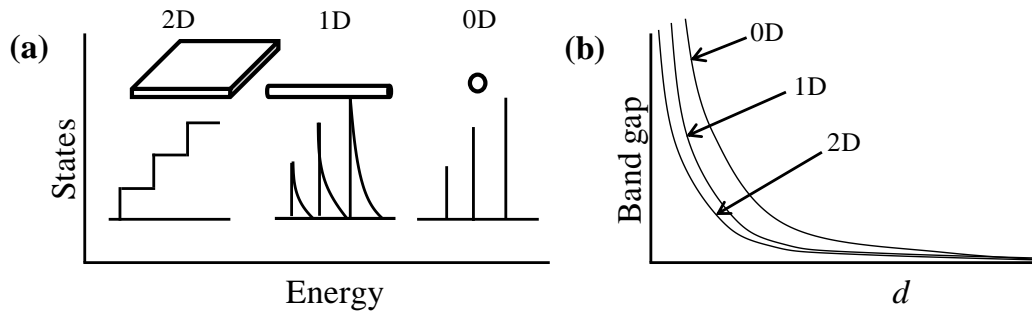


**Figure 1.6** Illustration of (a) density of states for semiconductor structures with different confined dimensions, and (b) band gap as a function of the length of the confined dimension (adapted from Alivisatos and Smith).<sup>16,42</sup>

As discussed in section 1.2, high-quality QDs with narrow size and shape distribution can be produced by optimization of solution phase synthetic conditions, and these high-quality QD samples reveal many excitonic features in their absorption spectra. Therefore, instead of a simple two band model, a more complicated real band structure should be considered to explain these transitions. Typically, the valence band of diamond-like (Zinc blend) semiconductors shows multi-subband character, which is caused by the strong spin-orbit coupling.<sup>43</sup> For example, the valence band of bulk CdSe, which is formed by Se 4*p* atomic orbitals, is split into two subbands  $p_{3/2}$  and  $p_{1/2}$  (split-off band), where subscript denotes is the total unit cell angular momentum,  $J = (l + s)$ , which consists of orbital ( $l$ ) and spin ( $s$ ) contributions. For the zinc blende (or cubic) crystal lattice,  $p_{3/2}$  band is split into two more subbands  $J_m = \pm 3/2$  (heavy-hole band) and  $J_m = \pm 1/2$  (light-hole band) away from  $k = 0$ , where  $J_m$  is the projection of  $J$ . Figure 1.7a shows the band structure for a diamond-like semiconductor. The valence band consists of three subbands, the heavy-hole band, the light-hole band, and the split-off band, which are also referred to as A, B and C respectively. However, A and B bands are split at  $k = 0$  for wurtzite (or hexagonal) CdSe, due to the crystal field of the hexagonal lattice. Assuming a cubic crystal lattice, the electronic structure of CdSe QD can be described by a single parabolic conduction band and three simple parabolic bands for each valence subband, and the conduction band and each valence subband gives rise to ladder of electronic and hole states respectively (Figure 1.7b). However, this model fails to explain the electronic transitions in absorption spectrum of CdSe QDs due to the mixing of hole states in different subbands.<sup>12</sup>

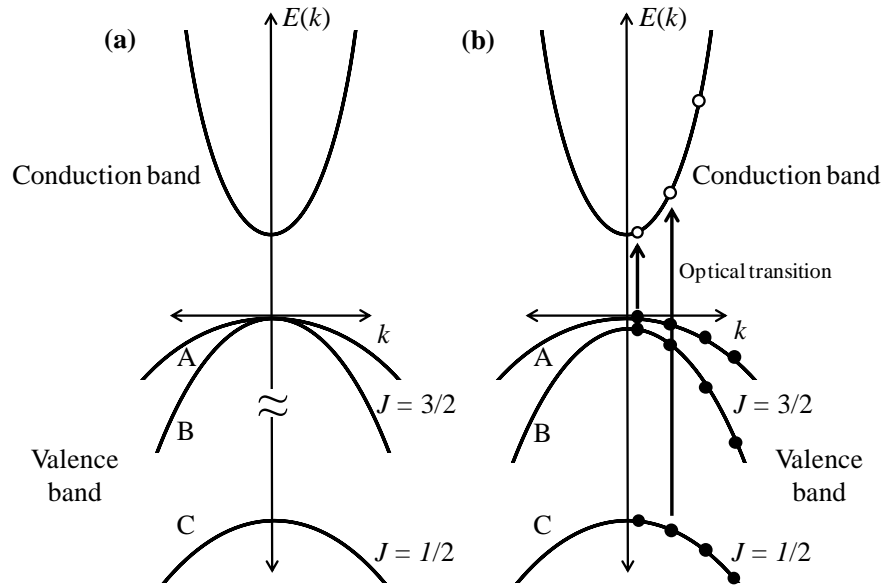


**Figure 1.7** (a) Band structure of a diamond-like bulk semiconductor. The valence band is split into two subbands  $p_{3/2}$  and  $p_{1/2}$  [split-off band (A)] at  $k = 0$ , and the  $p_{3/2}$  band is split into two more subbands [heavy-hole band (B) and light-hole band (C)] away from  $k = 0$ . (b) Band structure of a QD. (adapted from Klimov)<sup>12</sup>

Considering valence subband mixing, Ekimov et al. calculated the size-dependent energies of the hole states, which can be denoted as  $nL_F$ , where  $F$  ( $F = J + L$ ) is the total angular momentum for the hole, which is a sum of total unit cell angular momentum [ $j = s$  (hole spin) +  $l$  (valence band atomic basis)] and the angular momentum associated with the particle-in-a-sphere envelope function ( $L$ ) for the hole.<sup>43</sup> Figure 1.8 shows the electron and hole quantized states of CdSe QDs and an absorption spectrum of CdSe QDs (mean radius 4.1 nm) along with assignments of electron and hole states for well-resolved optical transitions.

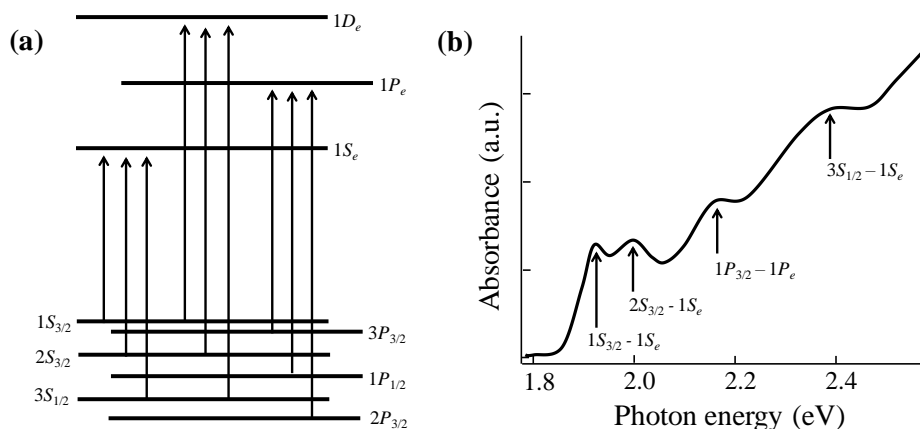


**Figure 1.8** (a) Electron and hole quantized states of CdSe QDs. Arrows illustrate the allowed transitions. (b) Absorption spectrum of a CdSe QDs (mean radius 4.1 nm). Arrows indicates the electron and hole states involved in well-resolved optical transitions (adapted from Klimov).<sup>44</sup>

Optical properties of NCs, especially emission properties, are strongly dependent on the surface structure of NCs, in addition to NC size and shape. Because of the drastic increase of surface to volume ratio with the decrease of size, the number of atoms on the NC surface is a large fraction of the total number of atoms. Surface atoms are coordinatively unsaturated within the crystal lattice resulting in “dangling” bonds at the NC surface. These unpassivated dangling bonds, which are known as surface traps or states, create midgap states. For example, colloidal CdSe QDs usually have cation-rich surfaces and  $\text{Cd}^{2+}$  ions on the surface are mostly passivated by basic ligands (e.g. amines, carboxylic acids, phosphonic acids, phosphines, phosphineoxides, etc.) via dative metal-ligand bonds. However,  $\text{Se}^{2-}$  ions on the QD surface are unpassivated and these selenium  $sp^2$  hybridized dangling bonds trap holes on the surface (trap state or surface emission) resulting in reduction of band edge-emission.<sup>45</sup> Figure 1.9a illustrates the effect of surface states on the fluorescence of CdSe QDs. Relaxation of electrons from surface states,

which reside broadly within the bandgap, to the valence band, results in broad and weak deep-trap emission.

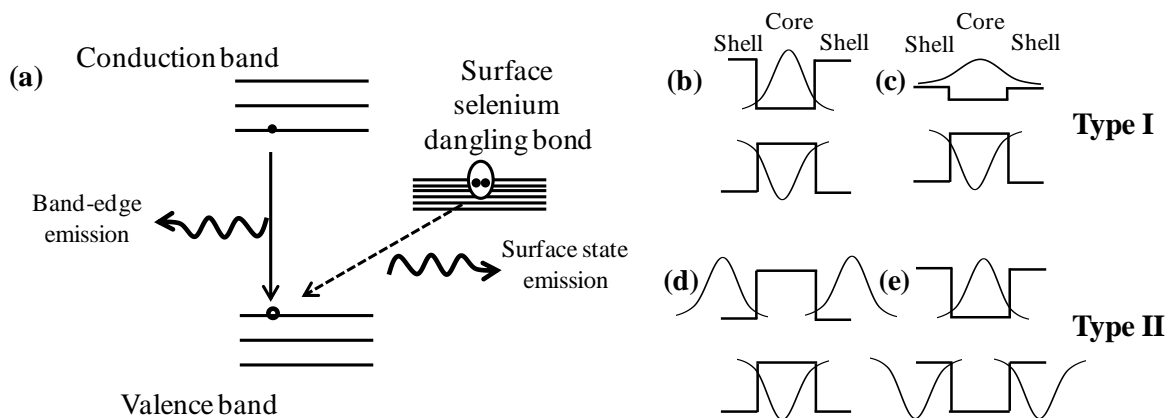


**Figure 1.9** Schematic representation of (a) band-edge (I) and surface state (II) emission in QDs, and (b) energy level alignment in different core/shell QD systems.

The most successful method to eliminate surface states is growing of epitaxial layers of inorganic materials (core/shell structure) in order to passivate the surface dangling bonds, and to confine electron and/or hole wave functions to the cores. The shell can be grown over the core QD via slow addition of shell precursors or successive ion layer adsorption and reaction (SILAR) strategy.<sup>46</sup> Figure 1.9b-e shows the types of band-level alignment in different core/shell QDs. If the QD core is overcoated with wide band gap shell, electrons and holes are confined into the core [type-I heterostructure, e.g. CdSe/ZnS (Figure 1.9b)] resulting in an increased photoluminescence quantum yield. However, as in the case of CdS/CdS) core/shell QDs (Figure 1.9c), electron can be delocalized over the entire core/shell structure when there is a smaller band off set between conduction bands. By contrast, type-II heterostructures have staggered band offsets, and the electron and hole wave functions are spatially separated (Figure 1.9d and e) which in turn promotes exciton dissociation.

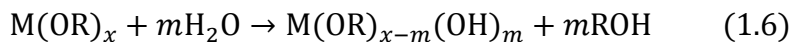
## 1.4 Semiconductor NC Assemblies

Development of excellent solution-phase synthetic strategies to produce high quality NCs with narrow size and shape distribution has opened up tremendous opportunities in a wide variety of applications. Due to their impressive size and shape dependent electrical and optical properties along with solution processability, semiconductor NCs are extremely useful in electronic and optoelectronic device applications. However, exploitation of semiconductor NCs for these applications requires macroscopic assemblies where NCs should effectively communicate with each other in order to achieve superior device performance. For example, semiconductor NC assemblies used in solar cell applications should not just perform light absorption, but should perform charge separation and transport efficiently via inter-NC communication. Therefore, the NC assembly method plays a major role in device performance.

For electronic and optoelectronic applications, semiconductor NCs are typically assembled into thin films. Short-range-ordered close-packed NC films can be fabricated by spin casting or drop casting of a colloidal NC solution, or using other techniques such as Langmuir–Blodgett, layer-by-layer deposition (LBL), doctor blading, and inkjet printing.<sup>19</sup> Additionally, NCs can self assemble from solution into long-range ordered films or three dimensional crystals upon slow evaporation of solvent or controlled destabilization of the solution.<sup>19</sup>

Brock et al. have developed an alternative method to assemble semiconductor NCs, especially metal chalcogenide NCs, into non-ordered three dimensional architectures, i.e. xerogels and aerogels, based on the sol–gel methods.<sup>47</sup> In traditional oxide sol–gel assembly, metal or nonmetal alkoxides (precursors) in acidic or basic aqueous or alcohol media undergo a series of hydrolysis and condensation reactions to form nanoparticles (colloidal sol) followed by

formation of a network of nanoparticles (wet gel) via controlled aggregation. In water or alcohol media, metal alkoxides hydrolyze as<sup>48</sup>



When  $m = x$ , total hydrolysis occurs, which is followed by either water condensation (Equation 1.7) or alcohol condensation (Equation 1.8) reactions.



The wet gel network can be dried under ambient conditions to form a xerogel, which is a more dense material due to the pore collapse as a result of capillary forces exerted during the evaporation of the pore liquid. This can be prevented by supercritical extraction of the solvent, which allows solvent to be removed without significantly impacting the wet gel structures due to the absence of a liquid-vapor interface.<sup>49</sup> Dried gel structures (aerogels) closely resemble the original wet gel structure and are highly porous.

Gacoin et al. originally showed the applicability of sol–gel chemistry to assemble discrete CdS NCs into wet gels.<sup>50</sup> As illustrated in Figure 1.10, controlled oxidation of thiolate-capped metal chalcogenide NC solution (sol) leads to aggregation of NCs due to oxidation-induced loss of thiolate ligands from the NC surface resulting in a three dimensional network of NCs (wet gel). Brock et al. extended this method to assemble other metal chalcogenide NCs such as CdSe,<sup>51</sup> CdTe,<sup>52</sup> ZnS,<sup>47</sup> PbS,<sup>47</sup> PbSe,<sup>53</sup> PbTe,<sup>54</sup> and Bi<sub>2</sub>Te<sub>3</sub><sup>55</sup> and resulting gels were dried under both ambient conditions and supercritical conditions to form xerogels and aerogels, respectively.

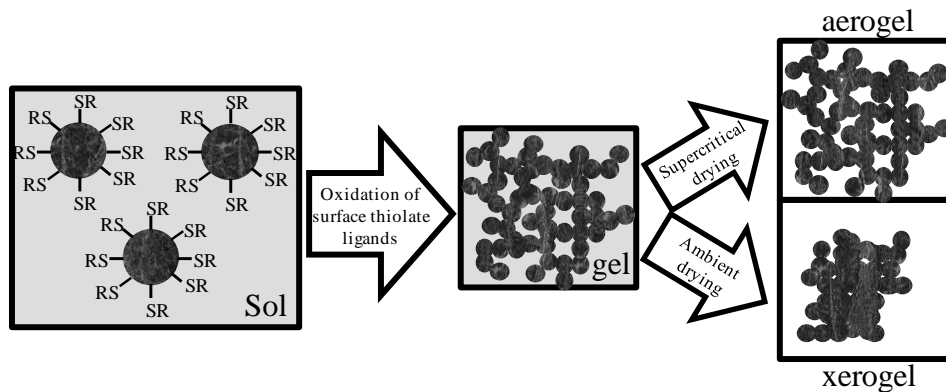


**Figure 1.10** Schematic representation of metal chalcogenide aerogel/xerogel synthesis. Oxidation and removal of thiolate ligands from the surface of metal chalcogenide NCs using a suitable oxidant initiates the gelation process and the resultant gels can be dried under ambient conditions to form a xerogel or by supercritical drying to yield aerogel.

According to the proposed gelation mechanism, removal of surface thiolate ligands exposes the  $\text{Cd}^{2+}$  cations on the NC surface in the case of CdSe NCs, and  $\text{Cd}^{2+}$  can be solvated, exposing  $\text{Se}^{2-}$  anions to the oxidizing environment.  $\text{Se}^{2-}$  anions can be oxidized by the oxidant and this leads to formation of diselenide bonding between NCs which initiates the aggregation process (Figure 1.11).<sup>56</sup> These inter-NC connections should provide better electronic communication in the NC assemblies prepared by sol–gel process compared to other self assembly methods and evaluation of the charge transport properties of sol–gel materials is one of the main objectives of this dissertation research.

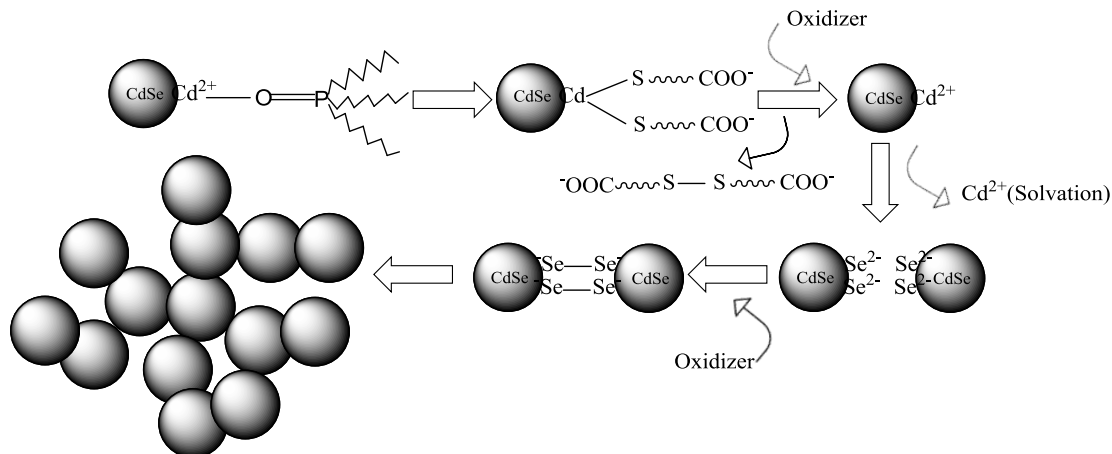


**Figure 1.11** Proposed gelation mechanism for metal chalcogenide NCs (adapted from Pala).<sup>56</sup>

### 1.5 Charge Transport in Semiconductor NC Films

Semiconductor NC thin films have shown great promise in optoelectronic devices such as field-effect transistors (FETs),<sup>57,58</sup> photodetectors,<sup>59,60</sup> light emitting diodes (LEDs)<sup>61,62</sup> and solar cells<sup>63,64</sup> due to their impressive optical properties and solution processability. The charge transport properties of semiconductor NC thin films play a key role in device performance, and this section discusses the mechanisms of charge transport in semiconductor NC films along with some major studies published over the last decade with the aim of improving charge transport in NC films.

Electrical conductivity,  $\sigma$ , in semiconductor NC thin films is dominated by carriers injected from electrodes, created by photooxidation, induced in the channel of FETs, or created by deliberate doping (chemical or electrochemical). This is because there is a low density of intrinsic carriers as the bandgap is much larger than the thermal energy,  $k_B T$ , at room temperature.<sup>12</sup> The energy levels of the NCs are confined within the individual NCs, and therefore, tunneling of charge carriers in NC thin films primarily depends on the quantum

mechanical coupling between the energy levels, which can be expressed in terms of a coupling energy,  $\beta$ , as<sup>56</sup>

$$\beta \approx h\Gamma \quad (1.9)$$

where  $\Gamma$  is the tunneling rate between two orbitals on adjacent NCs and it is strongly dependent on the inter-NC distance. Therefore, enhancement of electronic coupling between NCs via reduction of inter-NC distance is a powerful tool to improve the electrical conductivity in metal or semiconductor NC films. In the weak-coupling regime where  $\beta \ll k_B T$ , unperturbed energy levels of individual NCs exist and charge carrier transport occurs by incoherent hopping between neighboring NCs (Figure 1.12a). In the strong-coupling regime, where  $\beta \gg k_B T$ , coherent molecular-type orbitals that are formed by overlapping of the wave functions, extend over several NCs (Figure 1.12b).<sup>56</sup>

The coulombic charging energy,  $E_c$ , and disorder in the energy levels,  $\Delta\alpha$ , also play an important role in charge transport in NC films. Coulombic repulsion caused by the injection of an additional charge carrier gives rise to  $E_c$ , and the size and shape distribution of NCs results in dispersion of the energy levels,  $\Delta\alpha$ . Furthermore, disorder in inter-NC spacing is also critical for electrical transport in NC films. As described in the previous paragraph, formation of minibands due to the overlapping of wave functions is possible when  $\beta \gg E_c$  or  $\Delta\alpha$ , and metallic like conductivity can be observed in the NC film. When  $\beta \gg \Delta\alpha$ , this sudden increase of conductivity is known as Mott metal-insulator transition (MIT) or Anderson metal-insulator transition when  $\beta \gg E_c$ .<sup>56</sup>

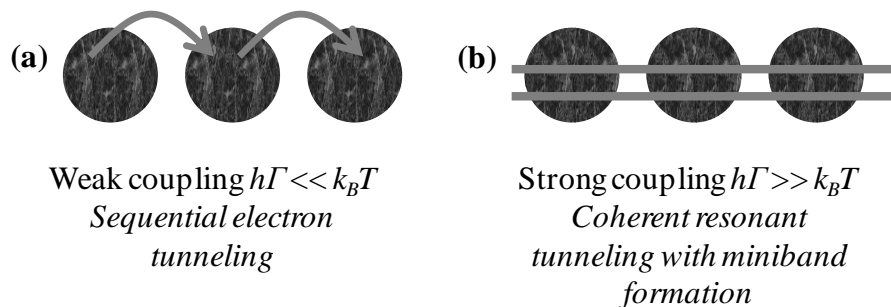


**Figure 1.12** Electronic interactions in a NC film where (a) weak electronic coupling results in unperturbed energy levels whereas (b) strong electron coupling results in miniband formation (adapted from Vanmaekelbergh).<sup>65</sup>

As discussed in section 1.2, ligands with long hydrocarbon chains are utilized in the solution phase synthesis of NCs, and these ligands stabilize NCs in solution and have a significant impact on controlling the kinetics of nucleation and growth of NCs. However, once ligand-capped NCs are assembled into thin films, these bulky ligands form a highly insulating barrier and decrease the inter-NC coupling, resulting in poor charge transport properties. Ligand exchange and annealing strategies are utilized to remove these bulky organic surfactants, which in turn reduce the inter-NC spacing and increase the quantum mechanical coupling of energy levels between neighboring NCs. Zabet-Khosousi et al. reported a Mott metal-insulator transition in films of alkanedithiol ( $\text{HS}(\text{CH}_2)_n\text{SH}$ ) cross-linked Au NCs when  $n \ll 4$ , since finite resistance,  $R$ , was observed at low temperatures.<sup>66</sup> When  $n \gg 6$ ,  $R$  increased rapidly at low temperature, confirming the nonmetallic behavior. Details of the mechanism of charge transport in metal NC films that show nonmetallic behavior can be obtained by measuring the dependency of  $\sigma$  on  $T$ , which can be expressed in the form of<sup>67</sup>

$$\sigma \approx \exp[-(T_0/T)^\nu] \quad (1.10)$$

where  $T_0$  is a constant and  $\nu$  ranges from 0 to 1. When  $\nu$  is equal to one, an Arrhenius type temperature dependence of conductivity is observed and charge carrier transport in the NC film occurs by nearest-neighboring hopping (NNH).  $\nu = 1/2$  is also frequently observed in metal NC films in the nonmetallic regime, and Efros-Shklovskii variable range hopping (ES-VRH) is one of the most common mechanisms that were modeled to explain this behavior. According to the VRH model, which was first proposed by Mott, the temperature dependence of the conductivity in three dimensional systems can be expressed as<sup>12</sup>

$$\sigma \approx \exp[-(T_0/T)^{1/4}] \quad (1.11)$$

where,  $T_0 = 24\pi a^3 g_0 k_B$ ,  $a$  is the characteristic localization length for the electron wave function and  $g_0$  is the density of states. In the VRH mechanism, hopping occurs via the path with the lowest activation energy, and hopping to more distant NCs may be favorable compared to the nearest-neighbor NCs. Below a certain critical temperature,  $T_C$ , Coulomb interactions are significant and Efros and Shklovskii extended the VRH model (ES-VRH) as<sup>12</sup>

$$\sigma \approx \exp[-(T_0/T)^{1/2}] \quad (1.12)$$

where  $T_C = e^4 a g_0 / (4\pi\epsilon_0\epsilon)^2 k_B$ . Several other charge transport mechanisms (e.g., cotunneling, quasi-localized hopping) have been also proposed to explain fractional- $\nu$  behavior in the temperature dependence of  $\sigma$ .<sup>67</sup>

The strength of the inter-NC coupling plays a significant role in the charge transport mechanism in semiconductor NC films. Bawendi et al. studied the charge transport properties of TOPO-capped CdSe NC films deposited on a lateral gated device and the NC films showed very low conductivity ( $\sim 10^{-14}$  S  $\text{cm}^{-1}$  below 200 K) due to significantly high inter-dot spacing ( $> 1.0$  nm).<sup>68</sup> Greenham et al. have studied the current–voltage characteristics of TOPO capped NC films sandwiched between metal electrodes and the estimated electron mobility from

photocurrent measurements of these films. Mobilities were extremely low ( $10^{-4}$ - $10^{-6}$   $\text{cm}^2 \text{V}^{-1} \text{S}^{-1}$ ) even at very high fields ( $10^7 \text{Vm}^{-1}$ ).<sup>69</sup> The films showed Arrhenius behavior in the temperature dependent ( $\sim 300$ - $180$  K) conductivity studies as a result of the activated NNH mechanism of electron transport. Guyot-Sionnest et al. were able to achieve higher conductivity and mobility in CdSe NC films by ligand exchange and electrochemical doping. TOPO-capped CdSe NCs were deposited on a Pt interdigitated array electrode with  $5 \mu\text{m}$  separation, and bulky TOPO ligands were exchanged with 1,4-phenylenediamine and  $1\text{S}_e$  states were filled in an electrochemical cell using a CdSe covered interdigitated array electrode as the working electrode.<sup>57</sup> The extracted conductivity and mobility values from the electrochemical measurements were  $\sim 10^{-2} \text{S cm}^{-1}$  and  $\sim 10^{-2} \text{cm}^2 \text{V}^{-1} \text{S}^{-1}$  respectively. At low electric fields, conductivity followed an ES-VRH model in the temperature range between 10 K and 120 K.<sup>70</sup>

Currently, charge transport studies in NC films are frequently done by fabricating FET devices. Talapin et al. improved the electrical conductivity of CdSe NC arrays by increasing the inter-NC coupling by ligand exchange and heat treatment. In order to evaluate the charge transport properties, FET devices were fabricated by spin coating CdSe NCs capped with a molecular metal chalcogenide complex,  $\text{In}_2\text{Se}_4^{2-}$ , onto  $\text{SiO}_2/\text{Si}$  substrates ( $\text{SiO}_2$  as the gate dielectric and Si as the gate) and subsequently annealed at  $200^\circ\text{C}$  for 30 min.<sup>71</sup> The source and drain Al electrodes were thermally evaporated onto the NC films. Significantly high electron mobility ( $16 \text{cm}^2 \text{V}^{-1} \text{S}^{-1}$ ) was rationalized by band-like electron transport in NC films due to the enhancement of individual NC coupling as a result of reduction of inter-NC space and annealing. Kagan et al. reported room temperature Field-effect mobility for electrons in CdSe NC films as high as  $27 \text{cm}^2 \text{V}^{-1} \text{S}^{-1}$ .<sup>72</sup> FET devices were fabricated by spin coating thiocyanate-exchanged NCs onto  $\text{Al}_2\text{O}_3/\text{SiO}_2/\text{Si}$  substrates ( $\text{Al}_2\text{O}_3/\text{SiO}_2$  as gate dielectric stack and Si as gate) followed

by thermal deposition of In/Au source and drain electrodes on the NC films. Devices were annealed at 250 °C for 10 minutes. The annealing causes the decomposition of thiocyanate ligands, which in turn further reduces the inter-NC spacing. Furthermore, doping of the NC film due to thermal diffusion of In during the annealing process saturates the trap states formed during the removal of surface thiocyanate ligands. They claimed that ligand exchange and annealing steps enhance the NC coupling, resulting in band formation due to delocalization of the electron and hole wave function over multiple NCs within the film. Moreover filling of trap states by In doping raises the Fermi energy and provides access to the bands. In both these studies, band-like transport is confirmed by the increase of electron mobilities with decreasing temperature (~300-220 K range).

## 1.6 Thesis Statement

Sol–gel methods provide a tried and true approach for linking semiconductor nanocrystals (NCs) into three-dimensional architectures (i.e., gels, xerogels, and aerogels) while preserving the properties of individual NCs.<sup>47, 73, 74</sup> Thus, gel materials prepared from semiconductor NCs retain the characteristic size- and shape-dependent optical and electronic properties, making them promising materials for use in optoelectronic device applications based on semiconductor NCs, such as field-effect transistors (FETs),<sup>57, 58</sup> photodetectors,<sup>59, 60</sup> light emitting diodes (LEDs)<sup>61, 62</sup> and photovoltaics.<sup>63, 64</sup> On the other hand, linking of NCs without the presence of intervening ligands should provide facile electronic communication between adjacent NCs, which remains a key hurdle in the development of NC-based devices.

The dissertation work is focused on achieving two main goals: 1) optimization of gelation conditions in order to tune the properties of the resultant gel structures with the aim of addressing application-specific needs; 2) incorporation of gel materials into device architectures for

evaluation of intrinsic properties and assessment of suitability for optoelectronic applications.

The dissertation research has three specific aims in order to achieve these goals.

- I. Ascertain the physical mechanism of gelation en route to controlling the optical quality of the gels
- II. Establish methods to prepare sol–gel films and determine their electro-optical properties
- III. Utilize chalcogenide gel materials to fabricate photovoltaic devices

Aim I. Ascertain the physical mechanism of gelation en route to controlling the optical quality of the gels (presented in Chapter 3)

CdSe/ZnS core/shell gel materials have potential to be used in optoelectronic applications due to the dominance of quantum size effects in the electronic structure, which enables the optical properties to be tuned within the visible region, and the absence of non radiative recombination pathways (achieved by overcoating the CdSe NC core with the ZnS shell) giving rise to intense band-edge emission.<sup>75</sup> However, typical gelation conditions result in opaque CdSe/ZnS gel materials, which is one of the major obstacles for their use in optoelectronic applications such as LEDs. In 2001, Gacoin and co-workers showed that the degree of transparency of CdS gels depends on the nature and concentration of the oxidant.<sup>76</sup> Accordingly, in this dissertation research, the mechanism and kinetics of aggregation of two sizes of 11-mercaptopundecanoic acid (MUA)-capped CdSe/ZnS NCs, as a function of oxidant concentration [tetranitromethane, (TNM)], were studied by means of time resolved dynamic light scattering (TRDLS). The structural characteristics of the resultant gels were probed by optical transmission, transmission electron microscopy (TEM), and small-angle X-ray scattering (SAXS). The kinetics of aggregation of CdSe/ZnS NCs were found to have a significant impact on the macroscopic

properties (i.e., transparency) of the resultant gels and this allows the transparency of the chalcogenide gels to be tuned in order to address application-specific needs in optoelectronics.

Aim II. Establish methods to prepare sol–gel films and determine their electro-optical properties (presented in Chapter 4)

In order to incorporate chalcogenide gel materials into device architectures, it is essential to fabricate gel materials in film form. In this dissertation research, methods of fabricating both micron- and submicron-thick sol–gel NC films are introduced. Gelation conditions that lead to transparent CdSe/ZnS gel structures were exploited to create transparent micron-thick CdSe/ZnS xerogel films. Films were deposited by immersing a glass substrate horizontally in the pre-oxidized sols, gelling and drying under ambient conditions. CdSe/ZnS xerogel films exhibited strong photoluminescence and high conductivities ( $\sim 10^{-3} \text{ S}\cdot\text{cm}^{-1}$ ). However, the films were rough, and attempts to make crack-free thinner films by this approach were not successful.

High quality thin sol–gel NC films were deposited by spin coating sols of thioglycolic acid-capped CdSe and CdSe/ZnS NCs onto substrates and dipping the films into an oxidizing solution (TNM in acetone). Optical, structural and electrical properties of the sol–gel films were evaluated and the films were found to exhibit superior charge transport properties, as shown by a dramatic enhancement of electrochemical photocurrent under white light illumination relative to thin films composed of ligand-capped NCs. This suggests that the sol–gel approach may yield NC thin films suitable for a range of optoelectronic applications.

Aim III. Utilize chalcogenide gel materials to fabricate hybrid photovoltaic devices (presented in Chapter 5)

Photovoltaic technologies based on semiconductor NCs have significant importance due to the increasing demand for inexpensive, reliable and renewable energy. However the poor

charge transport properties of the NC phase remains a significant challenge to improve the performance of NC photovoltaics.<sup>77</sup> Sol–gel chalcogenide materials, which have the potential to provide enhanced electronic conductivity through an interconnected chalcogenide NC network, should be well-suited for photovoltaic applications. In this dissertation research, composite films of both CdSe and CdSe/ZnS aerogels, with poly(3-hexylthiophene) (P3HT) were evaluated for hybrid photovoltaic devices by analyzing the variation of morphology and photocurrent generation with the composition of the hybrid film. Compared to films composed of ligand capped, physically aggregated NCs and P3HT, areogel/P3HT films showed increased photocurrent and charge generation, suggesting the use of chalcogenide aerogel materials for hybrid photovoltaic applications is feasible.

## CHAPTER 2

### EXPERIMENTAL METHODS

This chapter outlines the materials and synthetic procedures that were used to synthesize nanocrystals (NCs) and their assemblies, and discusses the basic concepts of, and instrumentation for, material characterization. Chalcogenide NCs were synthesized by solution-phase synthesis, and structural, morphological and optical properties were characterized by powder X-ray diffraction (PXRD), transmission electron microscopy (TEM), scanning transmission electron microscopy (STEM), energy dispersive spectroscopy (EDS), UV–visible spectroscopy and photoluminescence (PL) spectroscopy. Sol–gel methods were employed to assemble metal chalcogenide NCs into different architectures, namely monoliths and films. Kinetics of aggregation and gelation of NCs were studied by performing dynamic light scattering (DLS) and small-angle X-ray scattering (SAXS). Wet gel monoliths were dried by supercritical CO<sub>2</sub> drying to form aerogel monoliths and sol–gel methods were utilized to fabricate xerogel films under ambient conditions. Aerogel and polymer mixtures were used to fabricate hybrid films, and both xerogel films and hybrid films were characterized by performing X-ray diffraction (XRD), field emission scanning electron microscopy (FESEM), atomic force microscopy (AFM), UV–visible spectroscopy, PL spectroscopy, and Fourier transform infrared (FTIR) spectroscopy. Charge transport properties in films were evaluated using the van der Pauw method and by performing photoelectrochemical measurements.

#### 2.1 Materials

Selenium powder (99.5%), stearic acid (95%), diethylzinc (1M, in hexane), bis(trimethylsilyl)sulfide, trioctylphosphine oxide (TOPO, 90%), tetranitromethane (TNM), and 11-mercaptopundecanoic acid (MUA, 95%), thioglycolic acid (98%) were purchased from

Aldrich. Trioctylphosphine (TOP, 97%) and cadmium oxide (99.999%) were purchased from Strem Chemicals. 1-tetradecylphosphonic acid (TDPA, 98%) was purchased from Alfa-Aesar and tetramethylammonium hydroxide pentahydrate (TMAH, 97%) was purchased from ACROS. Toluene, methanol and ethyl acetate were purchased from Mallinckrodt. TOPO was distilled before use; all other chemicals were used as received.

## **2.2. Synthetic Methods**

### **2.2.1 Synthesis of Metal Chalcogenide Nanocrystals (NCs), Ligand Exchange, and Sol–gel Assembly (Gel Monoliths and Sol–gel Films)**

Synthetic procedures for NCs are described in chapter 3-5 in detail along with purification, ligand exchange, and sol–gel assembly procedures. Precursors were prepared in an inert-atmosphere glove box, and synthetic steps were performed under inert atmosphere using Schlenk line technique.

### **2.2.2 Aerogel Production via Supercritical CO<sub>2</sub> Drying**

Drying wet gel monoliths without significantly impacting the pore structure was achieved by supercritical drying. In the supercritical drying process, the gel is first heated above the critical temperature ( $T_c$ ), and pressurized above the critical pressure ( $P_c$ ), of the pore liquid. As illustrated in Figure 2.1, above the  $T_c$  and  $P_c$  of the liquid, the liquid-vapor phase boundary does not exist and liquid and vapor densities become equal. The supercritical solvent can be slowly evacuated as a gas without affecting the pore structure due to the absence of liquid-vapor interface which corresponds to an absence of capillary forces on the pore walls that can lead to collapse during drying. Liquid CO<sub>2</sub> is a convenient solvent for the supercritical drying process because of its low critical temperature (31 °C) and pressure (7.36 MPa).<sup>78</sup> However, an

additional solvent exchange-step with acetone is required, as liquid CO<sub>2</sub> is not miscible with other common solvents such as methanol and ethanol.

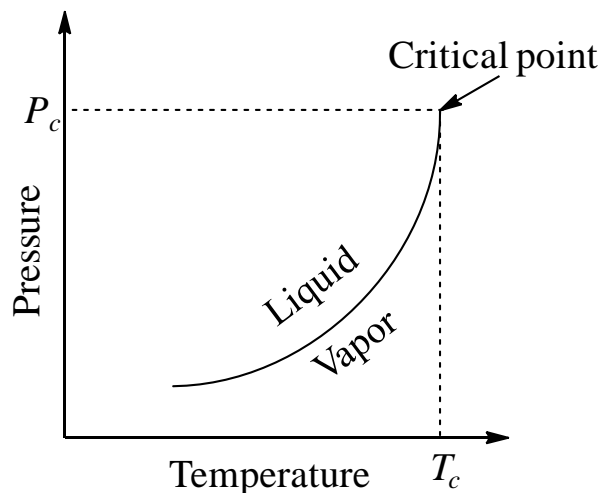


**Figure 2.1.** A phase diagram showing the liquid-vapor phase boundary and the critical point above which densities of the liquid and vapor are similar (adapted from Brinker).<sup>78</sup>

In the dissertation research, a SPI-DRY model critical pointer dryer was used to dry acetone-exchanged wet gel monoliths. Wet gel monoliths were placed in the drying chamber and acetone was exchanged with liquid CO<sub>2</sub> for four hours. During this period, chamber was drained several times and refilled with liquid CO<sub>2</sub>, and then the temperature of the chamber was increased up to 39 °C and the pressure was maintained above the critical pressure of CO<sub>2</sub> for one hour in order to form supercritical liquid. Finally, pressure of the chamber was vented slowly while maintaining the temperature at 39 °C. The temperature of the chamber was controlled by Fisher Scientific ISOTEMP 10065 temperature controller.

## 2.3 Material Characterization Techniques

### 2.3.1 Dynamic Light Scattering

The interaction of light (ultraviolet, visible, and infrared regions in the electromagnetic spectrum) with materials results in absorption, scattering, or both, depending on the wavelength of the light and optical properties of the material. Absorption of light and subsequent radiative emission (fluorescence or phosphorescence) is utilized in several optical spectroscopic techniques such as UV–visible spectroscopy, PL spectroscopy, etc. Light scattering occurs due to the emission of light from the oscillation or perturbation of the electron cloud of the material, caused by the electric-field component of the incident light, and can be categorized into elastic, quasi-elastic, and inelastic light scattering. In elastic or quasi-elastic light scattering, the frequency of light emitted during the scattering process is similar to the frequency of the incident light. However, in inelastic scattering, frequency of scattered light is differs from the frequency of the incident light, as in the cases of Raman and Brillouin scattering.

When light passes through a medium of suspended particles, elastic scattering takes place, and depending on the particle dimensions, two types of scattering processes can be seen. If the diameter of the particles,  $r$ , is much smaller than the wavelength of the incident light,  $\lambda$ , ( $r < \lambda/10$ ), light scattering can be described by Rayleigh theory. As illustrated in Figure 2.2, the scattering intensity,  $I$ , is equal in both forward and backward directions, and is strongly dependent on the wavelength ( $I \propto 1/\lambda^4$ ) in Rayleigh scattering. However, if the particle diameter is comparable to or greater than the wavelength of incident light, ( $r > \lambda/10$ ), more light is scattered in the forward direction, and the light scattering is much less dependent on the wavelength, and can be described by Mie theory.

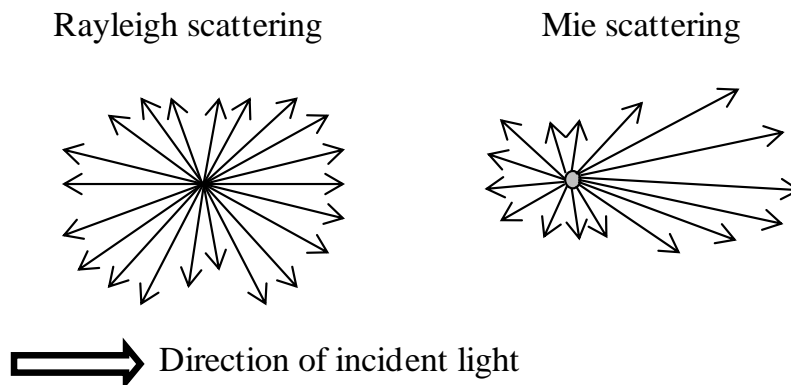


**Figure 2.2.** Two types of elastic light scattering: Rayleigh scattering and Mie scattering.

A typical DLS instrument consists of a light source, two sets of optical elements to transmit the beam and to collect the scattered light, a sample module, a detection system, a correlator, and a computer, as schematically shown in Figure 2.3.<sup>79</sup> A He-Ne Laser is the most commonly used light source, and the light is transmitted and delivered to the sample module, which consists of sample holder and sample cell, by a set of delivering optics. Light is scattered by the particles in the sample, and the scattered light is collected at a specified angle and directed to the detector (photomultiplier tubes or photodiodes) by the collecting optics. After digitizing the signal by electronics, it is fed into the correlator that constructs the autocorrelation function, and this information is then passed to the computer that performs the data analysis.

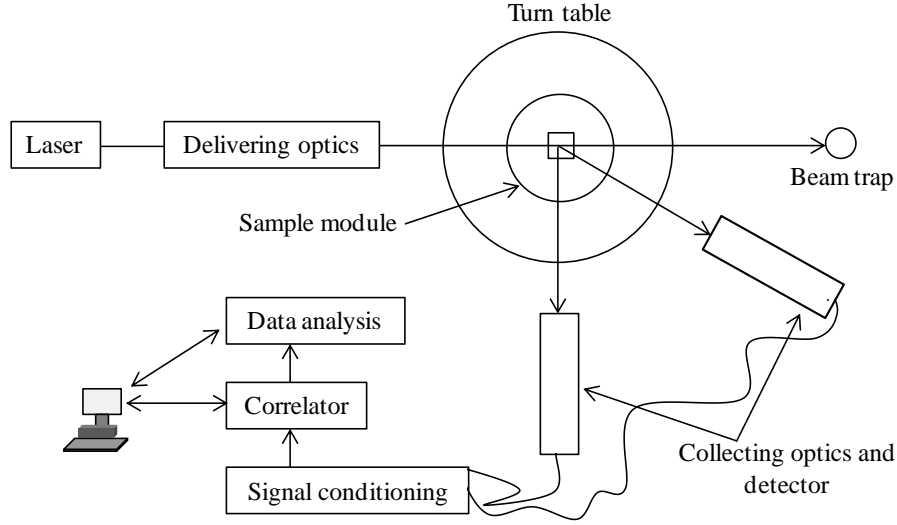


**Figure 2.3.** Schematic diagram of a DLS instrument (adapted from Xu).<sup>79</sup>

Because of the Brownian motion of the particles, the intensity of the scattered light fluctuates with time and the normalized second-order intensity correlation function  $g^{(2)}(\tau)$  can be obtained with the digital correlator in the DLS instrument by autocorrelation of these intensity fluctuations over a very short time interval

$$g^{(2)}(\tau) = \frac{\langle I(0)I(\tau) \rangle}{\langle I(0) \rangle^2} \quad (2.1)$$

where  $I(\tau)$  is the scattering intensity and  $\tau$  is the decay time.  $g^{(2)}(\tau)$  can be related to the normalized first-order electric field correlation function  $g^{(1)}(\tau)$  by the Siegert relation<sup>80,81</sup>

$$g^{(2)}(\tau) = B(1 + \beta |g^{(1)}(\tau)|^2) \quad (2.2)$$

where  $B$  is the base line of the correlation function and  $\beta$  is the coherence factor. For monodisperse solutions,  $g^{(1)}(\tau)$  decays exponentially,

$$g^{(1)}(\tau) = \exp(-\Gamma\tau) \quad (2.3)$$

where  $\Gamma$  is the decay rate. However, for polydisperse solutions,  $g^{(1)}$  must be represented as a sum or distribution of exponentials

$$g^{(1)}(\tau) = \int G(\Gamma) \exp(-\Gamma\tau) d\Gamma ; \int G(\Gamma) d\Gamma = 1 \quad (2.4)$$

where  $G(\Gamma)$  is the distribution function of  $\Gamma$ .<sup>82</sup> Analysis of autocorrelation functions using the method of cumulants yields the mean decay rate  $\bar{\Gamma}$  which is equal to  $\bar{D}q^2$  where  $\bar{D}$  is the average translational diffusion coefficient and  $q$  is the scattering vector

$$q = \frac{4\pi n}{\lambda} \sin \frac{\theta}{2} \quad (2.5)$$

where  $n$  is the refractive index of the solvent and  $\theta$  is the scattering angle. The average hydrodynamic radius  $\bar{R}_h$  of spherical particles can be calculated from the Stokes-Einstein relationship

$$\bar{R}_h = \frac{k_B T}{6\pi\eta\bar{D}} \quad (2.6)$$

where  $T$  is the absolute temperature,  $k_B$  is the Boltzmann constant and  $\eta$  is the viscosity of the solvent. Distribution of particle sizes can be obtained using a non-negatively constrained least squares (NNLS) fitting algorithm, which fits multiple exponential terms to  $g^{(1)}$ . The radius of particles measured by DLS technique is referred to as the hydrodynamic radius because it is calculated utilizing the diffusion motion of the particles in a fluid. Therefore, the particle diameter determined by DLS corresponds to the diameter of a sphere which has the same translational diffusion coefficient as the particle in the liquid.

In the dissertation research, time-resolved dynamic light scattering (TRDLS) measurements were performed using a Zetasizer Nano ZS instrument (Malvern Instruments, Westborough, MA) with a He-Ne laser beam at 633 nm and the detector positioned at 173°. In the TRDLS measurements, autocorrelation functions were accumulated for at least 15 s over

different time periods and the size distribution and the Z-average hydrodynamic radius ( $\bar{R}_H$ ) were determined using the Zetasizer software (version 6.2) provided by Malvern.

### 2.3.2 X-ray Diffraction

Diffraction from crystals occurs when the shortest interatomic distances of the crystals is in the same range as the wavelength of the incident radiation. Typically, this requirement is satisfied for X-ray, neutron and electron beams, which are scattered from the electron densities, nuclei, and electrostatic potentials, respectively.<sup>83</sup> X-ray diffraction, based on the wide-angle elastic scattering of X-rays, is one of the most basic and widely used techniques to determine the crystallinity and crystal structures of nanostructured materials, and to identify other structural characteristics related to the crystal structures such as defects and strains.

W. H. Bragg and W. L. Bragg formulated a law that relates the diffraction angle,  $\theta$  (Bragg angle), wavelength,  $\lambda$ , and interplanar distance between the crystallographic planes,  $d$ , by considering the diffraction of X-rays as a mirror reflection of a X-ray beam that is incident on to a set of parallel crystal planes, as illustrated in Figure 2.4. The path difference of the parallel X-ray beams reflected from adjacent crystal planes is  $2X$  which is equal to  $2d \sin \theta$ , and according to Bragg's law, constructive interference takes place when  $2X = n\lambda$ , where  $n$  is an integer and  $\lambda$  is the wavelength of the X-rays.

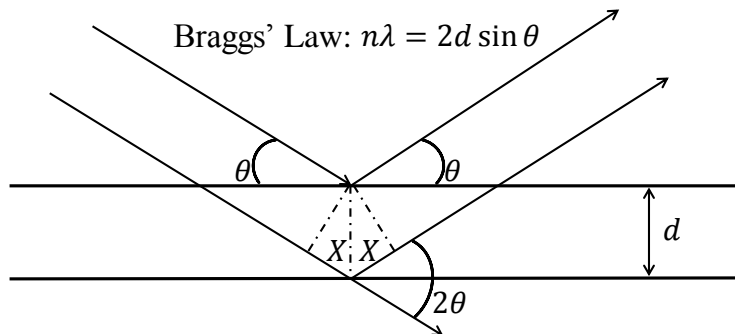


**Figure 2.4.** Geometrical illustration of X-ray diffraction on a set of parallel crystal planes (adapted from Pecharsky).<sup>83</sup>

X-rays can be produced using an X-ray tube (sealed tube or rotating anode tube) in which high energy electrons collide with a metal target (commonly Cu). This impact dislodges electrons from the K shell, and consequently, X-rays are generated by transition of electrons from the L and M shells to the K shell. A typical X-ray spectrum consists of three highly instance characteristic lines ( $K\alpha_1$ ,  $K\alpha_2$  and  $K\beta$ ) and a continuous background, which is known as white radiation. Because of the polychromatic nature and also the angular divergence of the X-rays, focusing optics are used in a diffractometer goniostat to increase the resolution and diffracted intensity. The quality of monochromatization (i.e. extent of elimination of  $K\beta$  and white radiation, and separation of the  $K\alpha_1$  and  $K\alpha_2$  doublet) depends on the method utilized to perform monochromatization of X-ray beam (ex. using a  $\beta$  filter or using diffraction from a crystal monochromator). In order to remove angular divergence, the X-ray beam is collimated in-plane by using divergence slits, and axially by using soller slits. The intensity of the diffracted X-rays is measured using a detector [point detectors such as scintillation detectors, line detectors such as position sensitive detectors (PSD), or area detectors such as charge coupled devices (CCD)].

The orientation of the sample (horizontal or vertical), diffraction geometry, and motion of the goniometer arms play critical roles in designing different diffractometer goniostats. As shown in Figure 2.5, the diffraction geometry can be reflection mode, which is known as Bragg-Brentano focusing geometry, or transmission mode. The diffractometer goniostat can be built to satisfy Bragg's condition by keeping the x-ray source stationary, while rotating the sample and the detector in a synchronized fashion, or keeping the sample stationary while rotating the source and the detector arms.

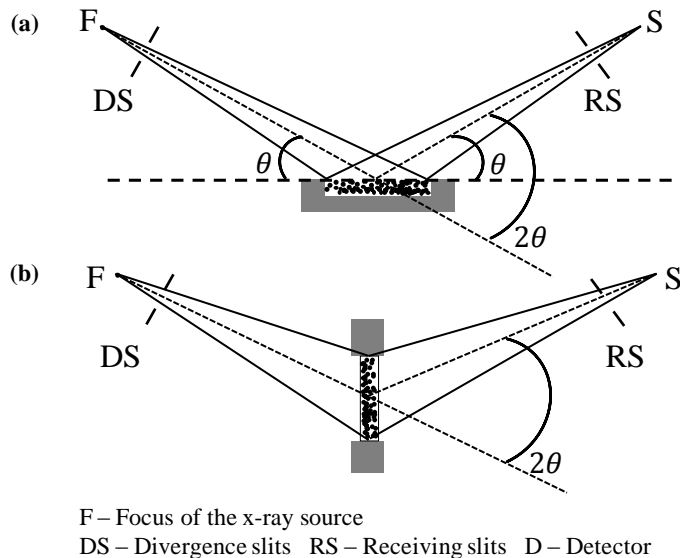


**Figure 2.5.** Types of diffraction geometries (a) reflection mode and (b) transmission mode (adapted from Pecharsky).<sup>83</sup>

In a typical XRD experiment, the intensity of the diffracted X-rays is measured as a function of Bragg angle,  $2\theta$ , which is the angle between the diffracted and incident beams. From a crystalline sample, multiple Bragg reflections can occur from different sets of crystal planes during the  $2\theta$  scan, and this leads to formation of multiple peaks in the XRD pattern. The

position, intensity and shape of these peaks depend on the structure and atomic constituent of the sample. The main structural parameter that determines the peak positions is the unit cell dimensions, and peak intensity is mainly dependent on the atomic structure, which includes the types and spatial distribution of atoms in the unit cell.<sup>83</sup> This allows phase of a crystalline material to be assigned by using the diffraction pattern database that is maintained by the international center for diffraction data (ICDD).

The small crystallite size of nanocrystals results in broadening of XRD peaks due to the presence of a small number of crystal planes (incomplete destructive interfaces due to short coherence length). The size of the nanocrystals can be estimated from the XRD peak broadening using Scherrer equation

$$D = k\lambda/\beta \cos \theta \quad (2.7)$$

where  $D$  is the average crystallite size, and  $\beta$  is the full width at half maximum (FWHM) of the reflection at angle  $\theta$ . The value of  $k$  is close to unity, and depends on the crystallite shape and the reflection used. This is typically chosen to be 0.9 by considering size distribution effects on the Scherrer equation. The size of spherical nanocrystals can be estimated more accurately using following equation<sup>84</sup>

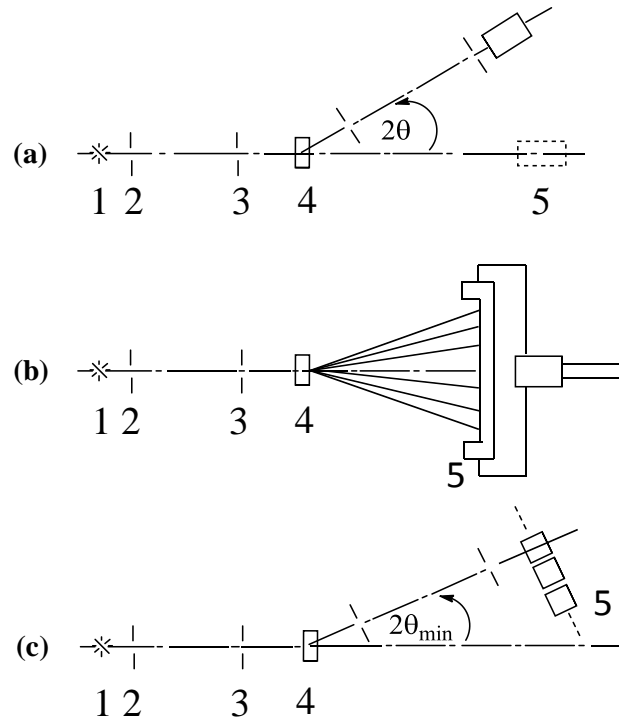
$$D = \frac{4}{3} \left( \frac{0.9\lambda}{\beta \cos \theta} \right) \quad (2.8)$$

In this dissertation research, XRD was performed on a Rigaku Diffractometer (RU200B) using the  $K\alpha$  line of a Cu rotating anode source (40 kV, 150 mA). Films were deposited on glass or silicon substrates for the XRD analysis. Powered samples were attached to a low background quartz holder using a thin layer of vacuum grease.

### 2.3.3 Small-angle X-ray Scattering (SAXS)

X-ray scattering occurs at wide-angles due to the atomic structure of the material as discussed in the section 2.3.2. However, at small angles (typically  $2\theta < 5^\circ$ ), X-rays scatter off inhomogeneous regions (sizes of several nanometers to several tens of nanometers) that arises from differences in electron densities in any material (crystalline or amorphous).<sup>85</sup> Accordingly, small-angle X-ray scattering (SAXS) can be employed to obtain structural information on nanostructured materials, such as particle size of NC systems, structural characteristics of NC assemblies, and pore sizes of porous materials.

SAXS instruments can be categorized into two types according to the X-ray source: instruments that use characteristic X-rays generated by X-ray tubes, or synchrotron radiation. In typical laboratory small-angle X-ray diffractometers, the collimation system (slit collimation system or point collimation system) forms a narrow beam of X-rays generated by the X-ray tube that is introduced to the sample. Scattered intensity can be collected by a detector in sequential or parallel mode.<sup>86</sup> In sequential mode small-angle X-ray diffractometers, the detector (point detectors such as scintillation or proportional counter detectors) is positioned at different angles sequentially to collect the data, as shown in Figure 2.6. In parallel mode diffractometers, the detector is stationary (line detectors such as position sensitive detectors), and it collects scattered intensity simultaneously at all angles. Additionally, a combination of both modes of operation is employed when the scattered intensity is collected using an array of monolithic solid state detectors.



1 – Radiation source 2, 3 – Collimation system  
4 – Sample 5 – Detector

**Figure 2.6.** Outlines of (a) sequential mode data collection using a point detector, (b) parallel mode data collection using a position sensitive detector, and (c) data collection using an array of solid state detectors in SAXS experiments (adapted from Feigin).<sup>87</sup>

Determination of NC size using a dilute dispersion of NCs is one of the most basic applications of SAXS. The SAXS intensity,  $I$ , scattered from a noninteracting  $N$  number of NCs with uniform electron density,  $p$ , dispersed in a homogeneous medium of electron density,  $p_0$ , is given by<sup>88</sup>

$$I(q) = I_0 N (\rho - \rho_0)^2 F^2(q) \quad (2.9)$$

where,  $I_o$  is the intensity of the incident X-ray beam and  $q = (4\pi/\lambda) \sin (\theta/2)$ .  $F(q)$  is the form factor, which is the Fourier transform of the scattering object. For spherical NCs of radius,  $R$ , it can be defined as

$$F(q) = \frac{4}{3}\pi R^3 \left[ 3 \frac{\sin(qR) - qR \cos qR}{(qR)^3} \right] \quad (2.10)$$

In order to determine the NC size, experimental data is fitted to the theoretical model using equation 2.9 and 2.10.

In the dissertation research, SAXS measurements were carried out using a Rigaku SmartLab X-ray diffractometer (40 kV, 44 mA) with Cu  $K\alpha$  radiation. 2.0 mm boron-rich capillary tubes were used as sample holders and scattering intensities were recorded from 0 to 8° 2 $\theta$ . The parasitic scattering produced by the sample holder, slits, and air was subtracted from the experimental scattering intensity.

### 2.3.4 Electron Microscopy

Electron microscopy is a powerful tool to characterize nanostructured materials. In electron microscopy, the interaction of high energy electrons with atoms is employed to obtain a wealth of information about the specimen. When a high energy electron beam impinges on specimen, electrons can be scattered elastically or inelastically. In elastic scattering, the direction of the primary electron beam can change due to the coulombic interactions between the impinging electrons and the atoms in the specimen, which is known as Rutherford scattering, but there is no detectable energy change of the primary electrons. Inelastic scattering occurs when the energy of the primary electrons is transferred to the electrons or atoms in the specimen. The energy of primary electrons can be lost by exciting a phonon (phonon scattering), exciting a plasmon (plasmon scattering), by exciting a single valence electron, or by exciting an inner shell electron. Relaxation of excited atoms due to the excitation of electrons leads to emission of

electromagnetic radiation as a secondary effect. Photons can be emitted during the relaxation if the primary electron beam causes an excitation of an outer shell electron of the specimen atoms, and this effect is known as cathodoluminescence. If the excitation occurs in the inner shell, relaxation takes place by emitting a characteristic X-ray or a characteristic Auger electron (Figure 2.7a and b). Knocking out of a K shell electron by the primary electron beam creates a vacancy in the K shell, and exciting of an electron from the L shell to the vacant site in the K shell emits characteristic  $K\alpha$  X-ray of the atom. Alternatively, instead of emitting an X-ray, an outer shell electron can be ejected which is known as Auger emission. The primary electron beam can also cause emission of X-rays (white radiation) without ejecting electrons from the inner shell, and this process is known as Bremsstrahlung. However these X-rays are not characteristic to the specific atoms. Other secondary effects caused by the primary electron beam include secondary electrons and backscattered electrons. Figure 2.7c summarizes the effects can result from the collision of a high energy electron beam with the specimen.

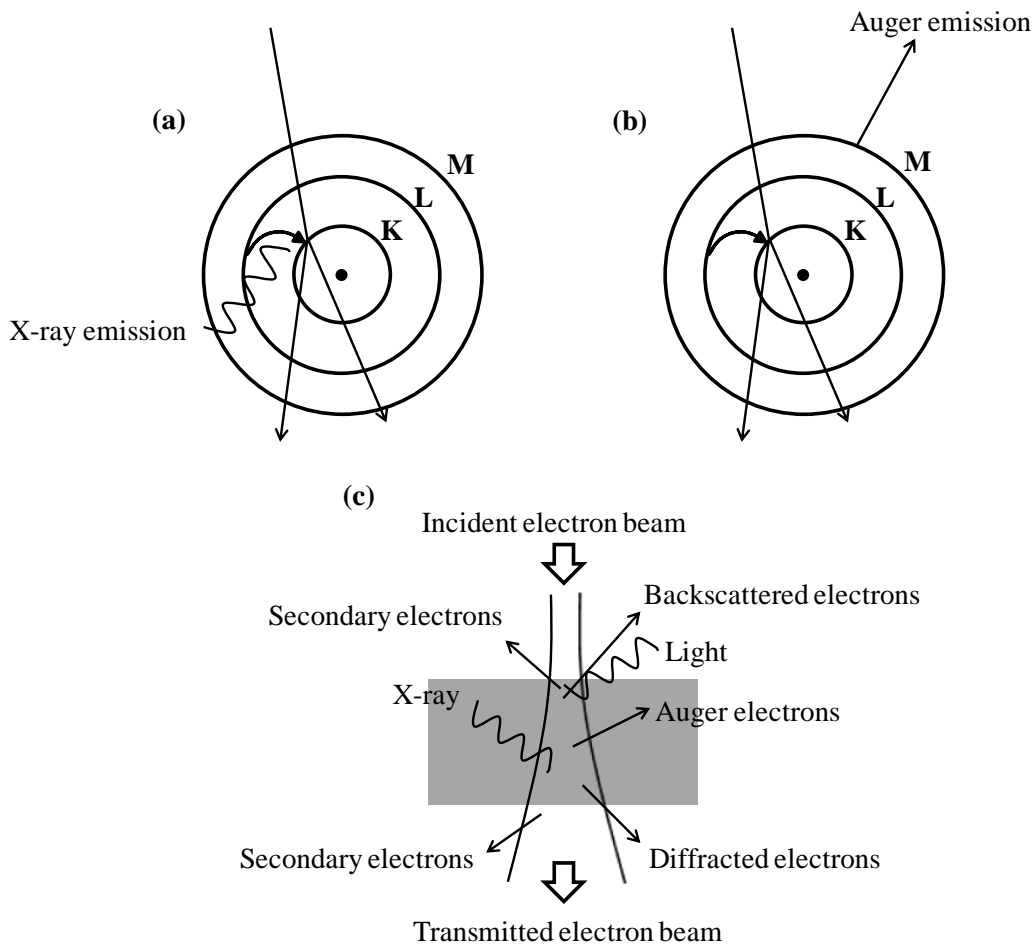


**Figure 2.7.** Two possibilities of relaxation of an inner-shell excited atom: (a) Emission of a characteristic X-ray; (b) emission of an Auger electron, and (c) effects resulting from the interaction of primary electron beam and specimen (adapted from Goodhew).<sup>89</sup>

#### 2.3.4.1 Transmission Electron Microscopy (TEM)

Transmission electron microscopy (TEM) can be employed to obtain structural characteristics, and the capability of direct imaging by TEM at very high magnifications (ranging from 50 to  $10^6$ )<sup>85</sup> permits the size and shape of NCs to be accurately assessed. Figure 2.8 schematically illustrates the major components of a TEM. In the TEM instrument, a high energy electron beam is formed by the electron gun (thermionic gun or field emission gun), in which electrons are generated by thermionic emission (LaB<sub>6</sub> or tungsten filament) or an extremely high

electric field (tungsten tip), and is accelerated [40-400 KeV or higher (up to 1MeV)]<sup>85</sup> using an anode at higher potential. At typical accelerating voltages,  $V$  ( $V \geq (200 \text{ keV})$ ), which are used in common TEMs, relativistic effects must be taken into account to calculate the wavelength,  $\lambda$ , of the electrons

$$\lambda = h / (2eVm_e + (e^2 V^2) / c^2)^{\frac{1}{2}} \quad (2.11)$$

where  $h$  is the Planck's constant,  $m_e$  is the mass of the electron and  $c$  is the velocity of light. The high energy electron beam emitted by the electron gun is then focused onto the specimen by the condenser system which consists of electromagnetic lenses. A side entry double tilt holder, on which a thin specimen on support grid is mounted, is employed to bring the specimen into the specimen chamber. Diffracted electrons from the specimen enter the objective system, and are used to form the first intermediate image and the diffraction pattern. The final resolution of the image is determined by the diameter of the objective aperture of the objective system, and high-voltage TEMs (e.g. 400 keV) have point-to-point resolution better than 0.2 nm.<sup>85</sup>

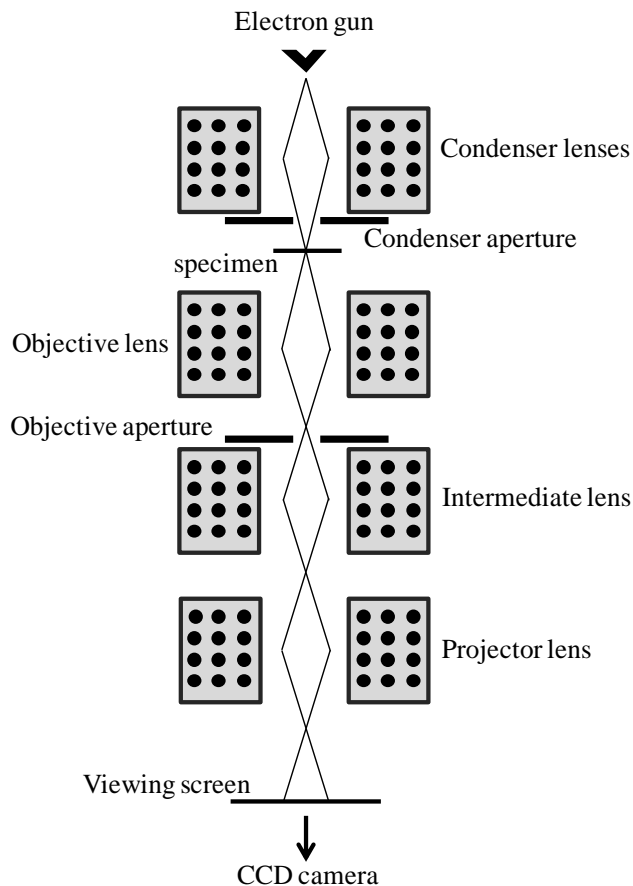


**Figure 2.8** Schematic of a conventional TEM (adapted from Goodhew).<sup>89</sup>

The objective aperture can be utilized to allow passing of either undeflected electrons (bright field imaging) or diffracted electrons (dark field imaging). In the image mode, a series of intermediate and projector lenses further magnify the image formed by the objective lens, and the final image is projected onto the fluorescent screen. In the diffraction mode, the diffraction pattern of a selected area of the specimen is projected onto the fluorescent screen by means of the selected area diffraction (SAD) or convergent beam diffraction (CBD) techniques. The diffraction pattern can be used to determine the Bravais lattice and lattice parameters of crystalline materials similar to XRD. The image or diffraction pattern is typically captured by a charge coupled device (CCD) array camera located under the viewing screen.

In the dissertation research TEM measurements were carried out on a JEOL 2010 transmission electron microscope operated at an accelerating voltage of 200 kV and carbon-coated copper TEM grids were employed as support grids. Samples were dispersed in appropriate solvents and drop casted on to grids.

#### **2.3.4.2 Scanning Electron Microscopy (SEM)**

The scanning electron microscope (SEM) shares many of features of the TEM, however the method of image formation and magnification are completely different, and SEM is mainly employed to image (magnification ranges from ~10 to over 300000)<sup>85</sup>, and to obtain structural characteristics of the surface or near surface region of the specimen. Figure 2.9 shows the schematic diagram of a typical SEM with major components. In a SEM instrument, electrons generated by the electron gun [thermionic gun or field emission gun (FESEM)] are accelerated at comparatively low voltage (1-30 keV).<sup>89</sup> The condenser and objective lenses focus a fine beam of electrons on the specimen, and two sets of coils are used to deflect the beam in order to raster over the surface of the specimen. Once the electron beam hits the specimen, it interacts with the specimen atoms as discussed in section 2.3.4, and the region into which electrons penetrate is known as the interaction volume. Most of the common SEMs use both secondary electrons (for topographic) and back scattered electrons (for both topographic and compositional) imaging processes. Secondary electrons are detected by means of an Everhart-Thornley detector, whereas backscattered electrons are detected with a scintillation detector, a solid-state detector, or a through-the-lens detector.<sup>89</sup> In contrast to TEM, SEM acquires the electrical signal gradually and builds the image pixel by pixel. The size of the incident probe beam and the probe current primarily determine the ultimate resolution of the instrument, which approaches a few

nanometers. SEMs typically have a high depth of focus (field) due to the smaller angle of convergence of the incident beam.

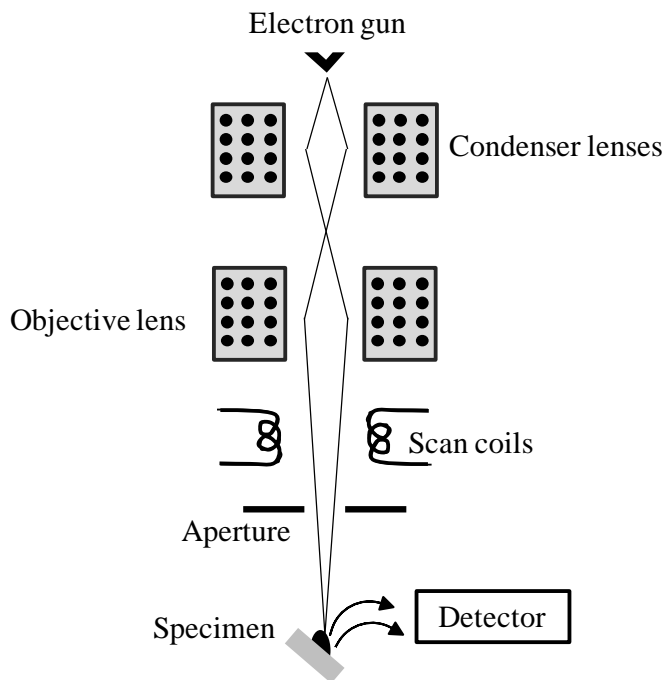


**Figure 2.9** Schematic showing the main components of a SEM (adapted from Goodhew).<sup>89</sup>

In the dissertation study, FESEM images of films deposited on ITO-coated glass substrates were obtained using a JEOL JSM-7600F field emission scanning electron microscope operated at an accelerating voltage of 15 kV in high-vacuum mode.

#### 2.3.4.3 Energy Dispersive Spectroscopy (EDS)

Interaction of high energy electrons with the specimen atoms enables the imaging and structural analysis of nanostructured materials by electron microscopy. Coupling of suitable detectors to the electron microscope allows further use of these interactions for qualitative to quantitative chemical analysis. As discussed in section 2.3.4, the collision of high energy electrons and specimen atoms results in emission of characteristic X-rays whose wavelengths

correspond to the atoms of each element present in the specimen. These characteristic X-rays are utilized for qualitative to semi-quantitative analysis in energy dispersive spectroscopy (EDS). Figure 2.10 illustrates some of the possible transitions that give rise to X-ray lines, and the intensity of these lines can be used to determine the relative amounts of different atoms present in the material.

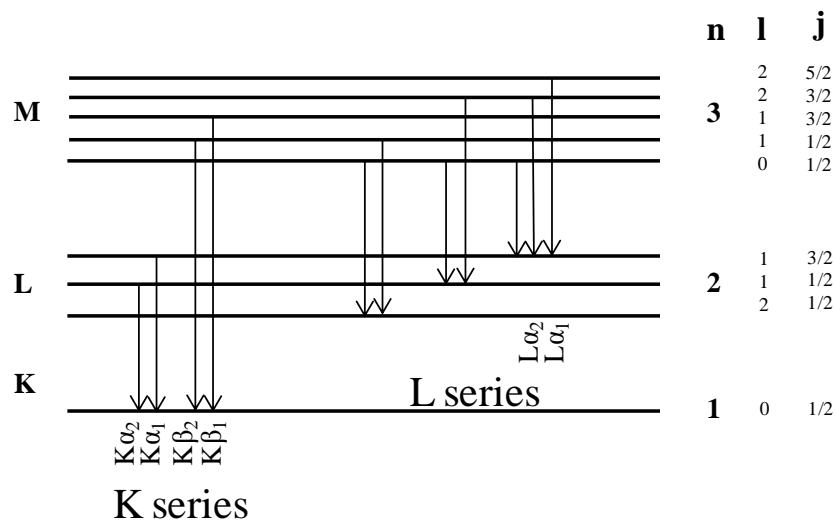


**Figure 2.10.** Common X-ray transitions that lead to lines appearing in an EDS spectrum.

Most of the TEM and SEM instruments are coupled with an EDS detection system, which usually consists of detector crystals such as silicon doped lithium or intrinsic high purity germanium. Because X-rays cannot be deflected, the detector has to be positioned closer to the specimen.<sup>89</sup> In TEM, a fine focused beam is used for qualitative and semi-quantitative analysis of the area of interest. Because of the low energy of the X-ray peaks, lighter elements are difficult to analyze by EDS. Electron energy loss spectroscopy (EELS) is an alternative method to analyze lighter elements by TEM. Spot analysis can also be performed using SEM by stopping the electron beam on the area of interest. Furthermore, SEM has capability of studying the

variation of chemical composition over a selected area by line scanning (one-dimensional scanning) or X-ray mapping (two-dimensional scanning).

In the dissertation study EDS analysis was performed with EDS detectors (EDAX inc.) coupled to both TEM (JEOL 2010 transmission electron microscope) and FESEM (JEOL JSM-7600F field emission scanning electron microscope) instruments.

#### **2.3.4.4 Scanning Transmission Electron Microscopy (STEM)**

Scanning transmission electron microscopy (STEM), which is a combination of TEM and SEM techniques, is a powerful tool to study nanostructured materials. STEM is capable of acquiring transmission images as in TEM, however, a fine focused electron beam is scanned across the specimen instead of illuminating the interested area of specimen at once using a parallel beam. Although some TEM instruments have the ability to operate in STEM mode, the best STEM performance can be achieved in dedicated STEM instruments. Figure 2.11 shows a simplified schematic diagram of a dedicated STEM instrument with various detector systems. A field emission gun is used to generate the electron beam (accelerating voltage ranging from 60 to 300 KeV), and it is focused (beam diameter can be as less 0.1 nm) on to the specimen.<sup>90</sup> Because of the absence of intermediate and projector lenses after the specimen, there is a lot of room for variety of detectors to be added in STEM.

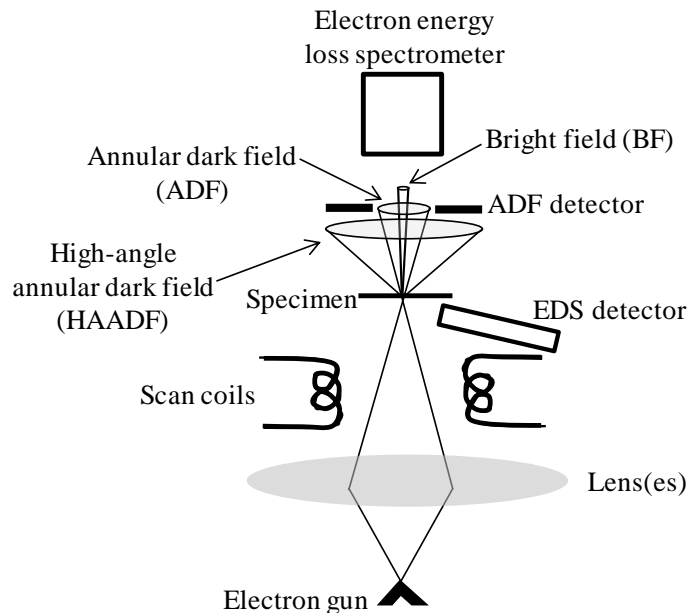


**Figure 2.11.** Schematic of a dedicated STEM (adapted from Goodhew).<sup>89</sup>

As in TEM, undiffracted electrons are collected by a bright field detector to form a bright field image. Diffracted electrons are collected by an annular dark field (ADF) detector in the dark field mode. Additionally, electrons scattered at relatively larger angles can be collected by means of a high-angle annular dark field (HAADF) detector. At the higher angles, the dependency of scattering on the atomic number,  $Z$ , increases. Therefore, this is known as  $Z$ -contrasting imaging, and enables different individual columns of atoms to be distinguished. The greatest advantage of STEM is the capability to obtain spatially resolved analytical information (by EDS or EELS) in parallel with atomically resolved high resolution imaging.

In the dissertation research, STEM images were taken using the FEI Titan 80-200 Scanning Transmission Electron Microscope (S/TEM) operated at 200 kV. In STEM mode,  $Z$ -contrast images were taken using a high-angle annular dark-field (HAADF) detector (Fischione Instruments), and elemental mapping was performed using the “Super X” Energy Dispersive

Spectrometric (EDS) system, which consists of 4 windowless silicon-drift detectors (SDD) positioned symmetrically around the specimen in a unique FEI design. The detectors are made by PN Sensors, utilizing a pulse processor from Bruker Corporation. The integration of Super X EDS detection in combination with the High-Brightness Electron source is also called ChemiSTEM Technology, introduced by the FEI company in 2010.

### **2.3.5 Atomic Force Microscopy (AFM)**

Atomic force microscopy (AFM) is a scanning probe microscopic technique that is often utilized to obtain topographical images of surfaces of nanostructured materials. Image formation in this family of microscopes is based on the strong distance-dependent interactions between a sharp probe/tip and the surface of the sample, and this is different from conventional microscopes in which lenses are a main part of image formation system.

Figure 2.12 shows the main components of an AFM. A nanometer-sharp AFM tip (commonly fabricated from Si, SiO<sub>2</sub> or Si<sub>3</sub>N<sub>4</sub>) mounted on a cantilever (available in diving board or V-shaped geometries) interact with the sample surface, and the tip is raster scanned over the sample surface by a piezoelectric system (usually lead zirconate titanate) that can move with a subnanometer displacement. During the imaging process the tip is brought in contact with, or close to, the sample surface, and scanned over the sample. Depending on the surface topography of the sample surface, the tip moves vertically, and these vertical deflections are detected using a small laser beam reflected off the back side of the cantilever onto a position-sensitive photodiode.<sup>91</sup> Typical vertical and horizontal distance resolutions are around 0.01 and 0.2 nm, respectively, and this allows measuring surface topography with near-atomic resolution.

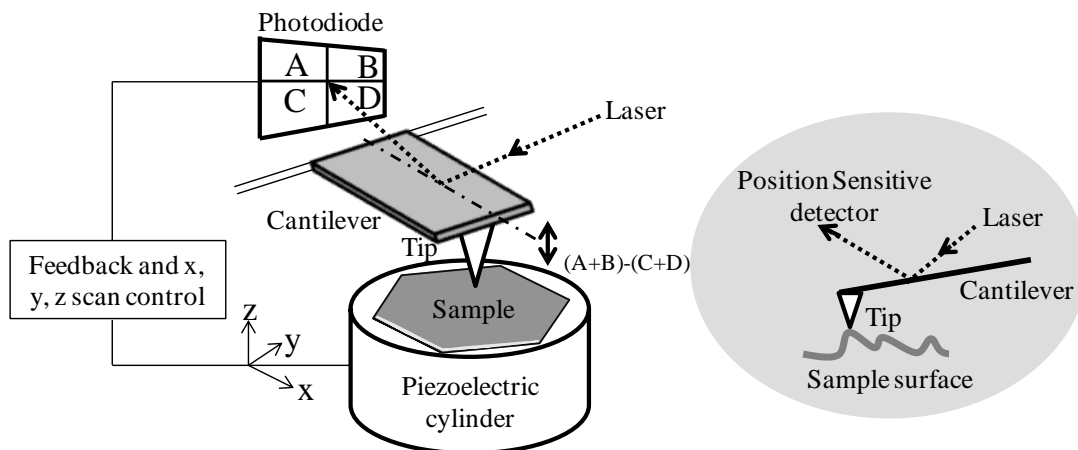


**Figure 2.12.** Schematic of an AFM (adapted from Drelich).<sup>91</sup>

AFM can be operated in two basic modes depending on the scanning dynamics: static mode (contact mode) or dynamic mode (tapping mode or non-contact mode). In contact mode, the tip is in direct contact with the sample surface; in tapping mode, the tip oscillates and taps the surface; and in non-contact mode, it oscillates without touching the surface. In parallel to topographical imaging, the physical properties of nanostructured materials such as mechanical, electrical, thermal and magnetic properties, can be measured by the AFM technique.

In the dissertation research, AFM analysis of NC films deposited on glass substrates was performed using a Dimension 3100 AFM (VEECO) in tapping mode. The surface roughness of the films was measured by using the roughness command (Nanoscope) and film thickness was determined using the sectional height analysis command (Nanoscope). The surface roughness was measured from three areas on the film of  $5 \times 5 \mu\text{m}^2$  each. The film was then scratched carefully with a blade. The film thickness was determined by measuring the depth of the scratch at five locations on the film.

### 2.3.6 Optical Spectroscopy

Optical spectroscopy involves the study of the interaction of light with matter. Optical spectroscopic techniques used in the dissertation research include UV–vis spectroscopy, PL spectroscopy and IR spectroscopy.

#### 2.3.6.1 UV–vis Spectroscopy

In UV–vis spectroscopy, visible and/or ultraviolet light is passed through the absorbing material, and this leads to electronic transitions due to the absorption of photons. The absorbance  $A$  of the sample is defined as

$$A = \log\left(\frac{I_0}{I}\right) = -\log T \quad (2.12)$$

where,  $I_0$  is the intensity of the incident beam,  $I$  is the intensity of the transmitted beam, and  $T$  is the transmittance. Figure 2.13 shows the key components of an UV–vis spectrometer. In a typical UV–vis experiment, the intensity of the light emitted by the light source is measured by the light detector after passing light through the sample chamber without (blank) and with the sample. The signal is then digitized, and processed by the computer to yield an absorption spectrum (a plot of intensity of absorbed light vs light wavelength).

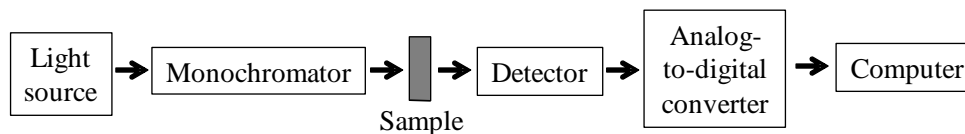


**Figure 2.13.** Block diagram of a UV–vis spectrometer (adapted from Zhang).<sup>92</sup>

The Beer-Lambert law shows the relationship between the absorbance and the concentration of the absorbing species,  $c$

$$A = \varepsilon cl \quad (2.13)$$

where  $l$  is the sample path length and  $\varepsilon$  is the extinction coefficient, which is the probability of absorbing a photon by an absorbing species at a given wavelength.

As discussed in Chapter 1, electronic transitions occur from the valence band to the conduction band in semiconductor NCs. Therefore, a band gap,  $E^*$ , can be calculated from absorption onset, and this can be obtained from the absorption spectrum of semiconductor NCs.<sup>93</sup> The size of spherical semiconductor NCs can be estimated by the relationship between the band gap and NC size using the effective mass approximation model

$$E^* \cong E_g + \frac{\hbar^2 \pi^2}{2r^2} \left( \frac{1}{m_e} + \frac{1}{m_h} \right) - \frac{1.8e^2}{\varepsilon r} \quad (2.14)$$

where  $E_g$  is the bulk band gap,  $\hbar$  is the reduced Planck's constant,  $r$  is the radius of semiconductor NCs,  $m_e$  is the effective mass of the electron,  $m_h$  is the effective mass of the hole,  $e$  is the charge on the electron and  $\varepsilon$  is the semiconductor dielectric constant.<sup>94</sup>

In the dissertation study, UV–vis spectra of solutions or films deposited on glass substrates were obtained with a Cary 50 (Varian Inc.) spectrometer.

### 2.3.6.2 Photoluminescence (PL) Spectroscopy

In PL spectroscopy, light is used to create excited electronic states in the material, and the optical emission produced during the relaxation of excited states is studied. Figure 2.14 shows a typical Jablonski diagram that illustrates the phenomena that can occur in the absorption and emission processes. Absorption of light excites an electron from singlet ground state,  $S_0$ , to a higher vibrational level of the singlet first,  $S_1$ , or second,  $S_2$ , state, and it is relaxed back to the lowest vibrational level of  $S_1$  state within  $10^{-12}$  s or less. This process is known as internal

conversion. Typically, fluorescence (emission rates are close to  $10^8 \text{ s}^{-1}$ ) occurs upon relaxing of the electron from the lowest vibrational level of the  $S_1$  state to a vibrational level of the  $S_0$  state. An excited electron in  $S_1$  state sometimes can undergo a spin conversion to the triplet,  $T_1$ , state which is known as an intersystem crossing. Phosphorescence occurs upon transition from the  $T_1$  state to the  $S_0$  state; however, emission rates are slow ( $10^3$  to  $10^0 \text{ s}^{-1}$ ) due to the spin-forbidden nature of the transition.

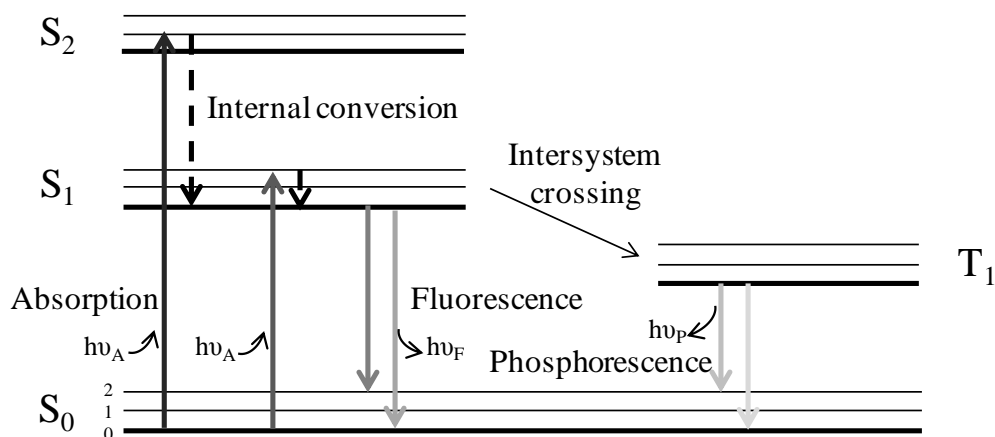


**Figure 2.14.** Jablonski diagram illustrating the processes occurring in the absorption and emission of light (adapted from Lakowicz).<sup>95</sup>

Figure 2.15 illustrates a block diagram of a PL instrument. Light generated by the excitation source is passed to the sample, and emitted light is dispersed in a spectral device, and converted into an electric signal by the detector, and then processed by electronic devices and a control computer to obtain the emission spectrum, a plot of intensity as a function of wavelength of the light.

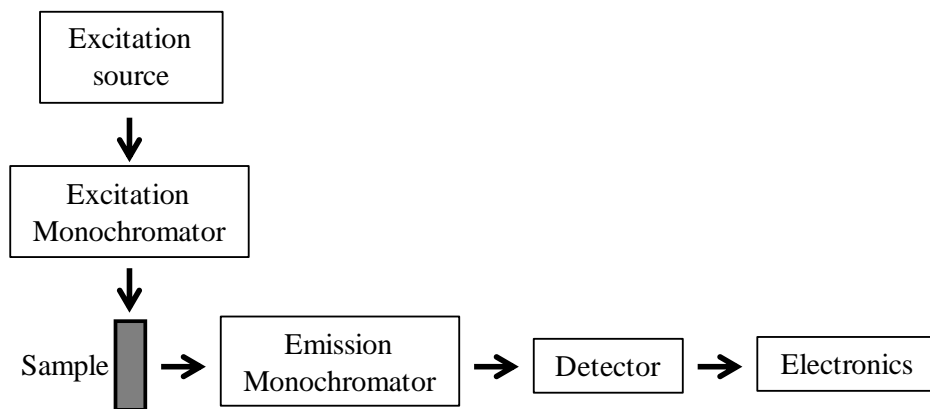


**Figure 2.15.** Block diagram of a PL spectrometer (adapted from Lakowicz).<sup>95</sup>

In semiconductor NCs, photoluminescence occurs due to the recombination of electron-hole pairs as discussed in Chapter 1. PL spectroscopy along with quantum yield measurements and lifetime studies can be utilized to acquire structural information of semiconductor NCs as well as to determine their quality.

In the dissertation study, PL spectra of solutions or films deposited on glass slides were obtained with a Cary Eclipse (Varian, Inc.) fluorescence spectrometer.

### 2.3.6.3 FTIR Spectroscopy

In FTIR spectroscopy, infrared radiation is passed through a sample, and transmitted radiation is measured after absorption of a fraction of the incident radiation by the sample due to vibrational excitations of groups of atoms (functional groups) in the sample. Accordingly, FT-IR spectroscopy is a useful technique for qualitative and semi-quantitative analysis of surface ligands on NCs.

Figure 2.15 shows the basic components of an FTIR instrument. Infrared radiation generated by the source is passed through an interferometer, which produces a signal containing all of the infrared frequencies, to the sample, and the transmitted signal is captured, amplified

and converted to digital by the detector, amplifier, and analog-to-digital converter, respectively. The digital signal is then Fourier transformed by the computer to obtain the final infrared spectrum containing the transmitted intensity at each infrared frequency. The FTIR technique can be used to analyze material in the liquid, solid or gaseous form, and the instrument can be operated in transmission mode or reflectance mode (attenuated total reflectance spectroscopy, specular reflectance spectroscopy or diffuse reflectance spectroscopy).<sup>96</sup>

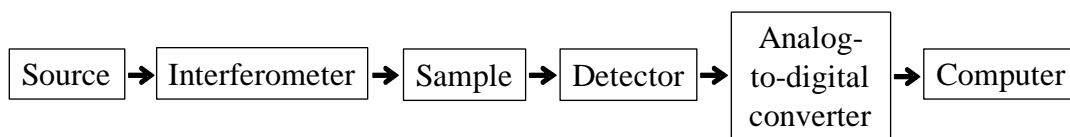


**Figure 2.15.** Block diagram of a FT-IR spectrometer (adapted from Stuart).<sup>96</sup>

In the dissertation research, FT-IR spectra were obtained using a Bruker TENSOR 27 FT-IR spectrometer (Bruker Optics, inc.). Films were deposited on silicon substrates and FTIR spectra were recorded in reflection mode. Aerogels were combined with KBr and pressed into a 15 mm pellet using a Carver Hydraulic Press.

### 2.3.7. Thermogravimetric Analysis (TGA)

Thermogravimetric analysis (TGA) measures the mass of a sample as a function of a temperature program (e.g. gradient temperature program, isothermal temperature program) under a specified atmosphere. A typical TGA curve (weight % vs. temperature) provides information regarding the stability of the material at a certain temperature, the decomposition or evaporation temperature of the material, and the temperature of chemical reactions with the atmosphere.

Accordingly, TGA is an important technique for quantitative analysis of the surface ligands on NCs.

In a TGA instrument, a sensitive balance is housed in a furnace to obtain the changes of the sample weight with temperature, and a purge gas system is used to provide the specified atmosphere for the experiment. According to the orientation of the sample placement in the balance, there are two basic configurations of TGA instruments: horizontal sample placement and vertical sample placement relative to the furnace and the balance. Temperature and balance data are collected and processed by a computer to create the TGA curve. Frequently, TGA instruments are coupled with gas chromatographs, mass spectrometers or FTIR spectrophotometers to obtain information on gaseous effluents.

In the dissertation research, TGA measurements were performed on a Perkin Elmer Pyris 1 TGA under nitrogen flow.

### **2.3.7. Electrical Measurements**

Studying electrical properties of nanostructured materials such as conductivity and dielectric behavior is important for developing nanostructured materials for various electronic applications. As discussed in Chapter 1, semiconductor NC films are extremely useful in a variety of optoelectronic device applications, and evaluation of charge transport properties in these films is a key aspect of performance improvement in optoelectronic devices.

#### **2.3.7.1. Sheet Resistance Measurement by the van der Pauw Method**

Electrical resistance,  $R$ , of a material is one of the basic electrical measurements, and for a film of length,  $l$ , width,  $w$ , and thickness,  $d$ , it can be defined as

$$R = \rho \frac{l}{wd} \quad (2.15)$$

where  $\rho$  is film resistivity. Because in most cases, the  $d$  of the film is much smaller than the lateral dimensions,  $R$  of a square piece of a film ( $l = w$ ) can be expressed as

$$R_S = \frac{\rho}{d} \quad (2.16)$$

where,  $R_S$  is sheet resistance, which is independent of the film dimensions except for  $d$ .

The van der Pauw method is a common technique used to measure the  $R_S$  of metallic and semiconductor NC films. In this technique, two sets of current-voltage measurements ( $V_{CD}, I_{AB}$  and  $V_{DA}, I_{BC}$ ) are performed with ohmic contacts to the film as illustrated in Figure 2.16, and  $R_S$  can be calculated using the van der Pauw equation.<sup>97</sup>

$$\exp\left(-\frac{\pi V_{CD}}{R_S I_{AB}}\right) + \exp\left(-\frac{\pi V_{DA}}{R_S I_{BC}}\right) = 1 \quad (2.17)$$

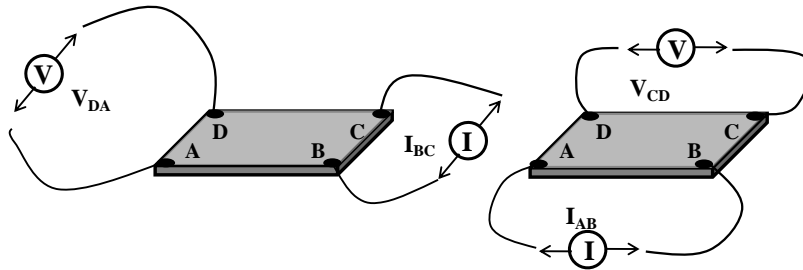


**Figure 2.16.** Sheet resistance measurements by van der Pauw method.

In the dissertation research, sheet resistances of the films deposited on glass substrates were measured using the van der Pauw method with a Keithley 2400 source meter. Four Pt wires and silver paste were used to achieve ohmic contact with the film, defining approximately a square of  $1 \text{ cm}^2$ .

### 2.3.7.2 Photocurrent Measurement and Incident Photon to Current Efficiency (IPCE)

#### Measurement by Photoelectrochemistry

Photocurrent measurement is a quick and easy method to evaluate the charge generation and transport in NC films. Figure 2.17 shows a basic schematic illustration of experimental setup, which is composed of a computer, a potentiostat, and an electrochemical cell, for controlled-potential experiments.

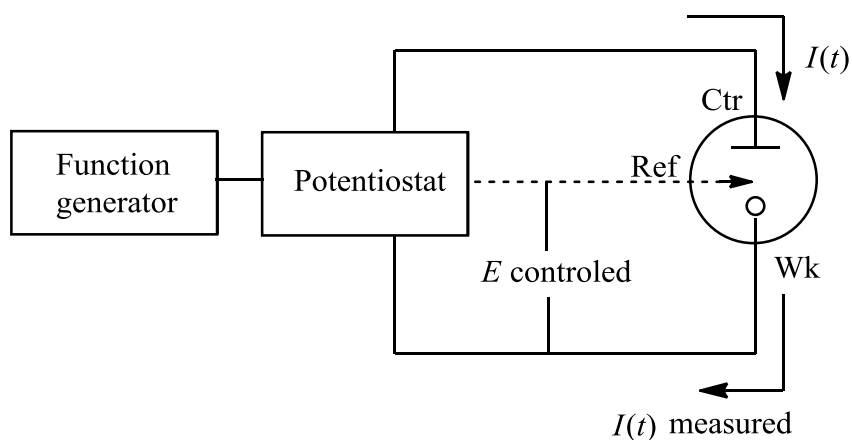


**Figure 2.17.** Experimental set up for controlled-potential experiments (adapted from Bard).<sup>98</sup>

The computer is used to generate the function, and to obtain and display the data. The electrochemical cell consists of a working electrode (Wk), a counter electrode (Ctr) and a reference electrode (Ref), and all three electrodes are immersed in an electrolyte. The potentiostat controls the potential,  $E$ , between the working electrode and the reference electrode, and measures the current,  $I$ , flowing between the working and counter electrodes. Photocurrent is generated by illuminating the working electrode by a light source.

In the study described in Chapter 4, photocurrent measurements were performed using a Schlumberger 1286 potentiostat with a Pt-coil counter electrode and a saturated Ag/AgCl

reference electrode. In the study described in Chapter 5 photocurrent measurements were obtained using an Eco Chemie Autolab PGSTAT10 potentiostat in a three-electrode glass cell. Ag/AgCl and a Pt wire were employed as reference electrode and as counter-electrode, respectively. Procedures of working electrode preparation and experimental conditions are described in detail in Chapters 4 and 5. Figure 2.18 illustrates the major components of the optical bench that was used for photoelectrochemical study described in Chapter 5.

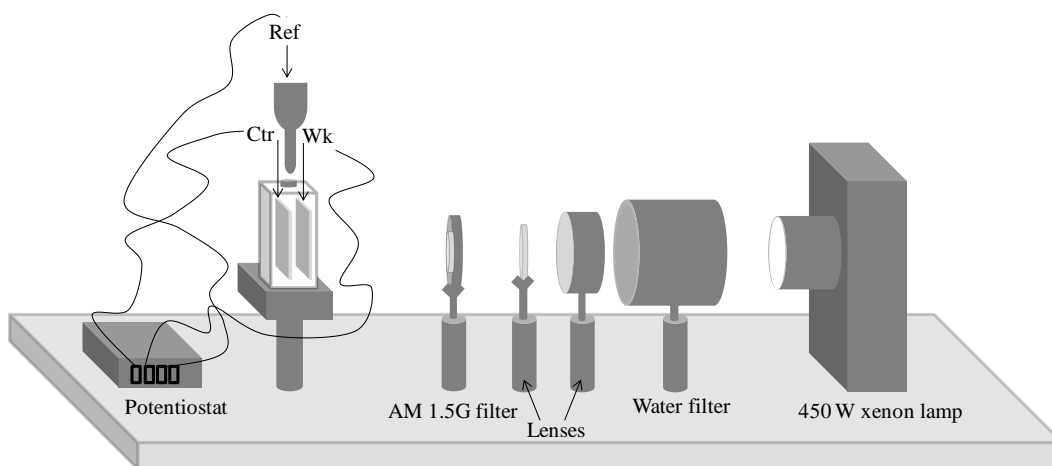


**Figure 2.18.** Schematic of the optical bench that was used for the photoelectrochemical measurements described in Chapter 5.

Incident photon to current efficiency (IPCE) or external quantum yield measurement is an important technique that can be used to verify the photocurrent measurement. In a typical IPCE measurement setup with an electrochemical cell (Figure 2.19), light is passed through a grating monochromator, the output signal is incident onto a beam splitter, and then focused onto the working electrode. Photocurrent signal is then measured by a potentiostat, and fed into a lock-in amplifier. The reflected portion of the signal by the beam splitter is detected by a silicon photodiode. Photocurrent is measured as a function of wavelength of the light while recording the

incident power of the light simultaneously, and signals from both the lock-in amplifier and photodiode are fed to a computer to produce IPCE curve.

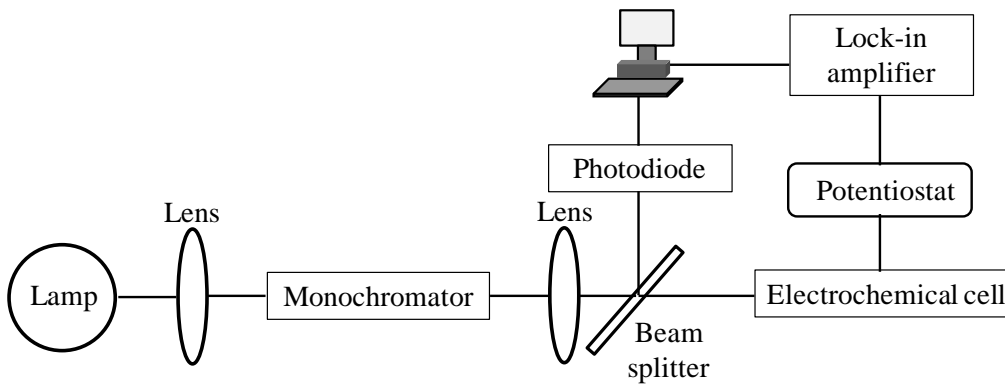


**Figure 2.19.** Schematic diagram of an IPCE experimental setup with an electrochemical cell (adapted from Krol).<sup>99</sup>

In the dissertation research, external quantum efficiency measurements were obtained with an Oriel 150 W Xe arc lamp (Newport) and a quarter-turn single-grating monochromator (Newport). Instrumentation and experimental conditions for IPCE measurements are described in detail in Chapter 4.

## CHAPTER 3

### AGGREGATION KINETICS OF METAL CHALCOGENIDE NANOCRYSTALS: GENERATION OF TRANSPARENT CdSe/ZnS CORE/SHELL GELS

#### 3.1 Introduction

The assembly of nanocrystals (NCs) into functional materials remains a key hurdle in the development of NC-based devices. As described in Chapter 1 (Section 1.5), sol–gel methods provide a tried and true approach for linking NCs into three-dimensional architectures (i.e., gels, xerogels, and aerogels) while preserving the properties of individual NCs.<sup>47,74</sup> Among chalcogenide gel materials, CdSe/ZnS core/shell gel materials<sup>75</sup> retain the NC band-gap tunability, which arises due to the dominance of quantum size effects in the electronic structure of CdSe NCs, and the intense NC band-edge luminescence, due to the suppression of nonradiative recombination pathways by overcoating the CdSe NC core with the ZnS shell. Moreover, removal of surface ligands and formation of a network of interconnected NCs during the gelation process are expected to provide better electronic communication between NCs. However, the lack of transparency of the sol–gel CdSe/ZnS materials produced to date remains a barrier to their use in optoelectronic applications, such as in light-emitting diodes (LEDs).

Gacoin and co-workers have extensively studied the sol–gel transition of CdS NCs and showed the possibility of formation of transparent CdS gel materials when the sizes of the fractal clusters in the gel are below the wavelength of visible light.<sup>50</sup> Furthermore, they demonstrated that the structure of the CdS gel materials depends on the nature and concentration of the oxidant. Therefore, it can be assumed that controlling the ligand and surface oxidation, and thus the aggregation and gelation kinetics, is key to achieving transparency in CdSe/ZnS gel materials. This chapter describes the details of a kinetic study of aggregation and gelation of

CdSe/ZnS NCs performed with the aim of synthesizing transparent gel materials. In this study, the kinetics of the sol–gel process for CdSe/ZnS NCs were evaluated by means of time-resolved dynamic light scattering (TRDLS) and small-angle X-ray scattering (SAXS) as a function of oxidant concentration, NC concentration, and NC size. On the basis of the TRDLS and SAXS analysis, the kinetics of aggregation and gelation of CdSe/ZnS NCs were correlated to the structural properties of the resulting gel materials and the degree of transparency. The contents of this chapter have been published as “Aggregation Kinetics of Metal Chalcogenide Nanocrystals: Generation of Transparent CdSe/ZnS Core /Shell Gels” (Korala, L.; Brock, S. L. *The Journal of Physical Chemistry C* **2012**, *116* (32), 17110-17117).

### **3.2 Experimental Section**

All the chemicals used in the syntheses described in this chapter are listed in Chapter 2 (Section 2.1). Transmission electron microscopy (TEM), UV–vis spectroscopy and powder X-ray diffraction (PXRD) were utilized for characterization of materials, and time-resolved dynamic light scattering (TRDLS) and small-angle X-ray scattering studies were performed as described in Chapter 2.

#### **3.2.1 Synthesis of CdSe/ZnS Core/shell NCs**

Highly luminescent CdSe/ZnS NCs were synthesized according to literature methods with slight modifications.<sup>100,101,32</sup> In a typical synthesis of green-emitting NCs, a mixture of 0.0127 g (0.1 mmol) of cadmium oxide, 0.04 g (0.14 mmol) of 1-tetradecylphosphonic acid (TDPA), and 2.0 g (5.17 mmol) of trioctylphosphine oxide (TOPO) were heated to 330 °C under argon flow to generate a homogeneous colorless solution. The temperature of the solution was reduced to 150 °C, and a solution of selenium containing 0.01 g (0.13 mmol) of selenium powder in 2.4 mL of trioctylphosphine (TOP) was injected. The temperature of the mixture was then

increased up to 250 °C at a rate of 10 °C per 10 min and aged for 4 h. In a typical synthesis of orange-emitting NCs, 0.15 g (0.53 mmol) of stearic acid was used instead of TDPA, the selenium solution was injected at 320 °C, and NCs were grown for 2 h at 300 °C. After aging the green and orange NC solutions, a small aliquot was taken for their characterization.

In order to make the ZnS shell, a mixture of 0.15 mL of 1 M diethylzinc in hexane, 0.03 mL of bis(trimethylsilyl) sulfide (0.14 mmol), and 2 mL of TOP was slowly injected over a period of 15 min (the total molar ratio of the injection solution was CdSe:ZnS 1:1.4, based on the number of moles used in the synthesis) using a syringe pump at 180 °C and followed by annealing at 75 °C overnight. As-prepared CdSe/ZnS NCs were purified by two cycles of dispersion in toluene and precipitation with methanol.

### **3.2.2 11-mercaptoundecanoic Acid (MUA) Exchange**

0.1 g (0.43 mmol) of MUA was dissolved in 10 mL of methanol, and the pH increased up to ~10 using tetramethylammonium hydroxide pentahydrate (TMAH). The MUA solution was added to the purified CdSe/ZnS NCs and shaken vigorously to achieve complete ligand exchange (Cd:MUA molar ratio of 1:4, based on original moles of Cd employed in the synthesis). The resulting MUA capped NCs were washed with ethyl acetate two times and then dispersed in methanol to make the NC sol.

## **3.3 Results and discussion**

Highly luminescent green- and orange-emitting CdSe/ZnS NCs were synthesized according to literature methods with slight modifications.<sup>100,101,32</sup> As-prepared CdSe/ZnS NCs were purified by two cycles of dispersion in toluene and precipitation with methanol and then exchanged with MUA. After removing excess MUA ligands, NCs were dispersed in methanol to make the sol. Figure 3.1 shows a high-resolution transmission electron microscope (HRTEM)

image of the as-synthesized green- and orange-emitting CdSe core NCs along with UV–vis and photoluminescence (PL) spectra of MUA-capped core/shell NCs. Core sizes (determined by HRTEM measurements) and optical properties of CdSe/ZnS core/shell NCs are listed in Table 3.1.

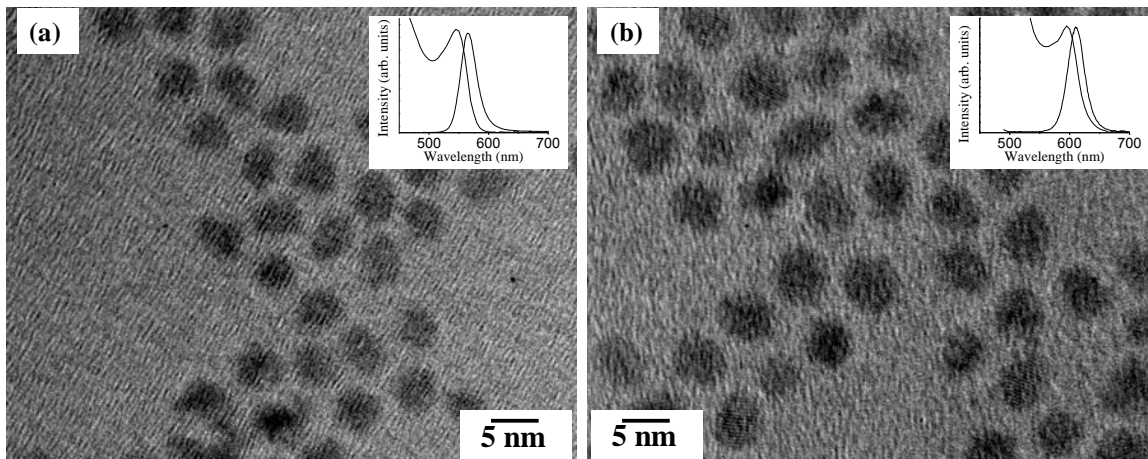


**Figure 3.1.** HRTEM images of (a) green- and (b) orange-emitting CdSe core NCs. The insets show absorption and emission spectra of MUA-capped core/shell NCs.

As expected, orange-emitting NCs have larger cores than the green-emitting NCs, and this is also reflected in the lower energy of absorption onset and band-edge emission maxima, consistent with less quantum confinement in the orange-emitting NCs. The full width at half-maximum (fwhm) values of the band-edge emission peaks of CdSe/ZnS core/shell in the PL spectra are between 31 and 34 nm, suggesting the presence of fairly monodisperse NCs. Gelation is achieved by oxidative ligand removal and formation of oxidized chalcogenide linkages between NCs.<sup>56</sup> Importantly, tetranitromethane is a non-oxygen-transferring oxidant and does not actively participate in bonding; NC–NC bonding occurs via purely inorganic chalcogenide linkages ( $S_n$ )<sup>2-</sup>.<sup>56</sup>

**Table 3.1.** Core size and optical properties of CdSe/ZnS core/shell NCs.

	Core size (nm)	Absorption onset (eV)	Band edge emission maxima (eV)	FWHM (nm)
Green-emitting NCs	$4.6 \pm 0.3$	2.17	2.19	31.3
Orange-emitting NCs	$5.3 \pm 0.4$	2.00	2.03	33.5

### 3.3.1. Probing the Effect of Kinetics of the Aggregation and Gelation on Gel Transparency by Time-Resolved Dynamic Light Scattering (TRDLS)

Aggregation kinetics can be considered in the context of two limiting regimes. Fast, diffusion-limited colloidal aggregation (DLCA), in which growth of the average cluster size has a power law behavior, and slow, reaction-limited colloidal aggregation (RLCA), in which exponential growth of the average cluster size occurs.<sup>102,103,104</sup> In the DLCA regime, power law behavior of the growth in the average radius of gyration  $\bar{R}_g$  of the aggregates can be shown by solution of the Smoluchowski equation<sup>105</sup>

$$\bar{R}_g(t) = \bar{R}_g(0) [1 + \alpha t/\tau]^{z/D_f} \quad (3.1)$$

In the RLCA regime, exponential scaling of  $\bar{R}_g$  is expected with a dependence represented by

$$\bar{R}_g(t) = \bar{R}_g(0) \exp(\alpha t/\tau) \quad (3.2)$$

In these equations  $z$  is the dynamic exponent,  $D_f$  is the fractal dimension,  $\alpha$  is the sticking probability and  $\tau$  is the reciprocal Smoluchowski rate

$$\tau = \frac{3\eta}{4k_B T N_o} \quad (3.3)$$

where  $\eta$  is the viscosity of the solvent,  $k_B$  is the Boltzmann constant,  $T$  is the absolute temperature and  $N_0$  is the primary particle concentration. In the DLCA regime, there are no repulsive forces between colloidal particles, and therefore every collision results in sticking, and aggregation kinetics depend solely on diffusion. In the RLCA regime, aggregation kinetics depend on the sticking probability of colloidal particles upon collision, due to the presence of inter-particle repulsive forces.

TRDLS is a powerful tool to study the kinetics of colloidal aggregation and gelation. We monitored the sol–gel transition of CdSe/ZnS NCs by TRDLS, and Z-average hydrodynamic radii,  $\bar{R}_h$ , of the aggregates were obtained as a function of time. Because  $\bar{R}_h$  is proportional to  $\bar{R}_g$  when  $q\bar{R}_h$  values are not equal to unity, we employed  $\bar{R}_h$  to study the kinetics of aggregation of CdSe/ZnS NCs.<sup>106,107</sup> To determine the effect of oxidant concentration on the kinetics of aggregation and gelation at room temperature, sols of CdSe/ZnS NCs with the same NC concentration ( $3.86 \times 10^{-7}$  M) and of two sizes (green and orange emitting) were used. NC concentration was determined by UV–vis spectroscopic measurements using size-dependent extinction coefficients published by Yu et al.<sup>108</sup>

Additionally, in order to explore the concentration effect, DLS measurements were done for green-emitting NC sols at a 10-fold increase in concentration. In all TRDLS measurements, sol volumes were constant (3 mL) and the sol was pipetted into a disposable cuvette. After adding varying amounts of 3% TNM (oxidant), the disposable cuvette was vigorously shaken, and immediately placed in the DLS instrument.

Figure 3.2a shows the time evolution of  $\bar{R}_h$  as a function of oxidant concentration in the aggregation of green- and orange-emitting NCs (N.B. the aggregation time period was selected over ranges where  $q\bar{R}_h$  is not equal to unity). Aggregation is initiated by the removal of thiolate

ligands by oxidation, consequently reducing the energy barrier for aggregation. Thus, increasing the oxidant concentration increases the aggregation rate due to the rapid removal of thiolate ligands from the NC surface, thus reducing the repulsive forces and increasing the sticking probability.

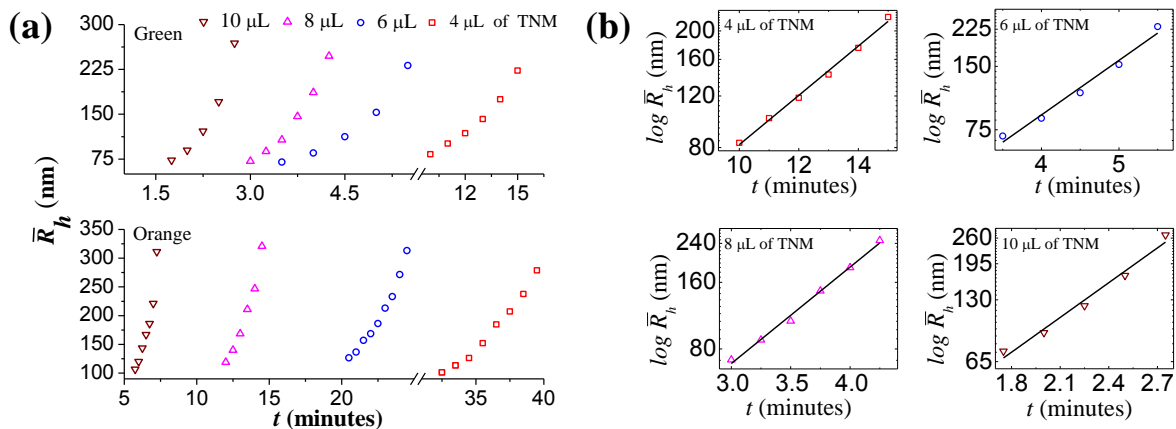


**Figure 3.2.** (a) Time evolution, as a function of the amount of TNM, of  $\bar{R}_h$  for green- and orange-emitting CdSe/ZnS NCs; and (b)  $\log \bar{R}_h$  vs time for green-emitting CdSe/ZnS NCs.

For green-emitting NCs treated with 4-10  $\mu\text{L}$  of TNM, aggregation follows RLCA kinetics as indicated in Figure 3.2b by the linear behavior on the semi logarithmic scale. Attempts to use the DLCA kinetic models resulted in poorer fits in each case. All the green-emitting wet gels are transparent (Figure 3.3a), although there is a decrease in transparency with the increase of oxidant, which is quantified by optical transmittance as shown in Figure 3.3b.

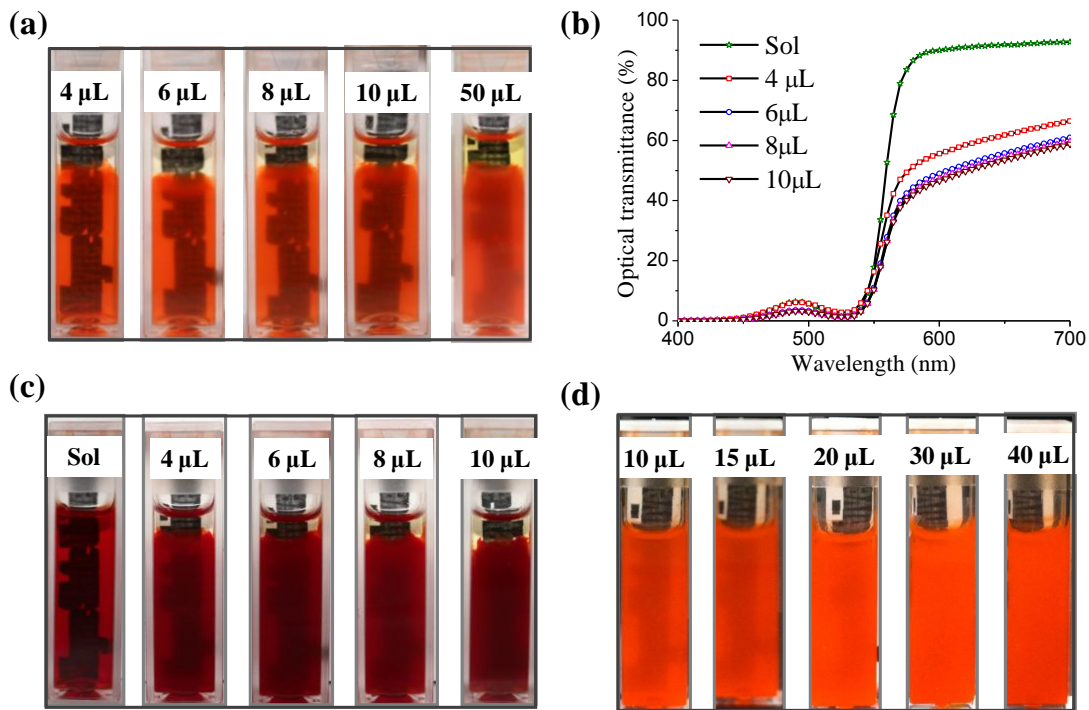


**Figure 3.3.** (a) Photographs, and (b) transmittance of green-emitting wet gels formed from different TNM concentrations; (c) Photographs of orange-emitting wet gels formed from different TNM concentrations; (d) Photographs of green-emitting wet gels (10-fold increase in concentration) formed by different TNM concentrations. Note: 40 μL of TNM in (d) corresponds to the same NC:TNM ratio as 4 uL in Figure 3.3a and c.

50 μL of TNM (Figure 3.3a) is poorly transparent, perhaps due to deviation of aggregation kinetics from the RLCA model. However, DLS failed to collect enough data to probe the kinetics due to the very fast aggregation and gelation (within a few seconds) that occurs at this high concentration of oxidant. Likewise, a 10-fold increase of NC concentration caused rapid aggregation even at the lowest ratio of oxidant to NC concentration used in the above study (4 μL TNM in the prior study corresponds to 40 μL TNM for a 10-fold NC concentration), and this may be due to a significant increase of the collision frequency in the

concentrated sols.<sup>109</sup> The decrease of the TNM amount (from 40 to 10  $\mu\text{L}$  TNM) drastically slows down the aggregation and gelation from a few seconds to several days for the high concentration of NCs. This may be due to the very low sticking probability, because of the large repulsive energy barrier for aggregation that arises from the surface ligands, which are being removed at much slower rates at low TNM concentrations. Furthermore, no correlation was observed between the aggregation kinetics of NCs and theoretical kinetic models (RLCA or DLCA) at this high NC concentration from TRDLS data (Figure 3.4) and all of the resultant gels are opaque (Figure 3.3d). These observations indicate that the control of aggregation kinetics of green-emitting CdSe/ZnS NCs can be utilized to alter the macroscopic properties of the resulting gels when the concentration of NCs is rather low (ca  $4 \times 10^{-7}$  M). At low NC and oxidant concentrations, aggregation follows RLCA kinetics and leads to formation of transparent gel structures.

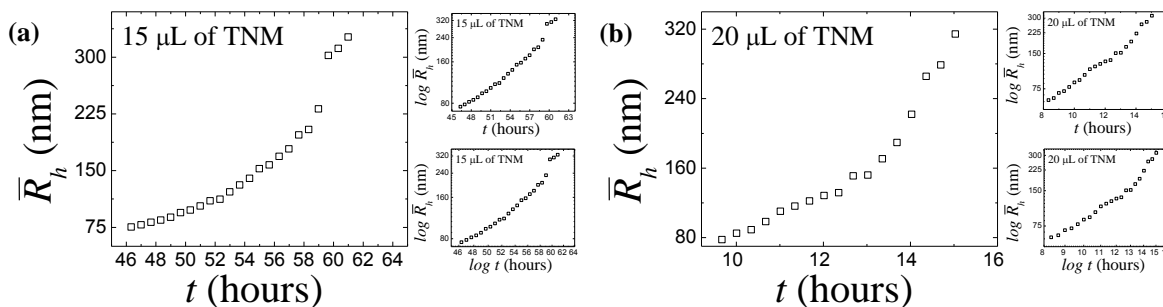


**Figure 3.4.** Time evolution of  $\bar{R}_h$  for green-emitting concentrated CdSe/ZnS sols oxidized by (a) 15  $\mu\text{L}$  and (b) 20  $\mu\text{L}$  of 3% TNM. Insets show  $\log \bar{R}_h$  vs time and  $\log \bar{R}_h$  vs  $\log$  time. The lack of linearity in the semi-log and log-log plots suggests that neither the RLCA or DLCA mechanism, respectively, are good fits to the data.

Aggregation kinetics clearly depend on the overall NC size, as orange-emitting NCs showed slower aggregation kinetics compared to the green-emitting NCs for the same oxidant and NC concentrations. This may be due to the slower diffusion rate of larger NCs and the presence of a larger number of surface ligands on the NC surface compared to that of the green-emitting NCs for the same particle concentration. For orange emitting NCs, it is difficult to describe the aggregation kinetics using theoretical models since RLCA or DLCA kinetics couldn't be distinguished by means of aggregation plots (Figure 3.5). The resulting wet gels have poor transparency and opacity increases with the amount of oxidizing agent used to form the wet gels (Figure 3.3c).

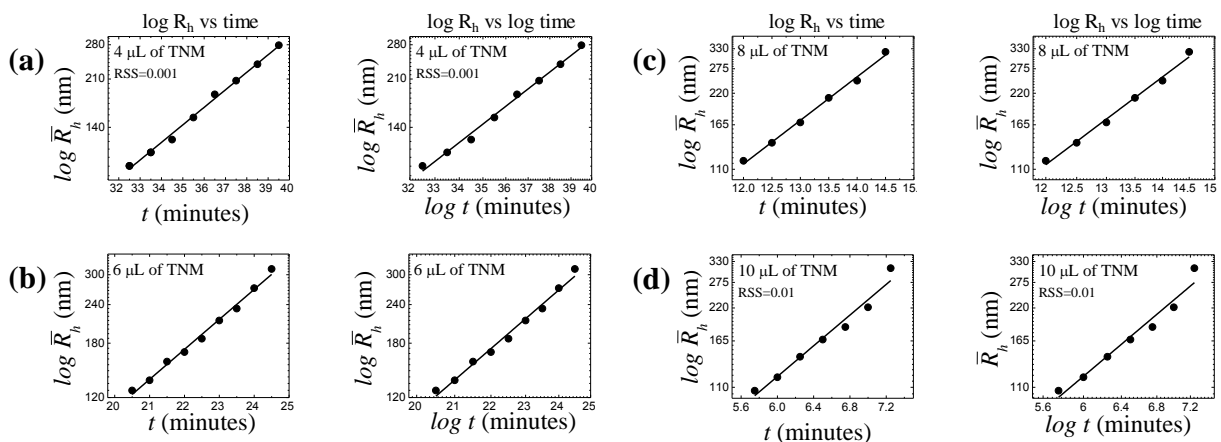


**Figure 3.5.**  $\log \bar{R}_h$  vs time and  $\log \bar{R}_h$  vs  $\log$  time for orange-emitting CdSe/ZnS sols oxidized by (a) 4  $\mu\text{L}$ , (b) 6  $\mu\text{L}$ , (c) 8  $\mu\text{L}$ , and (d) 10  $\mu\text{L}$  of 3% TNM.. The mechanism cannot be distinguished (RLCA/DLCA) because equivalent fits are obtained for each model.

TRDLS has also been used to study the sol–gel transition of various systems.<sup>110,111</sup> We extended this study to the metal chalcogenide system in order to understand the effect of

aggregation and gelation kinetics on the macroscopic properties of the resultant gels. The sol–gel transition can be described as a divergence-of-connectivity correlation.<sup>112</sup> At the gelation point, aggregates resulting from nonequilibrium cluster-cluster aggregation processes overlap and form a network to fill the total volume of the solution.<sup>113</sup> Hence, the approximate largest aggregate size near the gel point resulting from the cluster growth can be employed to explain the macroscopic properties (i.e. transparency) of the gel structure resulting from different kinetics.<sup>114</sup>

Martin and coworkers probed the silica sol–gel transition by TRDLS. According to their observations, the intensity correlation function  $g^2(\tau)$  shows a stretch exponential decay during the pre-gelation period (Equation 3.4) and a transition from a stretch exponential decay to a power-law decay at the gel point (Equation 3.5)<sup>110,113</sup>

$$g^2(\tau) - 1 \approx \sigma_1^2 \left\{ A \exp(-Dq^2\tau) + (1 - A) \exp \left[ - \left( \frac{\tau}{\tau_c} \right)^\beta \right] \right\}^2 \quad (3.4)$$

$$g^2(\tau) - 1 \approx \sigma_1^2 \left\{ A \exp(-Dq^2\tau) + (1 - A) \left[ 1 + \left( \frac{\tau}{\tau^*} \right)^{\frac{n-1}{2}} \right] \right\}^2 \quad (3.5)$$

where  $\sigma_1^2$  is the initial amplitude of the intensity correlation function,  $A$  is the fraction of the translational diffusion mode,  $D$  is the translational diffusion coefficient,  $\tau_c$  is the characteristic time for the stretch exponential mode ( $0 \leq A \leq 1$ ),  $\beta$  is the stretch exponent ( $0 < \beta < 1$ ),  $\tau^*$  is the time at which power-law behavior begins and  $n$  is the fractal dimension of the scattered photons ( $0 < n < 1$ ). For the sol state, the first exponential function relates to the translational diffusion of the clusters or aggregates, which follows a stretched exponential decay; whereas at the gel point, the initial exponential function follows a power-law decay.

Figure 3.6 shows the time evolution of intensity correlation functions,  $g^2(\tau)$ , for the green- and orange-emitting CdSe/ZnS NC sols oxidized by 4 $\mu$ L of TNM. Solid and dashed

curves represent the fitted curves using Equation 3.4 and 3.5, respectively. In both cases, the decay time,  $\tau$ , for the intensity correlation function,  $g^2(\tau)$ , increases with time, indicative of an aggregation process. Equation 3.4 was used to successfully fit the initial intensity correlation functions that show a stretch exponential decay of  $g^2(\tau)$ , suggesting that the samples remain in the sol state. At the gel point, the power law behavior of the intensity correlation function  $g^2(\tau)$  is evident by the successful fitting to the experimental curve using Equation 3.5, as indicated by the dashed lines in Figure 3.6. Near the gel point  $t_{gel}$ , the approximate largest aggregate size of the resulting gel can be determined from NNLS analysis, and these data are summarized in Table 3.2. For the green-emitting CdSe/ZnS gels, the approximate maximum aggregate sizes near the gel point are below the wavelength of visible light at low oxidant concentrations, explaining the transparency. The maximum aggregate size near the gel point increases with the oxidant concentration, and it can be assumed that rapid aggregation at relatively high oxidant concentrations (e.g. 50  $\mu\text{L}$  of TNM) results in comparatively larger aggregates,<sup>109</sup> consequently increasing the scattering of light and resulting in opaque gels. For the orange-emitting gels, the comparatively larger aggregates near the gel point significantly increase the scattering of visible light photons, making them less transparent than green-emitting gels for the same amount of TNM added. The aggregation of colloidal particles depends on both the collision frequency and sticking probability. The slower aggregation inherent in the larger particles, due to the slower diffusion and larger number of surface ligands that need to be removed from the surface, delay the gel point, but the fact that the aggregates present near the gelation point are larger than those for green-emitting sols suggests a higher sticking probability is occurring for the de-protected orange-emitting NCs.

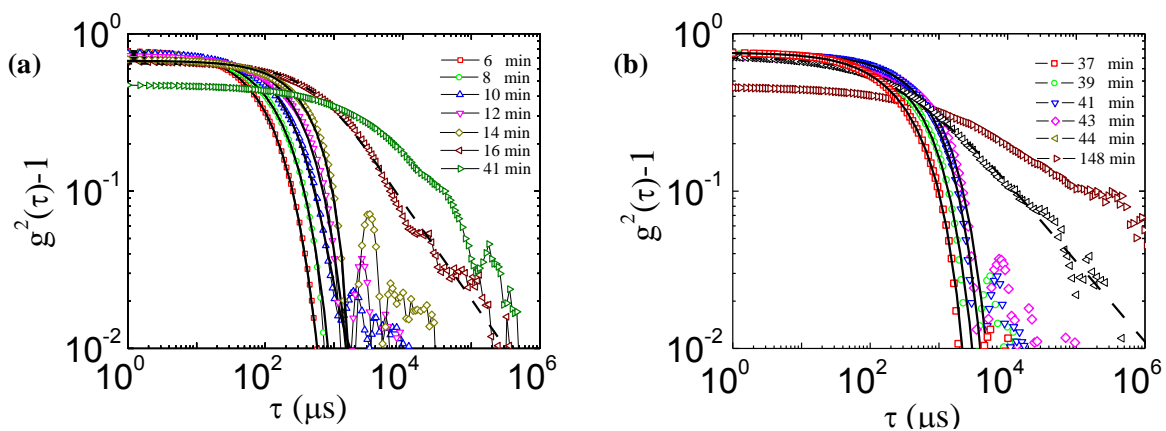


**Figure 3.6.** Intensity correlation functions,  $g^2(\tau) - 1$  of the (a) green-, and (b) orange-emitting CdSe/ZnS NC sols oxidized by 4  $\mu\text{L}$  of TNM as a function of time.

**Table 3.2.** Gel point,  $t_{gel}$ , and average cluster size near the gel point for green- and orange-emitting gels formed from different amounts of TNM.

Amount of TNM ( $\mu\text{L}$ )		4	6	8	10
Green-emitting gels	$t_{gel}$ (min)	16	6	4.5	3
	Average cluster size (nm)	$230 \pm 36.83$	$320 \pm 44.73$	$390 \pm 52.05$	$470 \pm 51.32$
Orange-emitting gels	$t_{gel}$ (min)	43	25	15	7.5
	Average cluster size (nm)	$480 \pm 46.65$	$510 \pm 50.51$	$540 \pm 52.47$	$670 \pm 69.86$

### 3.3.2. Probing the Effect of the Kinetics of Aggregation and Gelation on Structural Characteristics of the Resultant Gels by Small-angle X-ray Scattering (SAXS)

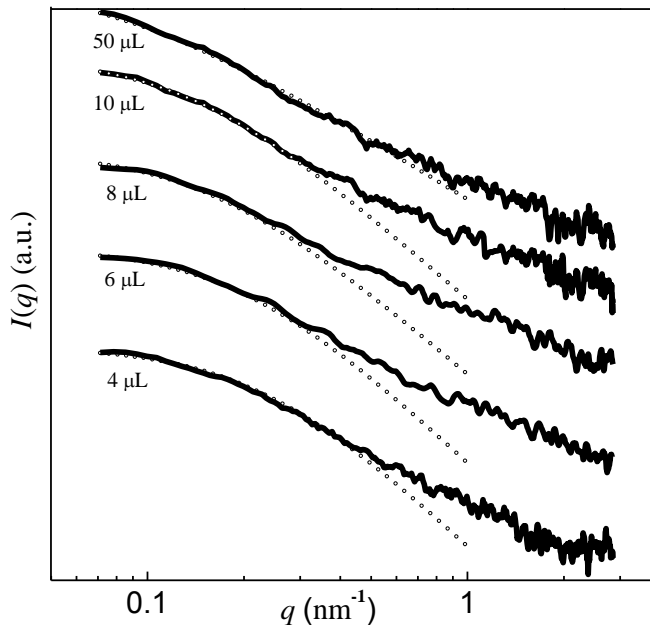
As pointed out earlier, aggregation of colloidal particles results in disordered fractal clusters that are connected to form the wet gel structure at the gel point. The SAXS technique can be employed to study the structure of the wet gels and this allows correlation of the structural characteristics of the wet gels to the aggregation process, and ultimately to the macroscopic properties of the gels. Furthermore, this allows the structural characteristics of green-emitting gels that result from relatively high amounts of oxidizing agent, where the kinetics are too fast to resolve by DLS, to be probed. For SAXS measurements, sol volumes (3 mL) were pipetted into disposable cuvettes, and varying amounts of 3% TNM were introduced, as was the case for TRDLS; then a portion was transferred to 2.0 mm boron-rich capillary tubes and allowed to gel.

Figure 3.7 shows scattering intensity,  $I(q)$ , of wet gels formed by introduction of different concentrations of TNM to green-emitting sols, as a function of the scattering vector,  $q = (4\pi/\lambda) \sin (\theta/2)$ . In a typical scattering curve of a mass fractal aggregate, the power law behavior of  $I(q)$  within the mass fractal region occurs in the  $q$  range  $1/\xi \gg q \gg 1/a$ , where  $\xi$  is the correlation length and  $a$  is the average particle size.  $I(q)$  deviates from power law behavior for  $q$  above  $1/\xi$ , which is called Guinier region.<sup>115</sup> The  $I(q)$  of Guinier and fractal regions, and the crossover between the Guinier and fractal regions, can be fit by

$$I(q) = A \frac{\Gamma(D + 1)}{(1 + q^2 \xi^2)^{(D-1)/2}} \frac{\sin[(D - 1) \arctan(q\xi)]}{(D - 1)q\xi} \quad (3.6)$$

where  $A$  is a constant for a given  $D$  and  $\xi$ , and  $\Gamma$  is the gamma function.<sup>116</sup>

Fitting the above equation for the low and medium  $q$  regions of the experimental curves, the fractal dimension  $D$  and correlation length  $\xi$  of the wet gels formed by different amounts of TNM can be obtained (Table 3.3).



**Figure 3.7.** SAXS spectra of green-emitting wet gels formed from different amounts of TNM. Lines composed of open circles represent the fitting of Equation 12 to the experimental curves.

**Table 3.3.** Fractal dimension,  $D$ , correlation length,  $\xi$ , and relative cluster mass,  $m$ , values of the green-emitting gels formed from different amounts of TNM.

Amount of TNM ( $\mu\text{L}$ )	4	6	8	10	50
$D$	1.96	1.95	1.84	1.83	1.30
$\xi$ (nm)	4.5	5.1	6.1	7.5	14.8
$m \propto \xi^D$	19	24	28	40	33

Fractal dimension values estimated from the fitting process are in the range between  $\sim 1.8$  and  $\sim 2.0$ , except for the gel formed by 50  $\mu\text{L}$  of TNM. According to Gacoin et al., transparent CdS gels resulting from the RLCA mechanism have a fractal dimension of 1.9.<sup>50</sup> From our

observations, the fractal dimension decreases with the increase of oxidant concentration and there is a significant decrease at 50  $\mu\text{L}$  of TNM. The change in amounts of TNM also results in change in cluster mass, which is related to the correlation length and fractal dimension, according to Equation 3.7.<sup>115, 117</sup>

$$m \propto \xi^D \quad (3.7)$$

As confirmed by TRDLS, fast removal of ligands from the NC surface with the increase of oxidant concentration increases the probability of NC sticking and leads to larger aggregates before they form the gel network, and this can be further confirmed by the increase of the correlation length with the increase of oxidant concentration, as it is associated with the average cluster size.<sup>50,118</sup> Furthermore, the increase of sticking probability prevents the small clusters from permeating the large clusters, and so they are rapidly attached at the edge of the large clusters, resulting in more open and less dense aggregates and a lower fractal dimensionality of the final gel structure (Table 3.3).<sup>102</sup> A dramatic change is observed between 10-50  $\mu\text{L}$ , consistent with a shift toward DLCA. Relative cluster-mass values are consistent with this phenomena, since the relative cluster mass,  $m$ , decreases between 10 and 50  $\mu\text{L}$  of TNM, although there is a significant increase of the cluster size according to the correlation length values (Table 3.3). TEM images of the gel structures formed by 8 and 50  $\mu\text{L}$  of TNM reveal this difference. As shown in Figure 3.8a and b, the resulting gel structure is more dense at a low concentration of oxidant, where aggregation follows RLCA kinetics. At high concentration of oxidant, faster kinetics resulted in a more open and less dense gel structure as indicated in Figure 3.8c and d. Because these are disordered fractal materials, no symmetry is apparent in the TEM images.

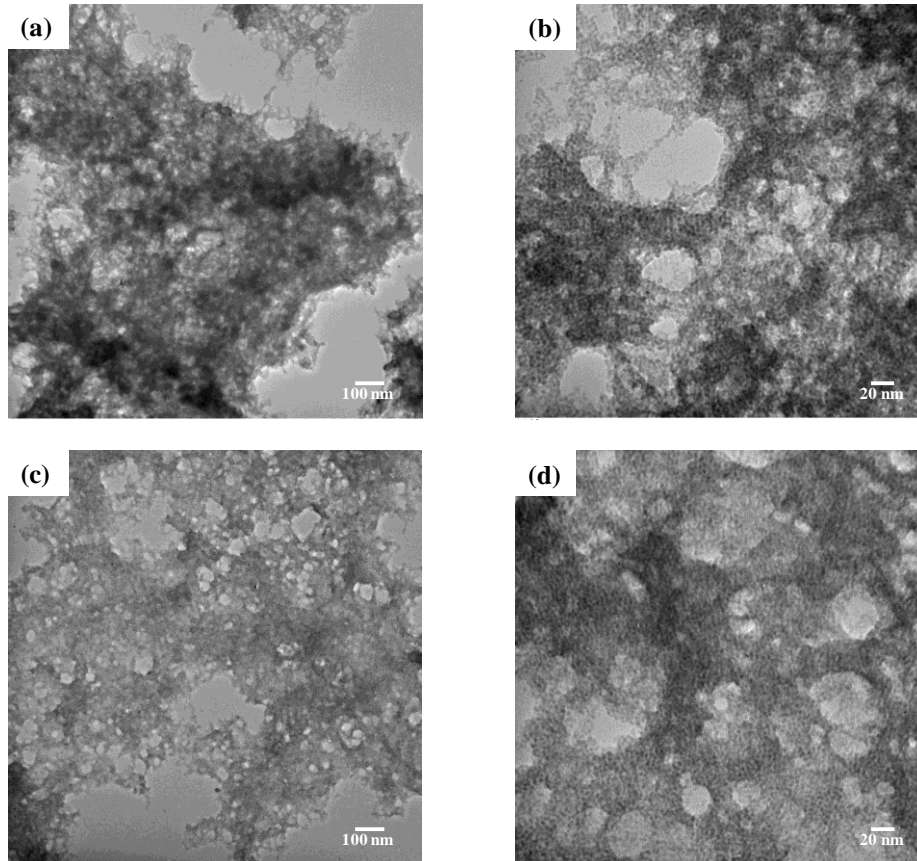


**Figure 3.8.** TEM images of gel clusters formed by (a), (b) 8  $\mu\text{L}$  , and (c), (d) 50  $\mu\text{L}$  of TNM.

The trend towards DLCA (i.e., increased sticking probability) observed for the larger, orange-emitting particles in the TRDLS is also reflected in the SAXS data. Orange-emitting gels formed from addition of 4  $\mu\text{L}$  of TNM exhibit lower fractal dimension ( $D = 1.76$ ) and higher correlation length values ( $\xi = 8.49$ , Figure 3.9) than the green-emitting gels formed under the same conditions.

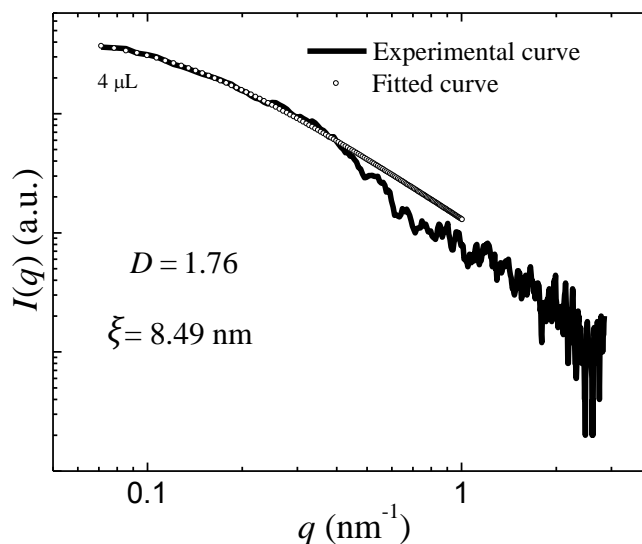


**Figure 3.9.** SAXS spectrum of an orange-emitting wet gel formed from 4  $\mu\text{L}$  of TNM.

### 3.4 Conclusions

The mechanism and kinetics of aggregation of green- and orange-emitting CdSe/ZnS core/shell NCs, initiated by removal of surface thiolate ligands using TNM as an oxidant, was studied by means of TRDLS and the characteristics of the resultant gels were probed by optical absorption, TEM and SAXS. Analysis of the sol–gel transition process clearly indicates that the degree of transparency of the resultant gels depends on the structural characteristics of the gels, which are in turn governed by the kinetics of aggregation and gelation of NCs. For small, green-emitting NCs, aggregation follows RLCA kinetics at low concentrations of NCs and oxidant, and the resulting gel structures are transparent due to the formation of aggregates that, at the gel point, have sizes below the wavelength of visible light. As the particle concentration, size or oxidant concentration is increased, there is a shift away from RLCA kinetics and the resultant aggregates trapped at the gel point are larger, scattering visible light and increasing opacity. These trends correlate with the fractal dimensionality of the gel networks, in which decreasing dimensionality correlates with larger, lower density aggregates arising from increased sticking

coefficients (i.e., a shift towards a DLCA mechanism) and decreased transparency. The ability to control the transparency of chalcogenide gels enables their properties to be tuned in order to address application-specific needs in optoelectronics.

## CHAPTER 4

### FABRICATION OF CHALCOGENIDE SOL–GEL FILMS FOR APPLICATIONS IN OPTOELECTRONICS

#### 4.1 Introduction

Thin films of semiconductor nanocrystals (NCs) are promising materials for electronic and optoelectronic device applications including field-effect transistors (FETs),<sup>57,58</sup> photodetectors,<sup>59,60</sup> light emitting diodes (LEDs)<sup>61,62</sup> and solar cells.<sup>63,64</sup> The size- and shape-tunable optical and electronic properties of semiconductor NCs, along with their solution processability, permit great flexibility in device design, enabling the use of low cost fabrication methods such as solution coating<sup>119</sup> or printing.<sup>120</sup> As discussed in Chapter 1 (Section 1.6), the charge transport properties of NC thin films play a major role in device performance and depend on the extent of electronic coupling between neighboring NCs, where charge transport occurs via tunneling.<sup>65</sup> Unfortunately, bulky organic ligands used in the synthesis of NCs reduce the interparticle coupling, and consequently have a destructive effect on the charge transport properties of NC films.

Reduction of the inter-NC spacing is one of the main strategies being investigated to improve the electronic communication between NCs in thin films. This can be done by removing the bulky organic surfactants by thermal annealing<sup>121,122</sup> or by exchanging them with smaller ligands, either in the solution phase before depositing the NCs as thin films (nitrosonium tetrafluoroborate,<sup>123</sup> molecular metal chalcogenides,<sup>124,125,126</sup> chalcogenide anions,<sup>127,128</sup> thiocyanate<sup>72</sup> or in the solid phase after deposition (hydrazine,<sup>10</sup> NaOH,<sup>129,130</sup> thiols,<sup>119,131,132,133</sup> amines,<sup>121,57</sup> short-chain carboxylic acids.<sup>134</sup> Alternatively, as discussed in Chapter 1 (Section 1.5), sol–gel methods can be used to assemble metal chalcogenide NCs into gels, xerogels, and

aerogels that have interconnected networks of NCs.<sup>47,49</sup> This is achieved by oxidative decomplexation of thiolate-capped NCs, exposing the particle and oxidizing surface chalcogenide species, resulting in interparticle linking via dichalcogenide bonding.<sup>56</sup>

In this dissertation research, kinetics of aggregation and gelation of 11-mercaptoundecanoic acid (MUA)-capped CdSe/ZnS core/shell NCs were probed by scattering techniques and it was shown that the cluster size at the gelation point has a major impact on the macroscopic properties (e.g. transparency) of the resulting gels (Chapter 3). For CdSe/ZnS NCs (average diameter 4.6 nm), transparent gel structures resulted at low NC concentration ( $4 \times 10^{-7}$  M) and oxidant concentration, where aggregation follows reaction limited colloidal aggregation (RLCA) kinetics. The present chapter describes the (1) exploitation of these conditions to create transparent micron-thick CdSe/ZnS xerogel films and charge transport studies performed using van der Paw method, and (2) a new strategy to fabricate high quality chalcogenide NC sol–gel thin films along with an evaluation of the potential of these films for optoelectronic applications by means of photoelectrochemical measurements. The work described in this chapter has been published in two articles as “Transparent conducting films of CdSe/ZnS core/shell quantum dot xerogels” and “Uniform Thin Films of CdSe and CdSe/ZnS Core/Shell Quantum Dots by Sol–Gel Assembly: Enabling Photoelectrochemical Characterization and Electronic Applications” (Korala, L.; Li, L.; Brock, S. L., *Chemical Communications* **2012**, 48 (68), 8523-8525 and Korala, L.; Wang, Z.; Liu, Y.; Maldonado, S.; Brock, S. L., *ACS Nano* **2013**, 7 (2), 1215-1223).

## 4.2 Experimental Section

All the chemicals used in the syntheses described in this chapter are listed in Chapter 2 (Section 2.1). Materials were characterized by performing X-ray diffraction (XRD), photoluminescence (PL) spectroscopy, FTIR spectroscopy, UV–vis spectroscopy, Atomic force

microscopy (AFM), field emission scanning electron microscopy (FESEM), transmission electron microscopy (TEM) and scanning transmission electron microscopy (STEM) as described in Chapter 2. To image the NCs before and after gelation by TEM and STEM, a thioglycolic acid-capped NC sol was drop casted onto a carbon-coated copper TEM grid and then dipped in a TNM solution (50  $\mu$ L of 3% TNM in 10 mL of acetone) for one minute and then submerged in fresh methanol solution for several minutes before allowing to air-dry.

#### **4.2.1 Synthesis of CdSe and CdSe/ZnS Core/shell NCs**

##### **4.2.1.1 NC Precursors for Xerogel Films**

In order to fabricate micron-thick xerogel films, CdSe/ZnS NCs were synthesized according to literature methods with slight modifications as described in Chapter 3 (Section 3.2.1).<sup>100,32</sup>

##### **4.2.1.2 NC Precursors for Sol–gel Thin Films**

For the fabrication of chalcogenide sol–gel thin films CdSe and CdSe/ZnS NCs were synthesized using s different literature procedure with modification.<sup>101,32</sup> In a typical synthesis, a mixture of 0.0514 g (0.4 mmol) cadmium oxide, 0.5 g (1.76 mmol) stearic acid and 3.7768 g (9.77 mmol) trioctylphosphine oxide was heated at 300 °C under argon flow and then a solution containing 0.0316 g (0.4 mmol) of selenium powder in 2.4 mL trioctylphosphine was injected after the solution became colorless. The NCs were grown at this temperature for two hours. ZnS shell formation and isolation of the NCs followed the procedure described in 3.1.1.

##### **4.2.1.2 MUA/thioglycolic Acid Exchange**

0.0223/0.3678g (0.1/1.6 mmol) of MUA or 0.11 mL (1.6 mmol) of thioglycolic acid was dissolved in 10 mL of methanol and the pH increased up to ~10 using TMAH. NCs were dispersed in MUA/thioglycolic acid solution (Cd:MUA/ thioglycolic acid molar ratio of 1: 4,

based on original moles of Cd employed in the synthesis) and centrifuged to remove the original organic ligands NCs were washed with ethyl acetate to remove excess MUA/ thioglycolic acid ligands and dispersed in methanol to make a NC sol.

#### **4.2.1.3 Deposition of Micron-thick CdSe/ZnS Xerogel Films by Sol–gel Methods**

Glass slides (Becton, Dickinson and Co.) were used as substrates for film deposition. Slides were cut to 1 cm by 1 cm and sonicated in acetone and ethanol, respectively, for 15 minutes. After rinsing with distilled water, the glass slides were dried under nitrogen gas blow. For the film deposition, glass slides were immersed in different volumes (ranging from 3 mL to 5 mL, NC concentration of  $4 \times 10^{-7}$  M ) of pre-oxidized MUA-capped CdSe/ZnS sols in compartmentalized Petri dishes (4 sections, 100mm (diameter)  $\times$  15mm (height), Fisher Scientific). 10  $\mu$ L of tetranitromethane (TNM) was then added to oxidize the MUA ligands, resulting in aggregation. After gelation, the substrates were dipped in acetone to remove the gelation by-products and dried under ambient conditions to make xerogel films.

#### **4.2.1.4 Deposition of CdSe and CdSe/ZnS Sol–Gel Thin Films**

Glass slides or silicon wafers were used as substrates for film deposition. Substrates were sonicated in acetone, ethanol, and water, respectively, for 15 min each. After rinsing with distilled water, substrates were dried under nitrogen gas blow. NC sols were spin coated (4000 rpm, 40 s) on glass or silicon substrates and dipped in tetranitromethane (TNM) solution (50  $\mu$ L of 3% TNM in 10 mL of acetone) for one minute and then dipped in fresh methanol solution for several minutes to remove the gelation byproducts (2 times) and finally dried under ambient conditions. For photocurrent measurements, NC sols were spin coated (4000 rpm, 40 s) on ITO-coated glass substrates (Delta Technologies,  $R_s = 5\text{--}15 \Omega$ ) and gelled following the above procedure. ITO substrates were cleaned following the same procedure as for the glass substrates.

Prior to spin coating, a portion of the ITO-coated glass substrate on one side was covered with tape to ensure a bare ITO region without NC film for electrode attachment. After spin coating, films were dried in ambient conditions and then annealed at 250 °C for 30 min under argon flow.

#### **4.2.1.5 Photoelectrochemical Measurements**

NC films fabricated on ITO-coated glass were used as working electrodes. The bare ITO region was mounted onto a coiled tinned copper wire using conductive silver paste (GC electronics) and sealed with Hysol 1C epoxy. The photoactive area was determined by optical image analysis. The electrodes were placed in a Teflon cell (with a glass window for light illumination) containing a 0.1 M polysulfide aqueous solution ( $\text{Na}_2\text{S} + \text{NaOH} + \text{S}$ ) as electrolyte. White light illumination was provided by a tungsten halogen lamp light source (ELH, Osram) with a quartz diffuser. The illumination intensity was set to  $100 \text{ mW/cm}^2$  using a thermopile (S302A, Thorlabs), and photocurrent measurements were performed at -0.57 V (solution redox potential) with respect to the Ag/AgCl reference electrode. No external bias was applied.

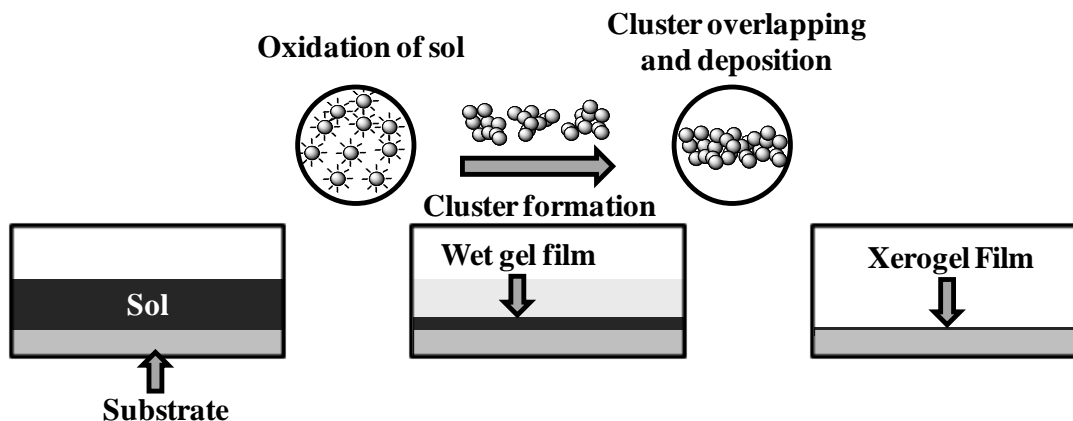
#### **4.2.1.6 Photon to Current Efficiency (IPCE) Measurement**

External quantum efficiency measurements were obtained with an Oriel 150 W Xe arc lamp (Newport) and a quarter-turn single-grating monochromator (Newport). Sample measurements were recorded with chopped illumination (20 Hz), and a quartz beam splitter was used to simultaneously record the light output intensity with a separate Si photodiode (Newport) to adjust for fluctuations in lamp intensity. Absolute photocurrents were measured by a digital PAR 273 potentiostat at -0.57 V with respect to the Ag/AgCl reference electrode, and the output current signal was connected to a Stanford Instruments SR830 lock-in amplifier. The output signals from the lock-in amplifier and the reference Si photodiode were fed into a computer controlled by custom-written LabVIEW software.

## 4.3 Results and discussion

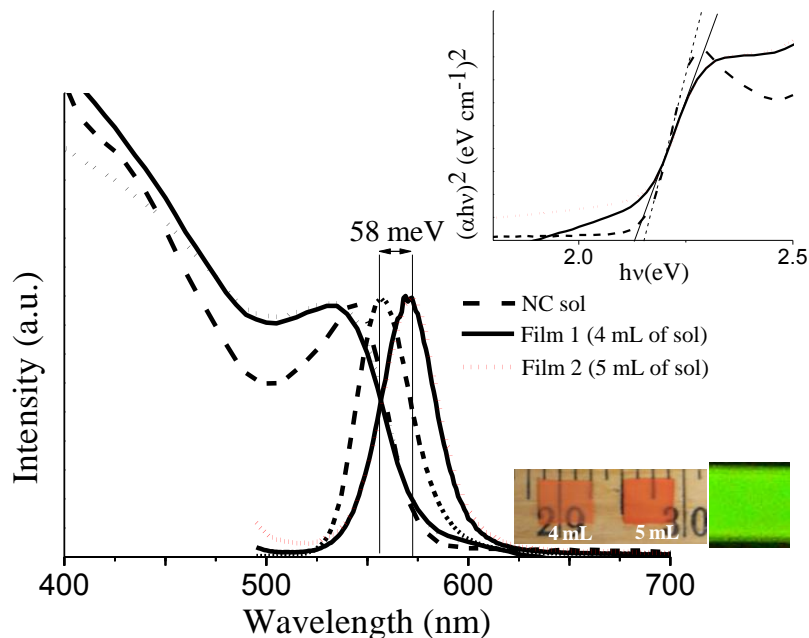
### 4.3.1 Transparent Micron-thick Conducting Films of CdSe/ZnS NC Xerogels

The conditions that lead to formation of transparent gel structures (Chapter 3) were exploited to create xerogel films. Green-emitting CdSe/ZnS NCs were synthesized according to literature methods with slight modifications and original trioctylphosphine oxide (TOPO) ligands were exchanged with MUA ligands.<sup>100,32</sup> The synthesis of transparent xerogel films of CdSe/ZnS NCs was achieved by immersing glass substrates horizontally in pre-oxidized sols of MUA-capped CdSe/ZnS NCs, gelling and drying under ambient conditions. The film thickness can be varied by adjusting the height of the volume fraction of sol on top of the substrate. Scheme 3.1 illustrates the formation and overlapping of clusters during the gelation process to construct the gel film. Oxidation of the precursor thiolate-capped CdSe/ZnS NCs, which are dispersed in methanol (sol), by tetranitromethane (TNM) removes the thiolate ligands from the NC surface and exposes the NC surface to the oxidizing environment. Solvation of surface  $\text{Zn}^{2+}$  ions, and then further oxidation of exposed  $\text{S}^{2-}$  ions by the oxidant, links the NCs together via sulfide bonding,<sup>56</sup> initiating the aggregation process. During the aggregation, clusters are formed and cluster sizes increase with time due to continuous collision and sticking of NCs. At the gel point, clusters overlap and fill the volume above the substrate, resulting in a wet gel film. Drying under ambient conditions causes pore collapse and further shrinking, principally from the top-down, while preserving the interconnected network of NCs within the xerogel film.



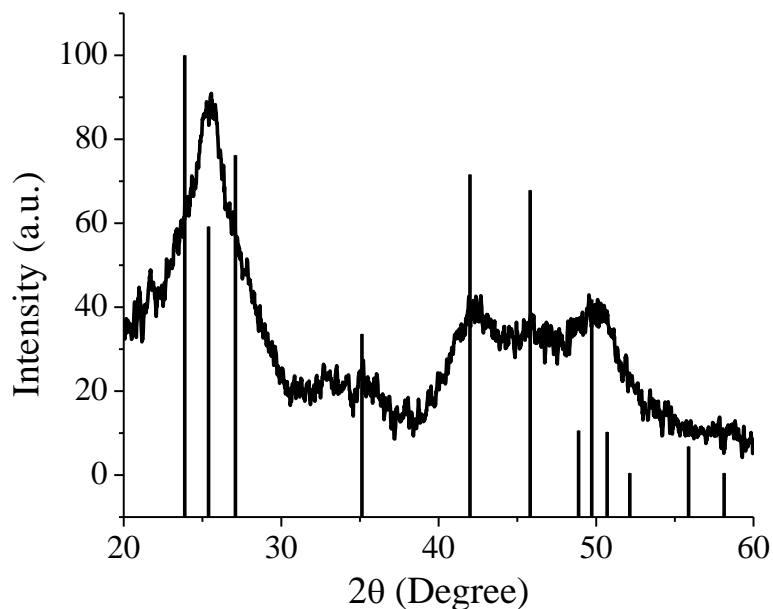
**Scheme 4.1.** Schematic illustration of the fabrication of a CdSe/ZnS xerogel film.

Figure 4.2 shows UV–vis and PL spectra of the sol, and the sol–gel films deposited from different volumes of sol. The deposited CdSe/ZnS xerogel films are quite transparent and highly luminescent when viewed under a UV lamp, as shown in the inset (bottom) of Figure 4.2. The wavelength of the first absorption peak of the xerogel films is blue shifted compared to that of the NC solution, but there is a slight red shift of the band gap value (20 meV, inset, Figure 4.2) which is extracted by plotting  $(ahv)^2$  vs.  $hv$  and extrapolating the linear part of the graph to the energy axis, as shown in the inset of Figure 4.2. The discrepancy can be attributed to the broadening of absorbance, smearing out the primary absorption peak. Moreover, the xerogel film shows a significant red shift (58 meV) in the PL maxima. These changes in absorption/emission properties are a good indication of the presence of an interconnected network of NCs within the xerogel film, where strong coupling of adjacent NCs results in efficient Förster resonant energy transfer.



**Figure 4.2.** UV–vis spectrum and PL spectrum of CdSe/ZnS NC sol and xerogel films deposited from 4 and 5 mL of sol (particle concentration, ca.  $4 \times 10^{-7}$  M). The inset (top) shows the plot of  $(\alpha hv)^2$  vs.  $hv$  for the absorption spectra and photographs (bottom) of deposited films under normal and UV light. There is a 58 meV shift in the PL peak upon going from a sol to a xerogel film.<sup>74,135</sup>

Structural and composition analysis of the films was done by performing X-ray diffraction (XRD) and energy dispersive spectroscopy (EDS). The XRD pattern of the xerogel film (Figure 4.3) reveals the hexagonal phase of CdSe, as is also seen in the precursor NCs. Semi-quantitative analysis of xerogel films by EDS reveals that Cd : Se : Zn : S ratios are 28.00 : 22.43 : 18.05 : 31.52. The excess chalcogen (sulfur) is attributed to residual MUA ligands on the NC surfaces comprising the xerogel film.



**Figure 4.3.** XRD pattern of a xerogel film deposited on a glass slide from 5 mL of sol. The line diagram corresponds to bulk CdSe [from ICSD patterns (PDF # 77–2307)].

The surface morphology of the xerogel films was studied by field emission scanning electron microscopy (FESEM) (Figure 4.4b). The films appear dense, which is a typical characteristic of xerogels, and do not have macroscopic cracks that lead to island formation. Thickness and roughness analysis of the xerogel films by atomic force microscopy (AFM) measurements (Figure 4.4b) reveal that the films have micrometer scale thicknesses and comparatively high roughness values (the average thickness and roughness of the films are 1.2  $\mu\text{m}$  and 120 nm (Film 1, 4 mL of sol) and 1.7  $\mu\text{m}$  and 140 nm (Film 2, 5 mL of sol)).

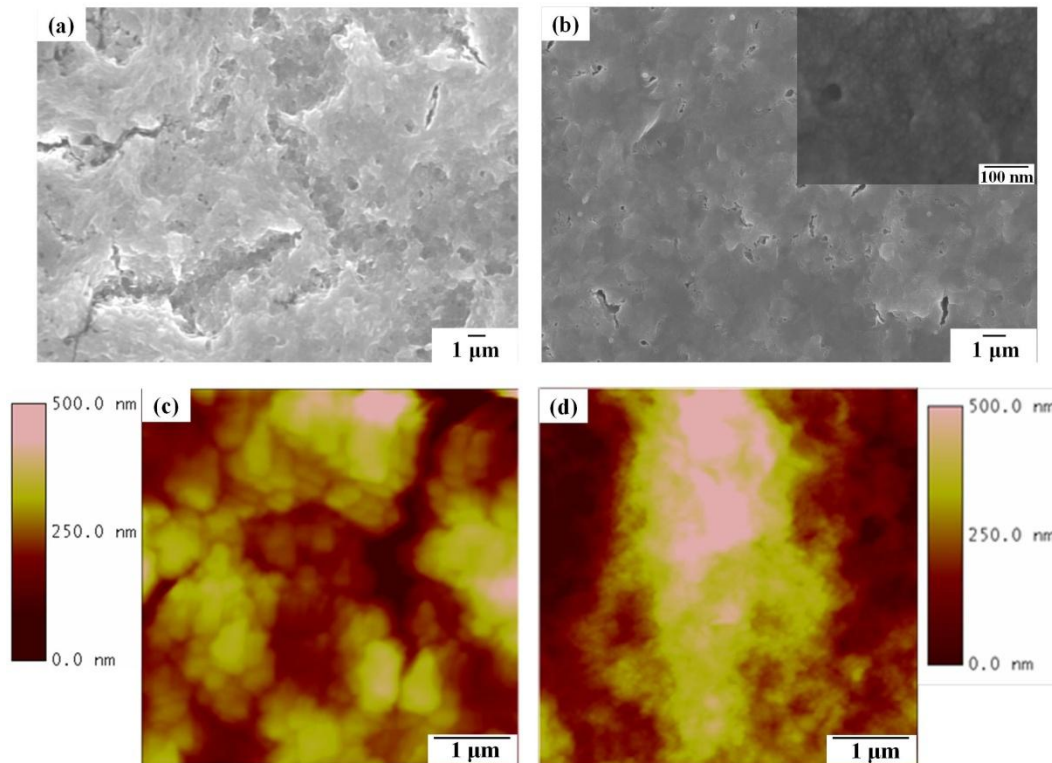


**Figure 4.4.** (a), (b) FESEM images, and (c), (d) AFM images of the CdSe/ZnS xerogel films deposited from 4 mL (left) and 5 mL (right) of sol. Films have dense and rough surface morphology. The inset of b shows the morphology of the film under higher magnification.

The sheet resistance,  $R_s$ , of films deposited from 5 mL of sol was measured by the van der Pauw method. Resistances are on the order of  $10^6 \Omega$  per square and conductivity,  $\sigma$ , is on the order of  $10^{-3} \text{ S cm}^{-1}$ . In order to compare  $\sigma$  of the sol–gel films directly to the NC precursor particles we tried to measure the  $R_s$  of relatively thick films ( $\sim 600 \text{ nm}$ ) of trioctylphosphine oxide (TOPO)-capped particles fabricated on a glass substrate by drop casting. However, we were not able to get a reading from the source meter, indicative of the highly insulating nature of the TOPO-capped CdSe/ZnS films. According to the literature, the  $R_s$  of TOPO-capped CdSe films with micron-scale thickness is on the order of  $10^{22} \Omega$  per square, thus we observe a sixteen

order of magnitude enhancement in conductivity by converting the NCs into xerogel films.<sup>122</sup> In fact, the  $\sigma$  of the xerogel NC films is close to that obtained from pyridine-capped CdSe thin films treated with cross-linking molecules ( $\sigma \sim 10^{-2} \text{ S cm}^{-1}$ ).<sup>57</sup> The high conductivity of the NC xerogel film is surprising since the particle interfaces are composed of oxidized sulfide linkages ( $\text{S}_n^{2-}$ ), and chemical reduction in solution leads to gel dispersion.<sup>56</sup>

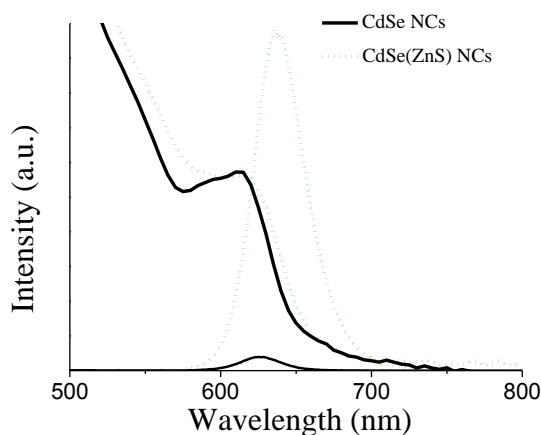
Since the high surface roughness could be adversely affecting the conductivity of xerogel films, attempts were made to deposit thinner films with low surface roughness by reducing the sol volume. Unfortunately, the decrease of sol volume resulted in macroscopic cracks on the film, and consequently, the conductivity reduced significantly.

#### **4.3.2 Uniform Thin Films of CdSe and CdS/ZnS NCs by Sol–Gel Assembly: Enabling Photoelectrochemical Characterization and Electronic Applications**

Although, fabrication of transparent, micron-thick CdSe/ZnS xerogel films is a major step toward practical exploitation of chalcogenide gels, the xerogel films were rough and fabrication of crack-free thinner films is difficult by this approach. Therefore, a new strategy was developed to fabricate high quality chalcogenide NC sol–gel thin films.

CdSe NCs were synthesized according to modified literature procedures and capped with thiolate ligands.<sup>101</sup> Figure 4.5 shows the UV–vis and PL spectra of purified TOPO/stearic acid-capped NCs dispersed in toluene. According to the first excitonic peak in the absorption spectrum, CdSe NCs were determined to have diameters of  $\sim 5.3 \text{ nm}$ .<sup>136,108</sup> After exchange with thiolate ligands, the band gap remained unchanged, but the PL was almost completely quenched due to hole trapping at surface thiolates (Figure 4.5).<sup>137</sup> The thiolate-capped NCs dispersed in methanol (sol) were then spin-coated onto substrates to form thin films of thiolate-capped NCs (sol films). Gelation was initiated by dipping the film into an oxidizing solution (TNM, in

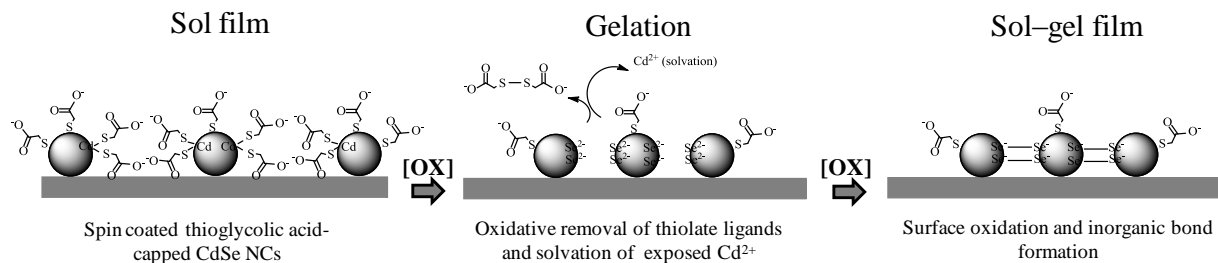
acetone). The films generated using MUA capping groups dissolved within a few seconds, indicating that the kinetics of gelation are not fast enough to overcome the redispersion of NCs in acetone. To increase the rate of oxidation of the thiolate ligands, the shorter chain ligand thioglycolic acid was used as the capping group. The short chain length is expected to afford easy accessibility of the oxidizing agent to the particle surface. Moreover, the shorter interparticle distances expected with thioglycolic acid as a ligand relative to MUA means the NCs will only have to migrate a short distance during the formation of interparticle bonds in the gelation process, which should prevent significant film cracking.



**Figure 4.5.** UV–vis and PL spectra of TOPO/stearic acid-capped CdSe and thioglycolic acid-capped CdSe NCs dispersed in toluene and methanol, respectively. PL intensities are normalized according to the fraction of the first excitonic absorption. PL quenching in the thioglycolic acidcapped QDs is attributed to hole-trapping at the surface thiolate.

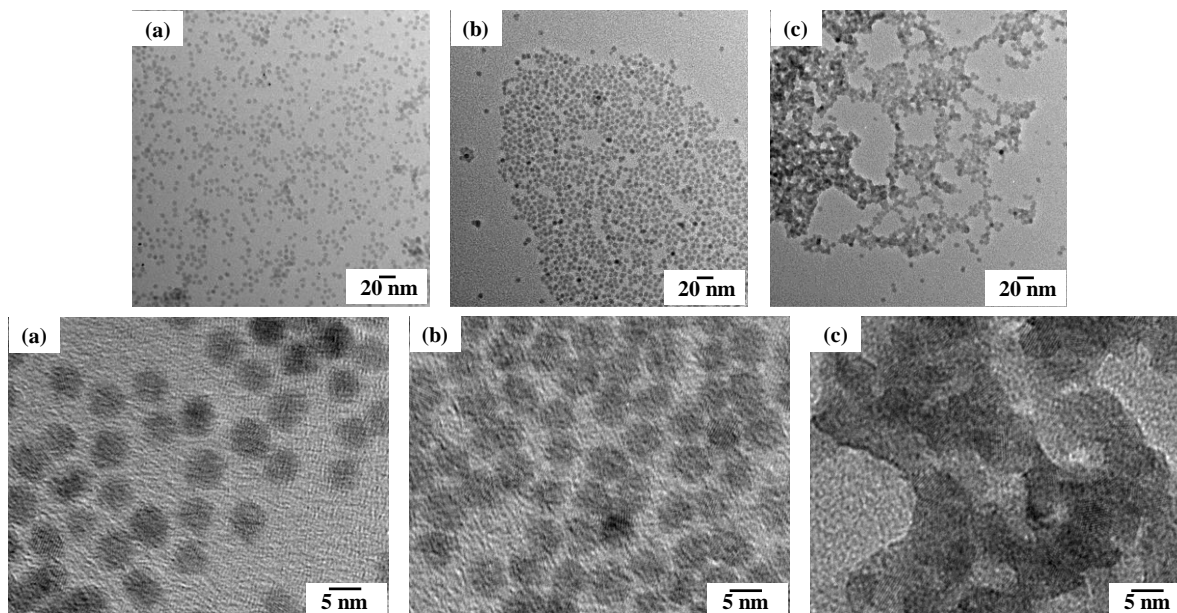
Spin-coated thioglycolic acid-capped NC films (sol films) ( $\sim 70$  nm thick) were immersed in solutions of TNM in acetone for one minute, followed by dipping in fresh methanol solution to remove the gelation byproducts (Scheme 4.2). In contrast to MUA-capped NCs, the

thioglycolic acid-capped NC films (sol films) did not disperse in the acetone/TNM solution and the resultant sol–gel NC films were also insoluble in methanol, suggesting the kinetics of oxidation are fast enough to remove the polar capping groups on the surface of NCs, inducing gelation, and making the film insoluble in polar as well as nonpolar solvents. The films were subsequently annealed at 250 °C for 30 min.



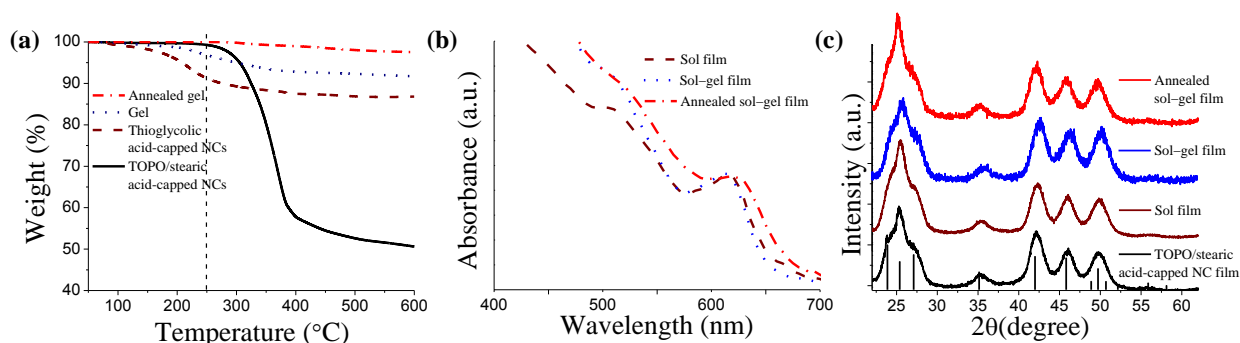
**Scheme 4.2.** Mechanism of oxidative ([OX]) gelation of a thioglycolic acid-capped NC film (sol film) submerged in a TNM solution.

Figure 4.6 shows TEM images of TOPO/Stearic acid-capped NCs and thioglycolic acid-capped NCs before and after addition of TNM. The discrete particles have been “wired” into a network by the oxidative treatment.



**Figure 4.6.** TEM images at two magnifications of (a) TOPO/Stearic acid-capped CdSe NCs, and (b) thioglycolic acid-capped CdSe NCs. (c) Corresponding TEM images of sample (b) after gelation showing formation of NC network.

Thermogravimetric analysis (TGA) was employed to follow the ligand exchange, gelation, and annealing processes using bulk samples. The originally synthesized CdSe NCs contained large quantities of organic surfactants (TOPO/stearic acid) as indicated by a  $\sim 50\%$  weight loss (Figure 4.7a). Successful exchange of the original organic ligands with thioglycolic acid was confirmed by the decrease of the weight loss down to  $\sim 13\%$ , since thioglycolic acid has a much lower molecular weight than the original ligands (TOPO/stearic acid). Moreover, thermal decomposition starts around  $220\text{ }^{\circ}\text{C}$  for TOPO/stearic acid-capped NCs, but after thioglycolic acid exchange the loss starts at a much lower temperature, below  $130\text{ }^{\circ}\text{C}$ , indicative of a significant chemical change in the surface ligands. The gelation causes removal of surface thiolate ligands from the NC surface, and as a result, further decreases the weight loss experienced during TGA down to just  $\sim 8\%$ .



**Figure 4.7.** (a) Thermogravimetric scans (under  $N_2$  flow,  $10\text{ }^\circ\text{C}/\text{min}$ ) of CdSe NCs before and after ligand exchange and a CdSe gel before and after annealing confirm the successful ligand exchange, loss of thiolate ligands during the gelation process, and removal of residual ligands in the annealing step. (b) UV–vis spectra of a thioglycolic acid-capped CdSe film before (sol film) and after gelation (sol–gel film), and after annealing the sol–gel film show that gelation causes minor surface etching of NCs (blue shift), and annealing results in greater NC–NC interaction (red shift). (c) XRD patterns of a TOPO/stearic acid-capped CdSe film, thioglycolic acid-capped CdSe film (sol film), a sol–gel film, and an annealed sol–gel film indicate negligible changes in crystallite size during the ligand exchange, gelation and annealing processes. The line diagram in (c) corresponds to bulk CdSe (from ICSD pattern PDF # 77-2307).

These processes can also be followed by FTIR analysis. FTIR of a TOPO/stearic acid-capped NC film has a prominent peak in the C–H stretching region that virtually disappears upon exchange with the short-chain thioglycolic acid ligand (Figure 4.8) consistent with a decrease in aliphatic hydrocarbon among the surface groups (i.e., loss of TOPO/stearic acid capping groups). Loss of TOPO is further confirmed by the absence of a P=O stretching vibration peak in the thioglycolic acid-capped NC film (sol film). A small peak due to  $\text{COO}^-$

stretching is observed in both the TOPO/stearic acid film and the sol film, consistent with the presence of stearic acid in the former and thioglycolic acid in the latter. Overall, the disappearance of C–H and P=O stretching while  $\text{COO}^-$  stretching is retained is consistent with the replacement of the bulky TOPO/stearic acid ligands with short chain thioglycolic acid.

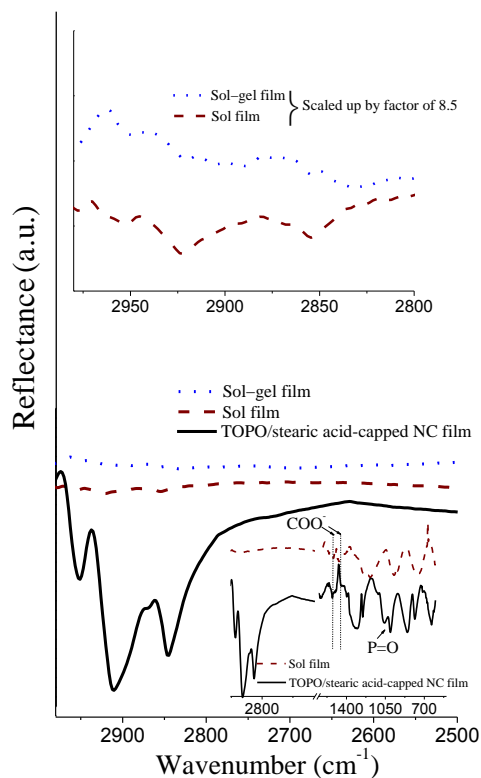


**Figure 4.8.** Bottom graph: C–H stretching region of the reflectance FTIR spectra of a TOPO/stearic acid-capped CdSe film, and thioglycolic acid-capped CdSe film before (sol film) and after gelation (sol–gel film). The inset shows the disappearance of the P=O stretching peak upon ligand exchange, and the presence of  $\text{COO}^-$  stretching in both TOPO/stearic acid-capped and ligand-exchanged sol film (due to stearic acid in the former and thioglycolic acid in the latter). The disappearance of C-H and P=O stretching while  $\text{COO}^-$  stretching is retained is consistent with the replacement of the bulky TOPO/stearic acid ligands with short chain thioglycolic acid. Top graph: IR spectra of a thioglycolic acid-capped CdSe film before (sol film) and after gelation (sol–gel film), scaled up by a factor of 8.5. Spectra are vertically shifted for clarity and demonstrate the further loss of organic groups upon gel formation. FTIR spectra were acquired on films deposited from NC solutions (TOPO/stearic acid- and thioglycolic acid-capped) with similar particle concentration.

The majority of the residual ligands are subject to decomposition at low temperatures (<250 °C) as indicated in Figure 4.7a where TGA analysis of an annealed gel (250 °C, 30 min) demonstrated only a 1–2% weight loss. This is important because a common problem with thermal treatment is that nanocrystals are not stable at the temperatures (>300 °C) needed to pyrolyze commonly employed organic surfactants, and thus the NCs frequently sinter in this process and lose quantum confinement.<sup>122</sup> This is not the case for our materials, as evidenced by absorption spectra and X-ray diffraction patterns of films (Figure 4.7 b, c). The absorption spectrum of a sol–gel film shows only a small blue shift of the first excitonic peak (5 nm, 17 meV) resulting from gelation. This may be due to surface etching during the gelation process. Removal of the thermally unstable residual ligands by annealing strengthens the connectivity of the NC network resulting in peak broadening and red shifting (10 nm, 33 meV) of the first excitonic peak relative to the sol–gel film. While this shift could be due to either the enhancement of interparticle coupling, crystallite growth, or a combination of these effects<sup>138,139</sup> a lack of change in the XRD peak breadths (which reflect crystallite size) suggests sintering is minimal. Thus, the major effect of the annealing step is to more effectively “wire” the particles into an interactive network.

Figure 4.9a shows photographs of sol–gel films before and after annealing. They appear crack-free, transparent and are visually identical. Microscopic evaluation of the films using FESEM reveal only nanoscale cracking of the film (Figure 4.9b–d) and AFM roughness measurements show the films (~70 nm thick) are smooth (roughness <2 nm) and uniform on the nanoscale (Figure 4.9e–g); no changes are observed during the gelation and annealing processes.

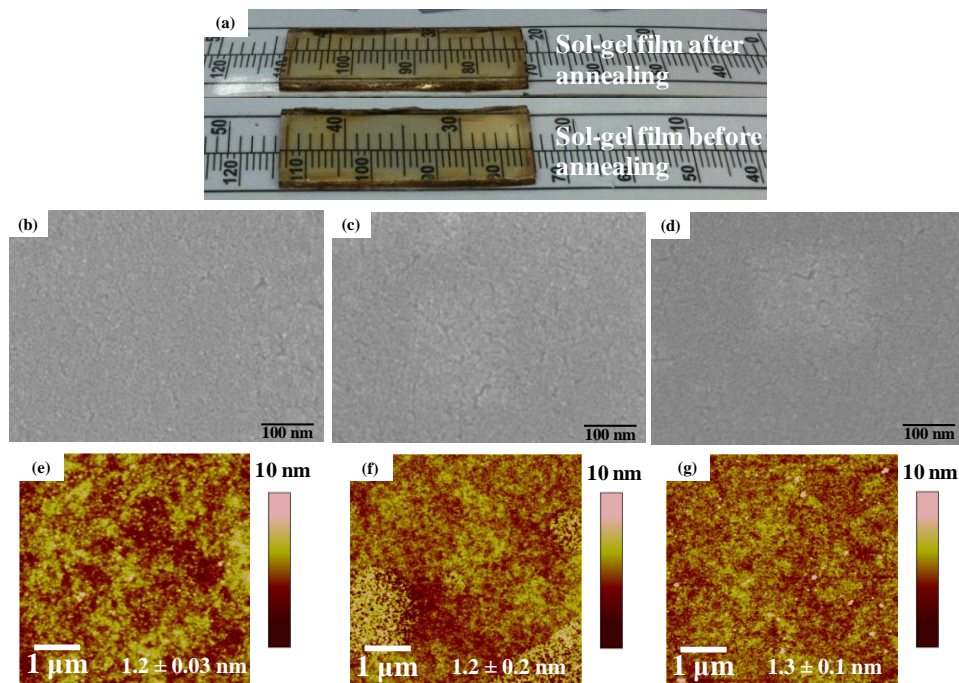


**Figure 4.9.** (a) Photographs of sol–gel films before and after annealing. FESEM images of a (b) thioglycolic acid-capped CdSe NC film (sol film) (c) sol–gel film, and (d) annealed sol–gel film. AFM images of a (e) thioglycolic acid-capped CdSe NC film (sol film) (f) sol–gel film, and (g) annealed sol–gel film. Both FESEM and AFM imaging confirm that there are no major morphological changes during the gelation and annealing processes.

To evaluate the potential of sol–gel NC films for optoelectronic applications, photoelectrochemical measurements were performed using a three-electrode system comprising the NC film on ITO as the working electrode, a Pt-coil counter electrode and a saturated Ag/AgCl reference electrode. A 0.1 M polysulfide aqueous solution ( $\text{Na}_2\text{S} + \text{NaOH} + \text{S}$ ) served as the electrolyte, and the photoresponse of TOPO/stearic acid-capped CdSe NC films (as-prepared) and CdSe sol–gel films (annealed at 250 °C) were studied under white light illumination (100 mW/cm<sup>2</sup>).

The TOPO/stearic acid-capped CdSe NC films did not exhibit a detectable photocurrent, indicating poor charge transport that is likely due to the highly insulating nature of the bulky organic ligands. However, CdSe annealed sol–gel films displayed a  $\sim 75 \mu\text{A cm}^{-2}$  anodic photocurrent at  $-0.57 \text{ V}$  (solution redox potential) with respect to the Ag/AgCl reference electrode, comparable to the only other report of photocurrent measurements on CdSe systems we could find in the literature (“bare” particle surfaces),<sup>140</sup> suggesting a significant improvement in charge transport arising from the interconnected NC network within the annealed sol–gel films (Figure 4.10). The rest potential of the annealed sol–gel films shifted from  $-0.65$  to  $-1.00 \text{ V}$  (vs. Ag/AgCl) (Figure 4.10.b) upon introduction of light, consistent with intrinsic n-type doping in the films, which can also be shown in the rectifying shape of the  $I - V$  curve (Figure 4.10b). The enhanced communication between adjacent NCs enables the photogenerated electron carriers to travel to the ITO electrode efficiently while holes are captured by  $\text{S}^{2-}$  and transferred to the counter electrode; consequently, the recombination efficiency of the electron-hole at the NC surface is greatly reduced and photocurrent increases dramatically. There was a slight decrease of photocurrent at the beginning; however, as the systems have not yet been fully optimized, this is not unexpected. Stable photocurrents were observed after some time.

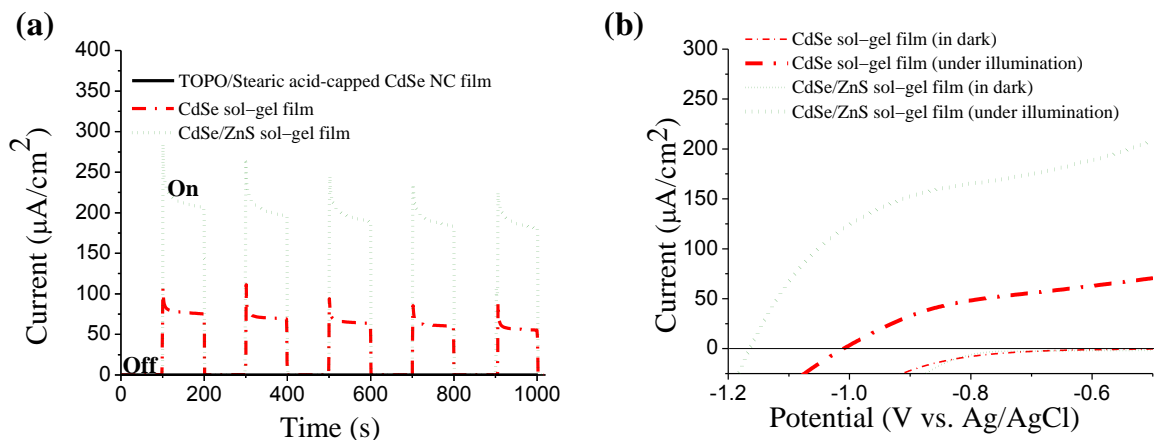


**Figure 4.10.** (a) Photocurrent response of a TOPO/stearic acid-capped CdSe NC film, and CdSe and CdSe/ZnS sol-gel films (annealed at 250 °C), to chopped white light irradiation (100  $\text{mW}/\text{cm}^2$ ) at -0.57 V (solution redox potential) with respect to a Ag/AgCl reference electrode confirms the enhancement of charge transport properties in annealed sol-gel films. (b)  $I - V$  characteristics of the CdSe and CdSe/ZnS sol-gel films (annealed at 250 °C). The ZnS shell leads to increased photocurrent, enhanced photovoltage, and sharper fill factor in annealed sol-gel films.

The promising photoresponse in the gel thin films can be rationalized by the linkage of NCs during the gelation process. As previously mentioned, treatment of thioglycolic acid-capped NC films (sol films) with oxidant, TNM, removes surface thiolates and oxidizes the exposed chalcogenide on the NC surface, leading to dichalcogenide-bonded NCs.<sup>56</sup> In the case of CdSe NCs, removal of thiolate ligands causes solvation of exposed  $\text{Cd}^{2+}$  ions, and consequently, the  $\text{Se}^{2-}$ -rich NC surface can undergo further oxidation resulting in NCs linked by  $(\text{Se})_2^{2-}$  (Scheme 4.2). To confirm the Se rich interfaces between NCs in the gel relative to the surface of discrete NCs, we performed high-angle annular dark-field scanning TEM (HAADF-STEM) imaging with EDS elemental mapping using the ChemiSTEM technology developed by FEI. Figure 4.11 show

the HAADF images and EDS elemental mapping of TOPO/stearic acid-capped CdSe NCs, and thioglycolic acid-capped NCs gelled by treatment with TNM. The NCs are highly crystalline and have significant Cd (blue) and Se (red) signal throughout. In contrast, the signal for gelled particles is dominated by Se, which is continuous throughout the interconnected network, consistent with Se-mediated interparticle bonding. The deficiency in Cd in the gelled network relative to the starting particles is particularly evident when Figure 4.11 images c and g are compared.

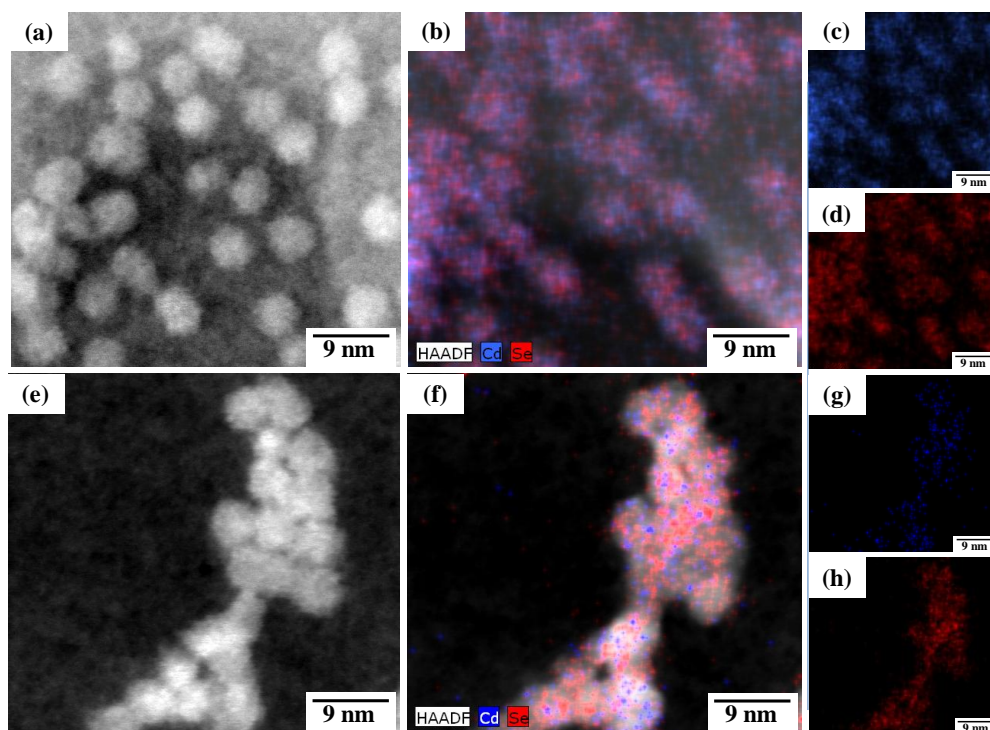


**Figure 4.11.** (a) A HAADF-STEM image of TOPO/stearic acid-capped CdSe NCs; and (b), (c), (d) EDS elemental mapping for Cd and Se. (e) A HAADF-STEM image of thioglycolic acid-capped CdSe NCs after gelation, and (f), (g), (h) EDS elemental mapping for Cd and Se. A distinct increase in Se signal relative to Cd is observed in gelled NCs relative to TOPO/stearic acid-capped NCs, consistent with the proposed mechanism of gelation.

We next sought to explore the effect of passivation of the CdSe surface on the photoconductivity of the films, considering the fact that surface modification during the ligand exchange, gelation, and annealing processes could lead to defect-related recombination. Nonradiative recombination can be suppressed by passivating the surface states of the chromophore (CdSe) by growth of a shell consisting of a material with a larger band gap, ZnS.<sup>141</sup> Although Type-I band alignment, as occurs when the valence band and conduction band of the core are sandwiched by those of the shell, which is the case for CdSe/ZnS, does not favor exciton dissociation, several reports have shown that enhancement of the photocurrent for NC-sensitized solar cells is realized when fabricated using CdSe/ZnS core/shell NCs.<sup>142,143</sup> Moreover, Zhu and co-workers have observed that the charge separation rate in CdSe/ZnS NCs depends on the shell thickness, with an exponential decrease in the charge separation kinetics with increasing ZnS shell thickness.<sup>144</sup> Thus, in order to improve surface passivation without overly compromising charge separation, we overcoated the core CdSe NCs with a thin shell of ZnS (~1–2 monolayers).

ZnS was grown on CdSe cores by slowly injecting a mixture of diethyl zinc and bis(trimethylsilyl)sulfide as zinc and sulfur precursors.<sup>32</sup> Figure 4.5 shows the UV–vis and PL spectra of core and core/shell NCs dispersed in toluene. The significant enhancement in band-edge PL intensity upon overcoating is consistent with a reduction of hole traps on the NC surface.

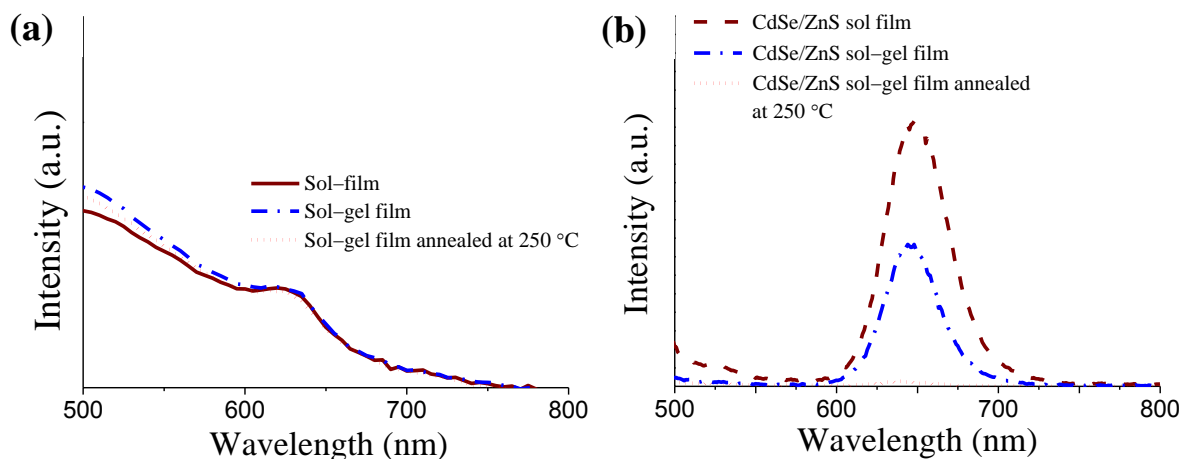


**Figure 4.12.** (a) UV–vis and (c) PL spectra of a thioglycolic acid-capped CdSe/ZnS film before gelation (sol film), after gelation (sol–gel film), and after gelation and annealing (sol–gel film annealed at 250 °C) indicates better electronic coupling of NCs is occurring during the gelation and annealing processes, resulting in free charge carriers and suppression of PL. PL intensities in (b) are normalized according to the fraction of the first excitonic absorption peak in (a).

The subsequent gelation and annealing processes have a large effect on the optical properties; the PL intensity decreases upon gelation and is almost completely quenched after annealing (4.b). PL quenching can be attributed to formation of surface trap states or generation of free charge carriers due to the enhancement of electronic coupling.<sup>128,131</sup> Because of the surface passivation provided by the thin shell of ZnS, the contribution from the latter to the PL quenching should be significant. Consistent with a hypothesis of decreased surface trapping giving rise to increased free charge carriers, a more than 2-fold increase of photocurrent (Figure 4.10a) and higher optical conversion quantum yield (Figure 4.13a) were observed for annealed core/shell sol–gel films compared to the corresponding CdSe-only films. The notion that the presence of a ZnS shell decreased surface trapping as a major recombination pathway is also

supported by the measured change in rest potential on moving from dark to illuminated conditions (Figure 4.1). At steady-state, the attainable photovoltage (i.e., the difference between the rest potential in the dark and under illumination) of a photoelectrode is a measure of the ratio of the product of charge carrier concentrations under illumination to the product of charge carrier concentrations in the dark

$$\Delta V = \frac{kT}{q} \ln \left( \frac{np}{n_i^2} \right) \quad (4.1)$$

where  $\Delta V$  is the difference in rest potentials in the dark and under illumination,  $k$  is Boltzmann's constant,  $T$  is temperature,  $q$  is the unsigned charge of an electron,  $n$  is the steady-state electron concentration,  $p$  is the steady-state hole concentration, and  $n_i$  is the intrinsic concentration of carriers in the semiconductor. All recombination processes act to minimize  $n$  and  $p$  under illumination. The larger measured change in rest potential for the ZnS-coated CdSe sol-gel film as compared to the bare CdSe sol-gel film under the same illumination conditions implies a larger population imbalance and, accordingly, a decreased rate of total recombination. The increased net anodic photocurrents for the ZnS-coated CdSe sol-gel films also imply sufficiently fast hole transfer through the ZnS shell. Quenching experiments with CdSe/ZnS NCs have previously demonstrated that strong coupling of a CdSe core with acceptors/donors on the opposite side of the thin ZnS shell (<5 monolayers) allows rapid charge transfer.<sup>145,146</sup> Accordingly, we posit that the thinness of the ZnS layer reduces trap sites where recombination can occur while enabling strong electronic coupling between the CdSe core and the dissolved solution redox mediator. This leads to improvement of all aspects of the photoresponse of annealed CdSe/ZnS sol-gel films relative to the corresponding CdSe sol-gel films, as reflected in Figure 4.10b; that is, increased photocurrent, enhanced photovoltage, and sharper fill factor.

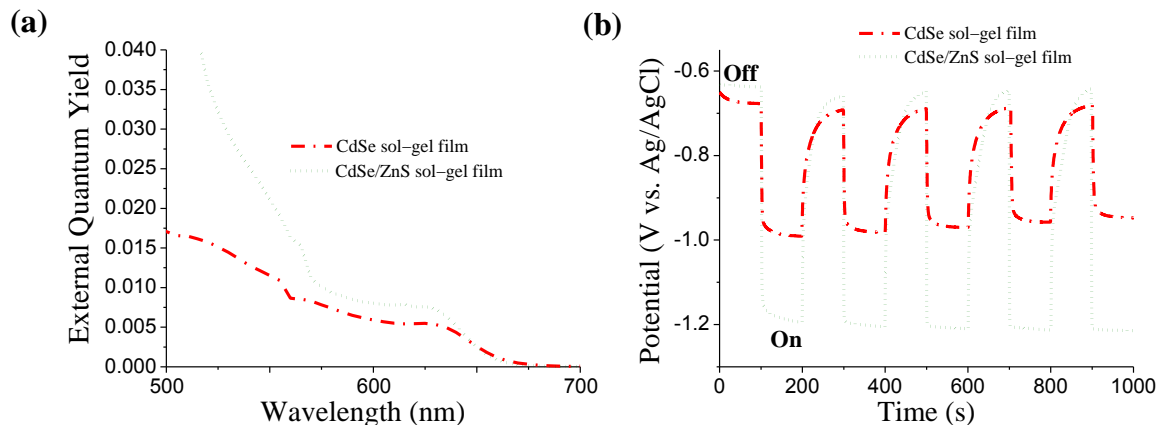


**Figure 4.13.** External quantum yield of CdSe and CdSe/ZnS sol-gel films (annealed at 250 °C) at -0.57 V (solution redox potential) with respect to a Ag/AgCl reference electrode. The increase in external quantum yield is consistent with increased electronic coupling and decreased trap states in the CdSe/ZnS annealed sol-gel films relative to the CdSe annealed sol-gel films. (b) Rest potential response of CdSe and CdSe/ZnS sol-gel films (annealed at 250 °C) to on-off cycles of white light irradiation. The larger measured change in rest potential for the ZnS coated CdSe sol-gel film is attributed to a decreased rate of recombination due to surface passivation.

Elemental mapping of the CdSe/ZnS NCs and sol-gel network (Figure 4.14) supports the hypothesis for the enhanced performance of core/shell sol-gel films relative to CdSe sol-gel films. As shown in Figure 4.14a, the CdSe core is only partially covered by the ZnS shell. Because of these imperfections in the ZnS shell, the CdSe cores have points of direct contact within the network that is created by the oxidative gelation process (Figure 4.14b, c). The decrease of defect-related recombination by partial passivation of the surface states that is achieved by growing a thin shell of ZnS, combined with direct contact of CdSe cores through defects in the shell<sup>142</sup> may collectively contribute to the enhancement of photocurrent for the CdSe/ZnS sol-gel films relative to CdSe films.

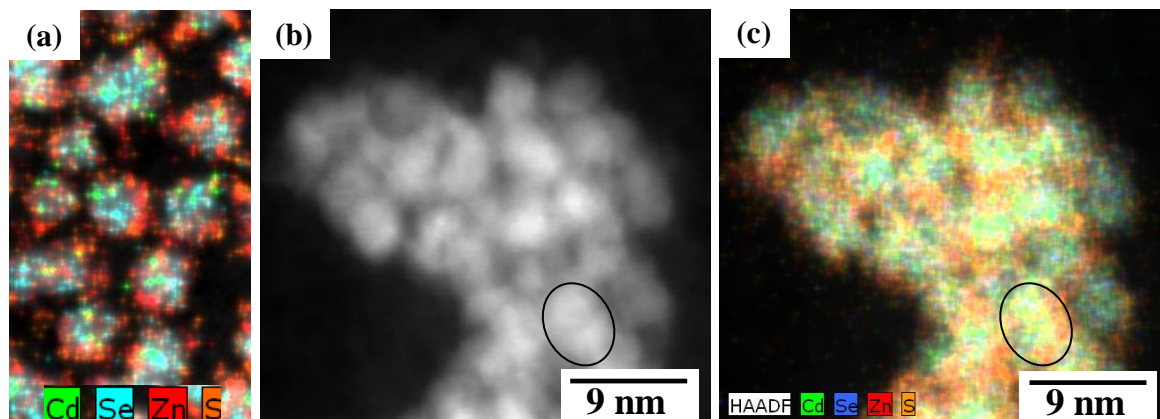


**Figure 4.14.** (a) EDS elemental mapping of TOPO/stearic acid-capped CdSe/ZnS NCs for Cd, Se, Zn and S shows that the CdSe cores are only partially covered by the ZnS shell. (b) A HAADF-STEM image of thioglycolic acid-capped CdSe/ZnS NCs after gelation, and (c) EDS elemental mapping for Cd, Se, Zn and S in CdSe/ZnS gels. The circled area shows one of several places where there appears to be direct contact between CdSe cores.

#### 4.4 Conclusions

Sol–gel methods can be employed to fabricate micron thickness CdSe/ZnS xerogel films with high transparency and luminescence. The films were surprisingly conductive ( $\sigma = 10^{-3} \text{ S cm}^{-1}$ ) consistent with the existence of an electrically connected network of NCs within the xerogel film. The network enhances the transport of mobile charge carriers despite the strong potential for trapping at the oxidized interfaces and/or bond cleavage due to reduction. However, fabrication of nanoscale-thick smooth films is difficult by this method due to film cracking.

Accordingly, a new method to fabricate high quality CdSe NC sol–gel films by applying gelation strategies to spin-coated thioglycolic acid-capped NC films (sol films) was developed. This method enables improved charge transport properties in NC solids by enhancing interparticle coupling via formation of oxidation-induced dichalcogenide linkages. Overcoating

CdSe NCs with a thin ZnS shell reduces unpassivated surface states, and thus charge-trapping, and results in a more than 2-fold increase of photocurrent. The ability to tune interfacial and surface characteristics for the optimization of photophysical properties suggests the sol–gel approach may yield NC thin films suitable for a range of optoelectronic applications.

**CHAPTER 5**  
**CONNECTING THE (QUANTUM) DOTS: TOWARDS HYBRID**  
**PHOTOVOLTAIC DEVICES BASED ON CHALCOGENIDE GELS**

### **5.1 Introduction**

Organic solar cells based on conjugated polymers are among the most promising devices for solar energy conversion. The “classical” device consists of a bulk-heterojunction of a polymer–fullerene network, comprising poly(3-hexylthiophene) (P3HT) and the soluble fullerene derivative [6,6]-phenyl C<sub>61</sub>-butyric acid methyl ester (PC<sub>61</sub>BM). The introduction of small alkyl thiol molecules, optimization of solvent conditions, and use of conjugated copolymers with smaller band gaps along with PC<sub>71</sub>BM enabled significant improvements in the efficiency of these devices, reaching ~7%.<sup>147</sup> However, bottlenecks such as morphology control, the mismatch with the solar spectrum and stability still persist.

The easily tunable optical properties, high absorption coefficients, and high electron affinity and mobility relative to organic materials,<sup>148</sup> as well as the potential for generation of multiple excitons, make inorganic semiconductor nanocrystals (NCs) such as CdSe,<sup>64,149</sup> CuInSe<sub>2</sub>,<sup>150</sup> PbS,<sup>151</sup> and PbSe<sup>152</sup> promising alternatives to organic fullerene derivatives in hybrid solar cell devices. However, the highest efficiencies achieved for this kind of NC-based solar cells are still around 3%,<sup>153,154</sup> mainly due to the poor charge transport properties of the inorganic phase, where transport occurs by hopping through a percolation pathway. Realization of a highly-interconnected pathway is a great challenge because the surface ligands used to passivate the NC surfaces have highly insulating, long aliphatic chains. Improved device performance via surface modification has been achieved by exchange with smaller ligands (e.g.

alkyl amines,<sup>155</sup> pyridine,<sup>64</sup> benzenedithiol<sup>154</sup>), shortening of long chain groups by thermal cleavage,<sup>156</sup> or removal of excess surface groups by performing additional washing steps.<sup>157</sup>

As discussed in Chapter 1 (Section 1.5), sol–gel methods can be used to assemble metal chalcogenide NCs into gels, xerogels and aerogels where NCs form a percolation network with inorganic particle interfaces that do not present the barriers to electrical transport that are endemic in organic-ligated NCs and remain quantum-confined.<sup>47,49</sup> This chapter describes the details of a study that evaluated the potential of chalcogenide aerogels for hybrid photovoltaic applications. In this work, variation of morphology and photocurrent generation with the composition of hybrid films of CdSe/ZnS core/shell aerogels and P3HT was investigated and the suitability of those novel hybrids for photovoltaic applications is discussed. The work described in this chapter has been published as “Connecting the (quantum) dots: towards hybrid photovoltaic devices based on chalcogenide gels” (De Freitas, J. N.; Korala, L.; Reynolds, L. X.; Haque, S. A.; Brock, S. L.; Nogueira, A. F., *Physical Chemistry Chemical Physics* **2012**, *14* (43), 15180-15184).

## 5.2 Experimental Section

All the chemicals used in the syntheses described in this chapter are listed in Chapter 2 (Section 2.1). Materials were characterized by performing X-ray diffraction (XRD), UV–vis spectroscopy, FTIR spectroscopy, Atomic force microscopy (AFM), transmission electron microscopy (TEM), and photoelectrochemical measurements were performed as described in Chapter 2.

### 5.2.1 Synthesis of CdSe/ZnS Core/shell NCs

CdSe/ZnS NCs were synthesized and exchanged with 11-mercaptoundecanoic acid (MUA) as described in Chapter 4 (Section 4.2.1.2 and 4.2.2).

### 5.2.2 Synthesis of CdSe/ZnS Core/shell Aerogels

MUA-capped NCs were washed with ethyl acetate two times and then dispersed in methanol (10 mL of methanol in two vials) and gelation was initiated by adding 50  $\mu\text{L}$  of methanolic solution of 3% tetranitromethane (TNM). Wet gels were aged for several days and exchanged with acetone to remove byproducts, followed by liquid  $\text{CO}_2$  exchange in a critical point drier, and drying by supercritical extraction, resulting in the formation of aerogels.

### 5.2.2 Deposition of Films

Films were deposited on plain or indium tin oxide (ITO) coated glass cleaned by sonication in acetone, isopropanol and chloroform respectively. CdSe/ZnS NC or aerogel dispersions in toluene were drop cast, and P3HT and hybrid P3HT:NC and P3HT:aerogel mixtures in toluene were spin coated (1500 rpm, 40s) onto the substrates.

## 5.3 Results and Discussion

CdSe/ZnS core/shell NCs were synthesized according to literature methods with slight modifications<sup>100,32</sup> and then treated with a basic 11-mercaptoundecanoic acid (MUA) solution to achieve ligand exchange with the thiolate. After removing excess thiolate ligands, NCs were dispersed in methanol to make the sol and gelation was initiated by adding tetranitromethane (TNM). Wet gels were aged for several days, exchanged with acetone to remove by-products, followed by liquid  $\text{CO}_2$  exchange and drying by supercritical extraction.

Figure 5.1 schematically represents the sol–gel transformation of CdSe/ZnS NCs, initiated by oxidation of surface thiolate ligands by TNM. Removal of surface ligands is followed by the solvation of surface  $\text{Zn}^{2+}$  ions. Further oxidation of  $\text{S}^{2-}$  on the NC surfaces links the NCs together via sulfide bonding, forming the gel network. Supercritical drying of wet gels results in aerogels.

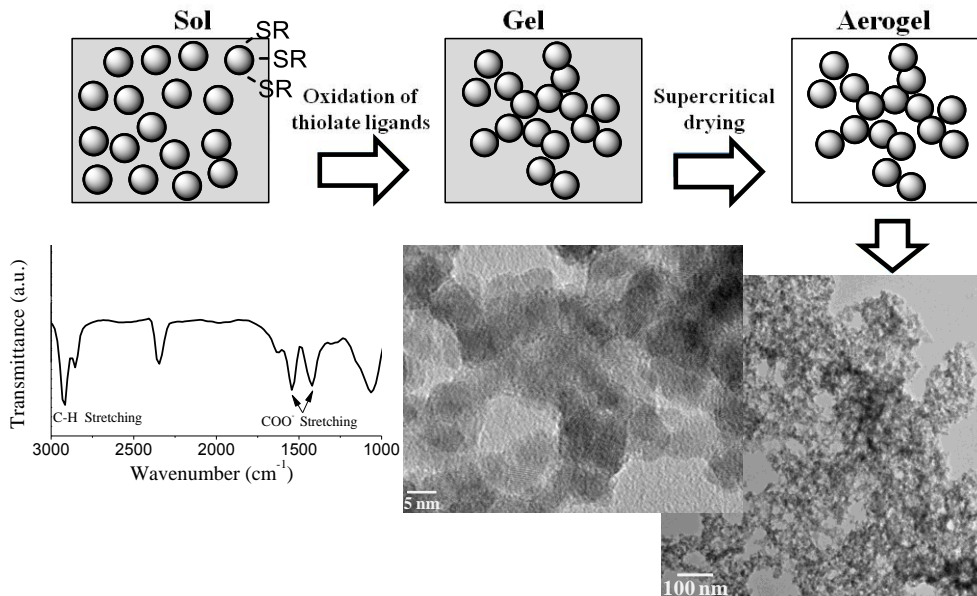


**Figure 5.1.** Schematic representation of the synthesis of aerogels from MUA-capped NCs, and TEM images (right) and a FTIR spectrum (left) of a CdSe/ZnS aerogel.

The process of gelation and supercritical drying removes the majority, but not all, of the thiolate ligands, as is evident from the FT-IR spectrum of the aerogel (Figure 5.1). Generally, about ~15% (by mole) of the ligands remain.<sup>158</sup> The residual ligands are present on the surface of the aerogel network, not at the interface, and are not expected to impact particle–particle conductivity, although they may have a significant effect on charge separation at the interface between the aerogel and P3HT.

Both CdSe/ZnS NCs and aerogels were mixed with poly(3-hexylthiophene) (P3HT) and dispersed in toluene in order to fabricate hybrid films of NC:polymer and aerogel:polymer. For NCs, additional washing steps were employed to partially remove original ligands and this leads to some aggregation of NCs. Figure 5.1 shows low- and high-resolution transmission electron microscopic (TEM) images of a CdSe/ZnS aerogel. The presence of end-to-end connected NCs (joints) within the aerogel network is visible in the TEM images. As indicated in Figure 5.2, end-

to-end connections lead to a more penetrating network for the aerogels (Figure 5.2b), compared to physically aggregated NCs (Figure 5.2a), once mixed with the P3HT. This is especially evident in samples with lower concentrations of inorganic materials. Importantly, mixing with P3HT does not disrupt the gel network.

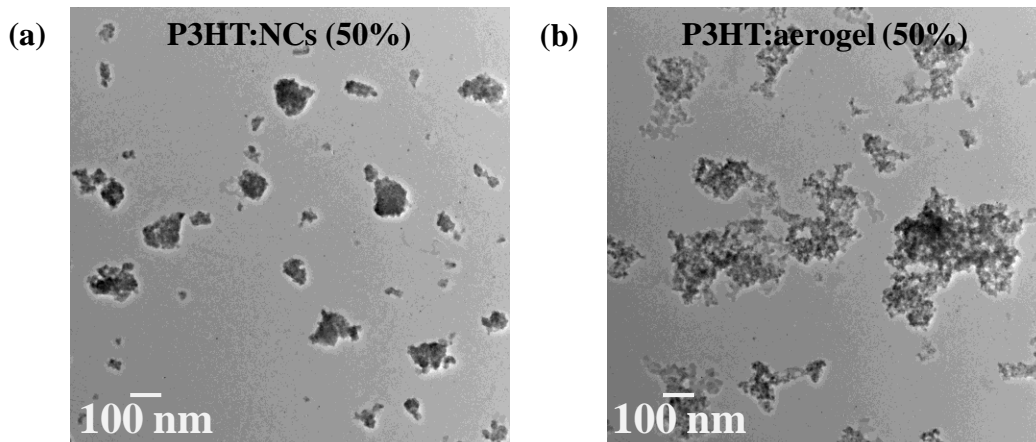


**Figure 5.2.** (a) P3HT:NC and (b) P3HT:aerogel mixtures containing 50 wt% inorganic material.

AFM analysis of hybrid films containing 50 and 90 wt% of inorganic material (NC or aerogel) reveals the presence of large clusters/aggregates (Figure 5.3). However, they appear to be well spread out in the P3HT:aerogel films, whereas aggregates appear to be more concentrated in certain regions of P3HT:NC films as also evidenced in TEM images (Figure 5.2). Hybrid films containing aerogels are rougher than films containing NCs: the root mean square (RMS) roughness was estimated to be ca. 110 nm and ca. 70 nm for films containing 90 wt% of aerogel and NCs, respectively.

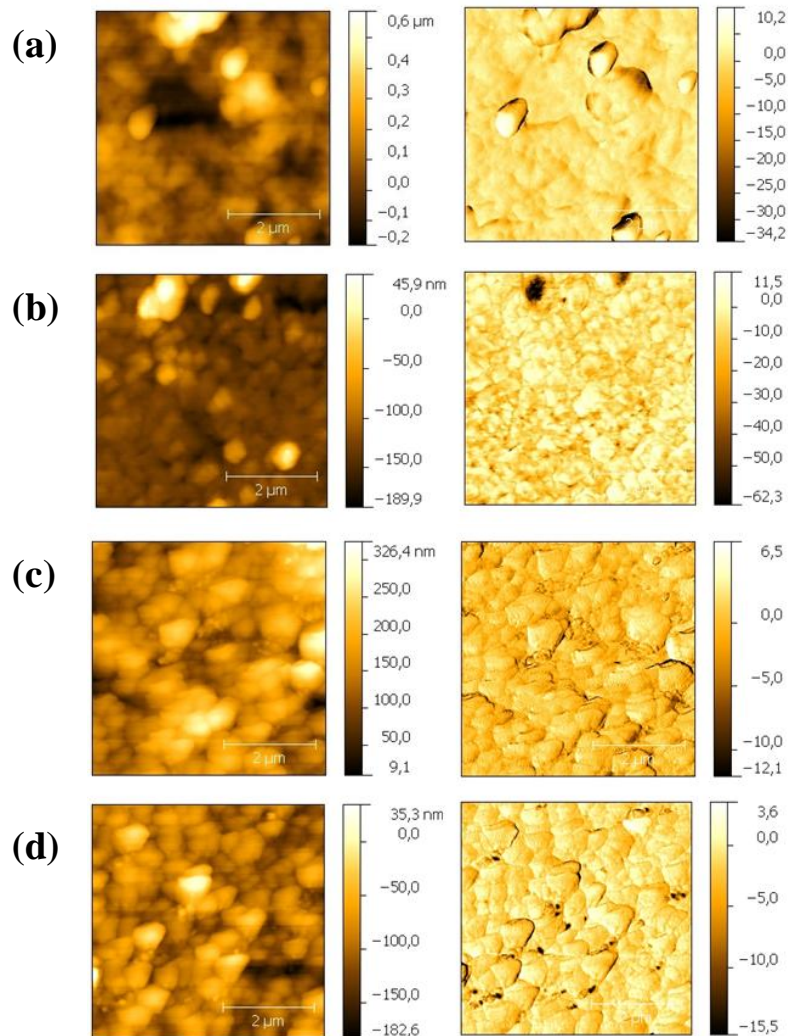


**Figure 5.3.** AFM images obtained in tapping mode for P3HT films containing (a) 90 wt% and (b) 50 wt% of CdSe/ZnS NCs, and (c) 90 wt% and (d) 50 wt% of CdSe/ZnS aerogel, deposited onto glass slides. Left images show topography, while right images show phase information.

Figure 5.4 shows the UV–vis absorption spectra of CdSe/ZnS NCs and aerogels (dispersed in toluene) and P3HT. The absorption profile of the aerogels is similar to that of the NCs used to prepare the aerogels. The first excitonic peak at  $\sim 615$  nm indicates that each nanocrystal in the aerogel network is  $\sim 5.3$  nm in diameter,<sup>108,136</sup> i.e., the quantum confinement effects of the respective nanometer scale building blocks are almost fully maintained despite

aggregation into a 3-D connected network, as previously observed.<sup>47</sup> The inorganic materials harvest light in the wavelength region coincident with the  $\pi \rightarrow \pi^*$  transition of P3HT (maximum at 550 nm) and the shoulder attributed to vibronic species (maximum at 600 nm).

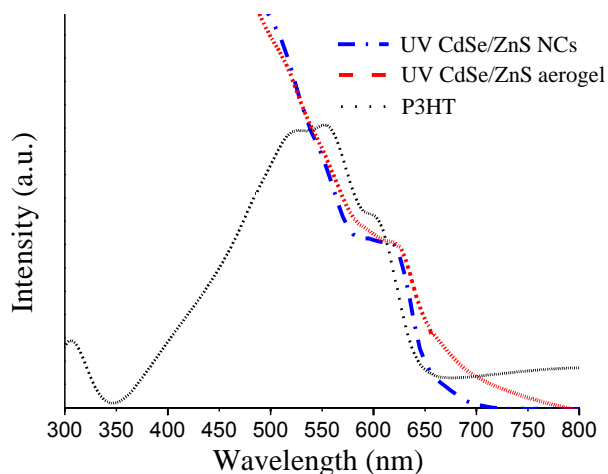


**Figure 5.4.** UV–vis absorption spectra of toluene dispersions of CdSe/ZnS NCs and aerogel, and a P3HT film.

Figure 5.5 shows the steady-state absorption spectra as a function of increasing CdSe/ZnS concentration in P3HT:NC and P3HT:aerogel hybrid films. There is an enhancement in light scattering as the CdSe/ZnS : P3HT ratio is increased for both types of films. In solar cells, light scattering can increase the optical path length within the active layer, offering the possibility of enhanced absorption, and thus, enhanced photocurrent generation.

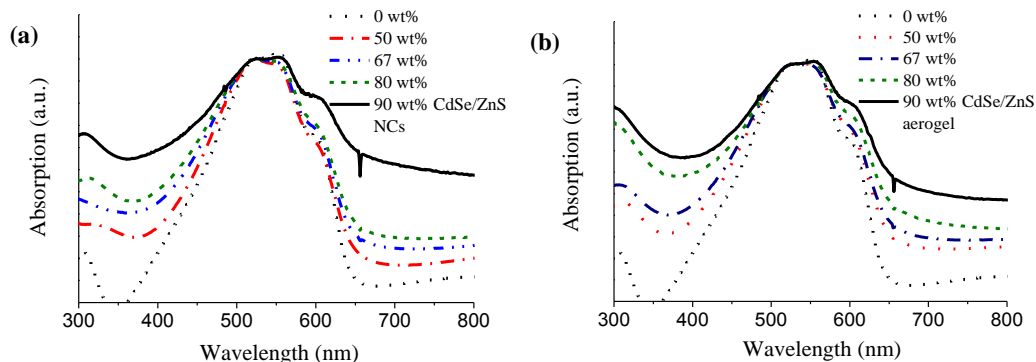


**Figure 5.5.** Steady-state absorption spectra of hybrid films of (a) P3HT:NCs (b) P3HT:aerogel with different weight ratios of CdSe/ZnS.

In order to compare the charge carrier generation, separation and transport in the P3HT:aerogel films with P3HT:NC films, photoelectrochemical measurements were obtained in a three-electrode cell connected to a potentiostat (Eco Chemie Autolab PGSTAT10). Ag/AgCl and a Pt wire were employed as a reference and counter electrode, respectively, and a 0.1 M aqueous solution of  $\text{Na}_2\text{SO}_4$  saturated with  $\text{O}_2$  was used as electrolyte. Working electrodes with an active area of  $1 \text{ cm}^2$  were prepared by drop casting or spin coating toluene dispersions of the materials onto ITO-coated glass. The current characteristics were recorded as a function of time, while repeated on-off cycles of white light illumination ( $100 \text{ mW cm}^{-2}$ ) were applied. First, NCs, aerogel and P3HT were analyzed individually. The original organic ligand-capped NC films showed negligible photocurrent response upon light illumination, indicative of poor charge transport in the films. However as mentioned previously, extra washing steps were employed to partially remove organic ligands that in turn leads to physical aggregation of the NCs and consequently improvement of photocurrent response. Figure 5.6 shows the photocurrent responses for photoelectrodes prepared by depositing NCs, aerogels and P3HT. Upon light illumination, prompt photocurrent generation in each electrode was observed. NC and aerogel

films show n-type behavior, while P3HT presents p-type behavior, consistent with the electrons as mobile charge carriers in the CdSe/ZnS phase and holes in the P3HT phase (Figure 5.6).

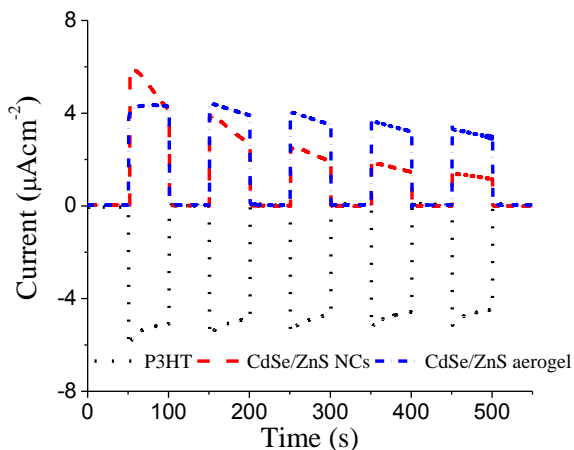


**Figure 5.6.** Photocurrent response of NC, aerogel and P3HT films under white light illumination ( $100 \text{ mW cm}^{-2}$ ).

Figure 5.7 shows photoelectrochemical measurements of P3HT:CdSe/ZnS (NCs or aerogel) hybrid films containing different concentrations of inorganic material by weight. Bare P3HT electrodes produce significantly lower currents than photoelectrodes assembled with hybrid films. The dramatically increased p-type photocurrent in the hybrid films is indicative of effective charge carrier separation at the organic-inorganic interface, which increases the formation of polarons in the polymer phase. Moreover, electrons are transported through the inorganic phase and ultimately scavenged by the  $\text{O}_2$  in electrolyte. A scheme of the expected charge transfer processes in these systems is provided in Figure 5.8.

Interestingly, the systems containing P3HT:aerogel and P3HT:NCs behave differently as the concentration of the inorganic material increases. At low concentrations of inorganic

materials ( $\leq 80$  wt%), the photocurrents delivered by P3HT:aerogel electrodes are higher than those delivered by P3HT:NC electrodes. This is related to the formation of a percolation network, required for efficient charge transport. For aerogel-based films, some percolation paths are preformed during the synthesis of the aerogel due to the controlled aggregation of NCs by formation of chemical bonds between NCs, while for NC-based films, the percolation limit is typically achieved only at very high concentrations of NCs (e.g., the best photovoltaic responses are usually obtained when  $\sim 90$  wt% of NCs are incorporated into the polymer matrix<sup>159</sup>). When the concentration reaches 90 wt%, the photocurrent of the NC-based electrode becomes similar to the aerogel-based electrode. Under this condition, both samples achieved effective formation of 3-D interconnected networks. It is worth noting that there is some degree of NC aggregation in the P3HT:NC electrodes (Figure 5.2a), due to partial removal of surface ligands.

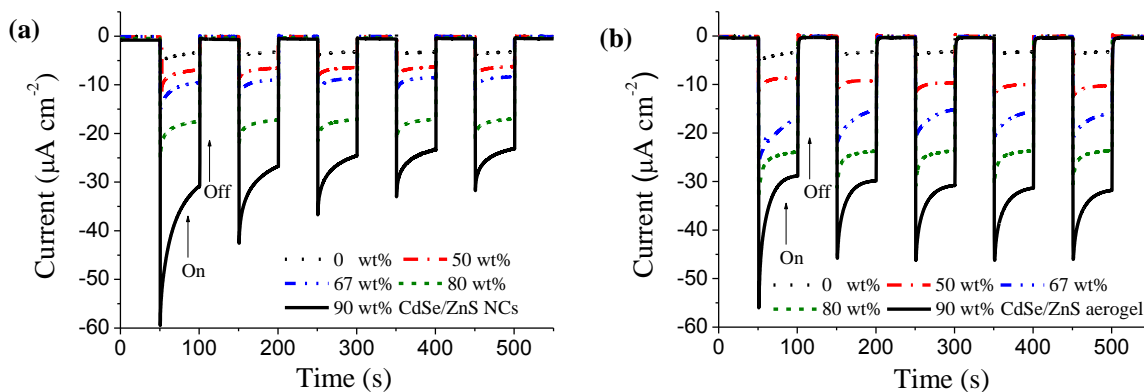


**Figure 5.7.** Photocurrent response of (a) P3HT:NC and (b) P3HT:aerogel films under white light ( $100 \text{ mW cm}^{-2}$ ).

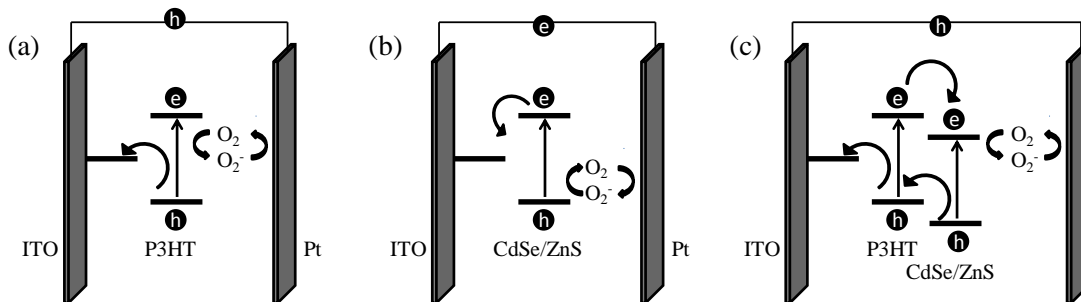


**Figure 5.8.** Scheme of charge transfer processes expected for systems containing electrodes based on (a) P3HT, (b) CdSe/ZnS NCs or aerogel, and (c) P3HT:CdSe/ZnS NCs or aerogel hybrid films, in the presence of a 0.1 M  $\text{Na}_2\text{SO}_4$  electrolyte saturated with  $\text{O}_2$  and under white light irradiation.

## 5.4 Conclusions

The potential of chalcogenide aerogels for hybrid photovoltaic devices was evaluated by studying photocurrent generation in hybrid films of CdSe/ZnS aerogel and poly(3-hexylthiophene) using photoelectrochemical measurements. Compared to organically capped, physically aggregated NCs, the aerogels showed higher photocurrent indicative of efficient charge carrier generation, separation and transport in films containing lower loadings of inorganic material in combination with P3HT. The results presented here suggest that chalcogenide aerogels are suitable candidates for optoelectronic devices, especially in applications where low amounts of inorganic phase are desired.

## CHAPTER 6

### CONCLUSIONS AND PROSPECTUS

#### 6.1 Conclusions

Chalcogenide nanocrystals (NCs) are of significant interest for a variety of optical and electronic device applications such as field-effect transistors (FETs),<sup>57, 58</sup> photodetectors,<sup>59, 60</sup> light emitting diodes (LEDs)<sup>61, 62</sup> and photovoltaics<sup>63, 64</sup> due to the dominance of quantum size effects in the electronic structure, which enables the optical properties to be tuned within the visible and near-IR regions, and solution processability, which allows thin film fabrication by low cost solution coating<sup>119</sup> or printing processes.<sup>120</sup> However, a key issue that must be addressed for their successful implementation is the enhancement of charge transport in NC assemblies that are utilized in device applications. Conductivity in NC assemblies, such as thin films, depends on the amount of electronic coupling between neighboring NCs so that charge transport can occur by sequential tunneling.<sup>65</sup> In the synthesis of these NCs, long chain aliphatic surfactant ligands are used to control the size and shape of the NCs and these bulky organic surfactants stabilize the NCs in solution by preventing aggregation. However in the solid state, the surfactants act as highly insulating barriers, reducing the interparticle coupling and consequently decreasing the conductivity and carrier mobility in NC assemblies. Currently, there is intensive research focusing on improving the conductivity and carrier mobility in chalcogenide NC assemblies by reducing the inter-NC spacing.<sup>124, 72</sup>

Brock et al. have used sol–gel methods to assemble metal chalcogenide NCs into gels, xerogels and aerogels.<sup>47, 49</sup> In this method NCs are connected through covalent bonding of anionic species (diselenide covalent linkages in the case of CdSe NCs) that are formed on the

surface during the gelation process<sup>56</sup> and this covalent linkage of discrete NCs into a network is expected to provide facile electronic communication between neighboring NCs.

The dissertation work focused on achieving two main goals: 1) optimization of gelation conditions in order to tune the properties of resultant gel structures with the aim of addressing application-specific needs; 2) incorporation of gel materials into device architectures and evaluation of their properties related to relevant applications. To achieve these goals, three specific aims were pursued.

Aim I. Ascertain the physical mechanism of gelation en route to controlling the optical quality of the gels (presented in Chapter 3)

Transparent CdSe/ZnS core/shell sol–gel materials have potential uses in optoelectronic applications such as light-emitting diodes (LEDs) due to their strong luminescence properties and the potential for charge transport through the prewired NC network of the gel.<sup>75</sup> However, typical syntheses of metal chalcogenide gels yield materials with poor transparency. According to studies done on the sol–gel transition of CdS NCs, the nature and concentration of the oxidant have considerable effect on the structure of the resultant CdS gel.<sup>50</sup> As described in Chapter 3 the macroscopic properties (i.e. transparency) of CdSe/ZnS gel structures were tuned by controlling the aggregation and gelation kinetics by means of oxidant concentration, sol concentration and primary particle size.

The mechanism and kinetics of aggregation of two sizes of 11-mercaptoundecanoic acid (MUA)-capped CdSe/ZnS NCs, initiated by removal of surface thiolate ligands using tetranitromethane (TNM) as an oxidant, were studied by means of time-resolved dynamic light scattering (TRDLS) at two different NC concentrations; the characteristics of the resultant gels were probed by optical transmission, transmission electron microscopy (TEM) and small angle

X-ray scattering (SAXS). At low concentrations of NCs (ca.  $4 \times 10^{-7}$  M), the smaller, green-emitting NCs aggregated faster than the larger, orange-emitting NCs, for a specific oxidant concentration. The kinetics of aggregation had a significant impact on the macroscopic properties of the resultant gels, with the transparency of the green-emitting gels decreasing with the increase of oxidant concentration due the formation of larger clusters at the gel point and a shift away from a reaction limited cluster aggregation (RLCA) mechanism. This was further confirmed by the analyses of the gel structures by SAXS and TEM. Moreover, a 10-fold increase in the green-emitting NC concentration resulted in opaque gel structures at any oxidant concentration. Likewise, the larger orange-emitting particles also produced larger aggregates at the gel point, leading to lower transparency. Based on this study, the critical factors for achieving transparent gels are; 1) small NC size ( $\sim 4.5$  nm); 2) relatively low NC concentration ( $\sim 4 \times 10^{-7}$  M); and 3) relatively low oxidant concentration ( $\sim 4\text{--}10$   $\mu\text{L}$ ). The ability to control the transparency of chalcogenide gels will enable their properties to be tuned in order to address application-specific needs in optoelectronics.

Aim II. Establish methods to prepare sol–gel films and determine their electro-optical properties (presented in Chapter 4)

Fabrication of gel materials in film form is one of the major steps towards incorporation of gel materials into device architectures. Evaluation of the charge transport properties of chalcogenide gel materials, which have never been studied, is also facilitated by production of a film. In Chapter 4, a significant step towards practical exploitation of chalcogenide gels by fabricating both micron-scale and nano-scale xerogel films is described.

The synthesis of transparent micron-thick xerogel films of CdSe/ZnS NCs was achieved by employing gelation conditions that resulted in transparent gel structures. Glass substrates

were immersed horizontally in pre-oxidized sols of CdSe/ZnS NCs and micron-thick xerogel films were deposited by gelling and drying under ambient conditions. Films had rough surface morphologies but exhibited strong photoluminescence and high conductivities ( $\sim 10^{-3} \text{ S}\cdot\text{cm}^{-1}$ ) which further confirmed the suitability of gel materials for optoelectronic applications.

Sol–gel thin film fabrication was achieved by dipping spin-coated sol films of thioglycolic acid-capped NCs (CdSe and CdSe/ZnS) into a solution of TNM in acetone. Mild annealing (250 °C for 30 minutes) was subsequently employed to remove the residual ligands after the gelation and cleaning steps. High-angle annular dark-field scanning transmission electron microscopy (HAADF-STEM) imaging of gelled CdSe NCs with chemical analysis confirmed that the surface and interparticle interfaces of the NCs are chalcogen-rich, consistent with an oxidative-induced gelation mechanism in which connectivity is achieved by formation of dichalcogenide covalent linkages between particles. Further enhancement of inter-particle coupling via mild thermal annealing, which removed residual ligands and reinforced NC connectivity, resulted in CdSe sol–gel thin films with superior charge transport properties, as shown by a dramatic enhancement of electrochemical photocurrent under white light illumination relative to thin films composed of ligand-capped CdSe NCs. The photocurrents of CdSe and CdSe/ZnS NCs were compared in order to investigate the effect of surface passivation. Removal of surface ligands during the gelation process can create surface defects on the CdSe surface, which can serve as electron and hole traps. As expected, a more than 2-fold enhancement in photocurrent, and a further increase in photovoltage were achieved by passivation of surface defects by overcoating CdSe core with a thin ZnS shell. The ability to tune interfacial and surface characteristics for the optimization of photophysical properties suggests

that the sol–gel approach may yield NC thin films suitable for a range of optoelectronic applications.

Aim III. Utilize chalcogenide gel materials to fabricate photovoltaic devices (presented in Chapter 5)

Increasing demand for inexpensive, reliable and renewable energy has motivated intense research in the field of photovoltaics. Bulk heterojunction (BHJ) solar cells are state-of-the-art organic solar cells, and so-called third generation photovoltaics.<sup>160</sup> BHJ solar cells consist of a solid dispersion of electron-donating and -accepting semiconductor polymers that creates a nanoscale, bicontinuous and interpenetrating network.<sup>161</sup> Excitons generated in the donor phase by absorption of light diffuse to the interface and dissociate into electrons and holes. After dissociation, electrons and holes travel to the respective electrodes through percolation pathways provided by the n-type and p-type polymer phases, respectively. However, the low electron mobility of the acceptor polymers, usually a fullerene derivative, ( $<10^{-4} \text{ cm}^2 \text{ V}^{-1} \text{ s}^{-1}$ ) is one of the major factors that limits the efficiency of the devices.<sup>162</sup> High electron affinity and mobility of inorganic semiconductor NCs make it possible to replace the organic fullerene derivative phase with an inorganic NC phase (e.g. CdSe,<sup>64, 159</sup> PbS<sup>163, 164</sup> or PbSe<sup>151</sup>) and create hybrid solar cells. Addition of the inorganic NC phase further contributes to the light absorption and thus generates more charge carriers. Band tunability of NCs enables adjustable absorption properties and consequently efficient light harvesting. However, efficiencies of these devices are still around 3%<sup>153</sup> mainly due to the typical poor charge transport properties of ligand-capped NCs.

Sol–gel chalcogenide materials have the potential to provide enhanced electronic conductivity via an interconnected chalcogenide network, making them a suitable candidate for hybrid photovoltaic applications. In Chapter 5, deposition of hybrid films of both CdSe and

CdSe/ZnS aerogel, and poly(3-hexylthiophene) (P3HT) was described, and the efficiency of charge generation and transport presented. The photocurrent response of aerogel/P3HT films was compared to films composed of P3HT and ligand-capped, physically aggregated NCs, under illumination of white light at different loadings. At lower loadings of nanomaterials, aerogel/P3HT hybrid films showed higher photocurrent and this confirms the efficiency of sol–gel methods to create NC assemblies with better charge transport properties. Furthermore, at any loading, CdSe/ZnS aerogel/P3HT films yield a higher photoresponse compared to that of CdSe aerogel/P3HT films, indicative of the importance of surface passivation.

## **6.2 Prospectus**

The dissertation research has provided fundamental insight into the conditions that are required to optimize the sol–gel process in order to tune the properties of resultant gel materials with the aim of addressing application-specific needs. Furthermore it has introduced strategies to incorporate gel materials into device architectures and provided evidence of suitability of sol–gel methods to form chalcogenide NC assemblies for optoelectronic applications. Thus, the future work should be focused on actual device fabrication.

The first attempts to make hybrid solar cells resulted in devices with poor performance due to the poor dispersion of aerogels in any solvent or solvent mixtures, making it hard to fabricate high quality hybrid films with uniformly dispersed inorganic and organic phases. Therefore, pre-pared aerogels may not be a suitable material for photovoltaic applications. However the dissertation work has introduced a successful strategy to fabricate high quality CdSe sol–gel thin films in ambient conditions, and these xerogel thin films exhibited promising photoresponse according to photoelectrochemical measurements, indicative of efficient charge transport in the NC network. Moreover, an inorganic surface passivation procedure (overcoating

the CdSe core with a thin ZnS shell) has been introduced in order to enhance the efficiency of charge carrier collection. Hence, CdSe/ZnS sol–gel films would be appropriate for fabrication of NC sensitized solar cells (Figure 6.1).

Poor charge transport in NC film is one of the major factors that contribute to the lower efficiency NC sensitized solar cells.<sup>15</sup> The sol–gel method introduced in Chapter 4 can be utilized to fabricate a photoanode of the solar cell. Layer-by-layer deposition of a CdSe/ZnS sol onto a nanocrystalline TiO<sub>2</sub> substrate by spin coating, followed by a gelation step for the formation of each layer, is expected to result in an interconnected network of NCs on the TiO<sub>2</sub> film. This could lead to an enhancement of solar cell efficiency due to the improvement in charge transport in NC film. As shown in Figure 6.1 photogenerated electrons in the NC film are expected to efficiently transport to the TiO<sub>2</sub> layer via the interconnected NC network, whereas holes are captured and transported to the counter electrode by sulfide/polysulfide electrolyte.

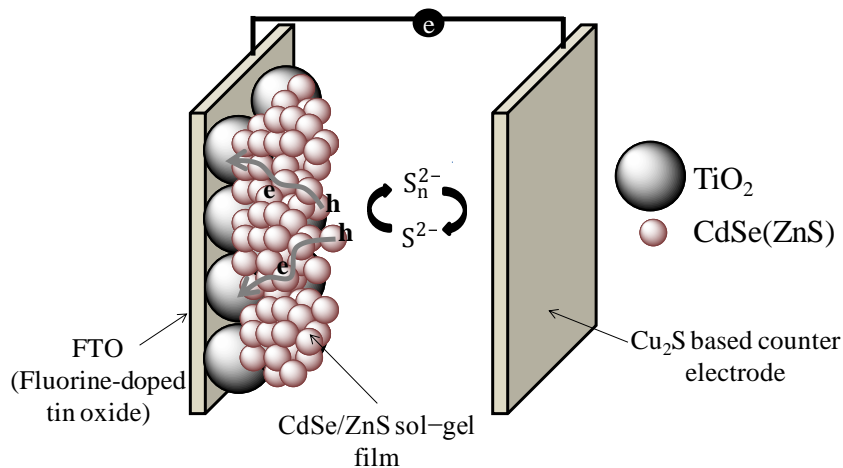


**Figure 6.1.** Schematic illustration of a NC sensitized solar cell (adapted from Kamat).<sup>15</sup>

The sol–gel film fabrication strategy can be extended to other chalcogenide NC systems, such as PbS. PbS NCs are particular of interest because of their ability to absorb both visible and near infrared light, which makes them one of the most desirable NC systems for solar energy harvesting. An appropriate photovoltaic type could be a depleted heterojunction NC solar cell in which PbS NC films are deposited on a  $\text{TiO}_2/\text{ZnO}$  substrate by the layer-by-layer spin coating/gelation process (Figure 6.2). According to preliminary studies, solution phase exchange of thioglycolic acid for PbS NCs is difficult because thioglycolic acid-capped PbS NCs are not stable in solution. However, ligand exchange can be successfully performed in the solid phase after depositing oleic acid-capped PbS NCs on the substrate. Gelation can subsequently be initiated by dipping the film in an oxidizing solution after the ligand exchange step. As in the CdSe case, suitable inorganic surface passivation is essential because removal of surface ligands creates trap states on the NC surface that reduces the efficiency of charge collection.

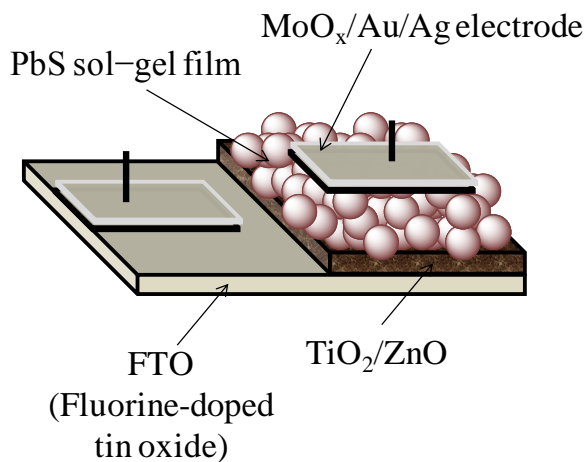


**Figure 6.2.** Schematic illustration of a depleted heterojunction NC solar cell (adapted from Sargent).<sup>165</sup>

In addition to fabrication of photovoltaic devices, examination of charge transport in sol–gel NC films in the solid state by fabricating field-effect transistors (FETs) is a fundamental prospective study. This will enable the basic electrical properties of sol–gel NC films to be assessed, such as conductivity and mobility, and also will provide insight into the mechanism of charge transport.

## REFERENCES

1. Yarema, M.; Pichler, S.; Sytnyk, M.; Seyrkammer, R.; Lechner, R. T.; Fritz-Popovski, G.; Jarzab, D.; Szendrei, K.; Resel, R.; Korovyanko, O.; Loi, M. A.; Paris, O.; Hesser, G.; Heiss, W., *ACS Nano* **2011**, *5* (5), 3758-3765.
2. Xie, R.; Zhang, J.; Zhao, F.; Yang, W.; Peng, X., *Chem. Mater.* **2010**, *22* (13), 3820-3822.
3. Harris, D. K.; Allen, P. M.; Han, H.-S.; Walker, B. J.; Lee, J.; Bawendi, M. G., *J. Am. Chem. Soc.* **2011**, *133* (13), 4676-4679.
4. Murray, C. B.; Norris, D. J.; Bawendi, M. G., *J. Am. Chem. Soc.* **1993**, *115* (19), 8706-8715.
5. Lhuillier, E.; Keuleyan, S.; Liu, H.; Guyot-Sionnest, P., *Chem. Mater.* **2013**.
6. Beberwyck, B. J.; Alivisatos, A. P., *J. Am. Chem. Soc.* **2012**, *134* (49), 19977-19980.
7. Battaglia, D.; Peng, X., *Nano Lett.* **2002**, *2* (9), 1027-1030.
8. Liu, W.; Chang, A. Y.; Schaller, R. D.; Talapin, D. V., *J. Am. Chem. Soc.* **2012**, *134* (50), 20258-20261.
9. Hines, M. A.; Scholes, G. D., *Adv. Mater.* **2003**, *15* (21), 1844-1849.
10. Talapin, D. V.; Murray, C. B., *Science* **2005**, *310* (5745), 86-89.
11. Urban, J. J.; Talapin, D. V.; Shevchenko, E. V.; Murray, C. B., *J. Am. Chem. Soc.* **2006**, *128* (10), 3248-3255.
12. Klimov, V. I., *Nanocrystal Quantum Dots*; CRC: Boca Raton 2010.
13. Shirasaki, Y.; Supran, G. J.; Bawendi, M. G.; Bulovic, V., *Nat. Photonics* **2013**, *7* (1), 13-23.
14. Konstantatos, G.; Sargent, E. H., *Infrared Phys. Technol.* **2011**, *54* (3), 278-282.

15. Kamat, P. V., *J. Phys. Chem. Lett.* **2013**, 908-918.
16. Alivisatos, A. P., *J. Phys. Chem.* **1996**, *100* (31), 13226-13239.
17. Qu, L.; Peng, Z. A.; Peng, X., *Nano Lett.* **2001**, *1* (6), 333-337.
18. Yin, Y.; Alivisatos, A. P., *Nature* **2005**, *437* (7059), 664-670.
19. Talapin, D. V.; Lee, J.-S.; Kovalenko, M. V.; Shevchenko, E. V., *Chem. Rev.* **2009**, *110* (1), 389-458.
20. Chen, Y.; Johnson, E.; Peng, X., *J. Am. Chem. Soc.* **2007**, *129* (35), 10937-10947.
21. Peng, Z. A.; Peng, X., *J. Am. Chem. Soc.* **2001**, *123* (7), 1389-1395.
22. Manna, L.; Scher, E. C.; Alivisatos, A. P., *J. Am. Chem. Soc.* **2000**, *122* (51), 12700-12706.
23. Cho, K.-S.; Talapin, D. V.; Gaschler, W.; Murray, C. B., *J. Am. Chem. Soc.* **2005**, *127* (19), 7140-7147.
24. Trentler, T. J.; Hickman, K. M.; Goel, S. C.; Viano, A. M.; Gibbons, P. C.; Buhro, W. E., *Science* **1995**, *270* (5243), 1791-1794.
25. Yu, H.; Buhro, W. E., *Adv. Mater.* **2003**, *15* (5), 416-419.
26. Yin, Y.; Rioux, R. M.; Erdonmez, C. K.; Hughes, S.; Somorjai, G. A.; Alivisatos, A. P., *Science* **2004**, *304* (5671), 711-714.
27. Sun, Y.; Xia, Y., *Science* **2002**, *298* (5601), 2176-2179.
28. Rivest, J. B.; Jain, P. K., *Chem. Soc. Rev.* **2013**, *42* (1), 89-96.
29. Casavola, M.; van Huis, M. A.; Bals, S.; Lambert, K.; Hens, Z.; Vanmaekelbergh, D., *Chem. Mater.* **2011**, *24* (2), 294-302.
30. Son, D. H.; Hughes, S. M.; Yin, Y.; Paul Alivisatos, A., *Science* **2004**, *306* (5698), 1009-1012.

31. Carbone, L.; Cozzoli, P. D., *Nano Today* **2010**, 5 (5), 449-493.
32. Hines, M. A.; Guyot-Sionnest, P., *J. Phys. Chem.* **1996**, 100 (2), 468-471.
33. Talapin, D. V.; Mekis, I.; Götzinger, S.; Kornowski, A.; Benson, O.; Weller, H., *J. Phys. Chem. B* **2004**, 108 (49), 18826-18831.
34. Carbone, L.; Nobile, C.; De Giorgi, M.; Sala, F. D.; Morello, G.; Pompa, P.; Hytch, M.; Snoeck, E.; Fiore, A.; Franchini, I. R.; Nadasan, M.; Silvestre, A. F.; Chiodo, L.; Kudera, S.; Cingolani, R.; Krahne, R.; Manna, L., *Nano Lett.* **2007**, 7 (10), 2942-2950.
35. Kudera, S.; Carbone, L.; Casula, M. F.; Cingolani, R.; Falqui, A.; Snoeck, E.; Parak, W. J.; Manna, L., *Nano Lett.* **2005**, 5 (3), 445-449.
36. Fiore, A.; Mastria, R.; Lupo, M. G.; Lanzani, G.; Giannini, C.; Carlino, E.; Morello, G.; De Giorgi, M.; Li, Y.; Cingolani, R.; Manna, L., *J. Am. Chem. Soc.* **2009**, 131 (6), 2274-2282.
37. Mokari, T.; Rothenberg, E.; Popov, I.; Costi, R.; Banin, U., *Science* **2004**, 304 (5678), 1787-1790.
38. Milliron, D. J.; Hughes, S. M.; Cui, Y.; Manna, L.; Li, J.; Wang, L.-W.; Paul Alivisatos, A., *Nature* **2004**, 430 (6996), 190-195.
39. Jain, P. K.; Amirav, L.; Aloni, S.; Alivisatos, A. P., *J. Am. Chem. Soc.* **2010**, 132 (29), 9997-9999.
40. Robinson, R. D.; Sadtler, B.; Demchenko, D. O.; Erdonmez, C. K.; Wang, L.-W.; Alivisatos, A. P., *Science* **2007**, 317 (5836), 355-358.
41. Zhang, J. Z., *Optical Properties and Spectroscopy of Nanomaterials*; World Scientific: Hackensack, 2009.
42. Smith, A. M.; Nie, S., *Acc. Chem. Res.* **2009**, 43 (2), 190-200.

43. Norris, D. J.; Bawendi, M. G., *Phys. Rev. B* **1996**, *53* (24), 16338-16346.
44. Klimov, V. I., *Annu. Rev. Phys. Chem.* **2007**, *58* (1), 635-673.
45. Underwood, D. F.; Kippeny, T.; Rosenthal, S. J., *J. Phys. Chem. B* **2000**, *105* (2), 436-443.
46. Li, J. J.; Wang, Y. A.; Guo, W.; Keay, J. C.; Mishima, T. D.; Johnson, M. B.; Peng, X., *J. Am. Chem. Soc.* **2003**, *125* (41), 12567-12575.
47. Mohanan, J. L.; Arachchige, I. U.; Brock, S. L., *Science* **2005**, *307* (5708), 397-400.
48. Burda, C.; Chen, X.; Narayanan, R.; El-Sayed, M. A., *Chem. Rev.* **2005**, *105* (4), 1025-1102.
49. Arachchige, I. U.; Brock, S. L., *Acc. Chem. Res.* **2007**, *40* (9), 801-809.
50. Gacoin, T.; Lahlil, K.; Larregaray, P.; Boilot, J. P., *J. Phys. Chem. B* **2001**, *105* (42), 10228-10235.
51. Arachchige, I. U.; Brock, S. L., *J. Am. Chem. Soc.* **2006**, *128* (24), 7964-7971.
52. Yao, Q.; Brock, S. L., *Inorg. Chem.* **2011**, *50* (20), 9985-9992.
53. Kalebaila, K. K.; Brock, S. L., *Z. Anorg. Allg. Chem.* **2012**, *638* (15), 2598-2603.
54. Ganguly, S.; Brock, S. L., *J. Mater. Chem.* **2011**, *21* (24), 8800-8806.
55. Ganguly, S.; Zhou, C.; Morelli, D.; Sakamoto, J.; Brock, S. L., *J. Phys. Chem. C* **2012**, *116* (33), 17431-17439.
56. Pala, I. R.; Arachchige, I. U.; Georgiev, D. G.; Brock, S. L., *Angew. Chem. Int. Ed.* **2010**, *49* (21), 3661-3665.
57. Yu, D.; Wang, C.; Guyot-Sionnest, P., *Science* **2003**, *300* (5623), 1277-1280.
58. Ridley, B. A.; Nivi, B.; Jacobson, J. M., *Science* **1999**, *286* (5440), 746-749.

59. Oertel, D. C.; Bawendi, M. G.; Arango, A. C.; Bulovic, V., *Appl. Phys. Lett.* **2005**, *87* (21), 213505.
60. Konstantatos, G.; Howard, I.; Fischer, A.; Hoogland, S.; Clifford, J.; Klem, E.; Levina, L.; Sargent, E. H., *Nature* **2006**, *442* (7099), 180-183.
61. Colvin, V. L.; Schlamp, M. C.; Alivisatos, A. P., *Nature* **1994**, *370* (6488), 354-357.
62. Coe, S.; Woo, W.-K.; Bawendi, M.; Bulovic, V., *Nature* **2002**, *420* (6917), 800-803.
63. Gur, I.; Fromer, N. A.; Geier, M. L.; Alivisatos, A. P., *Science* **2005**, *310* (5747), 462-465.
64. Huynh, W. U.; Dittmer, J. J.; Alivisatos, A. P., *Science* **2002**, *295* (5564), 2425-2427.
65. Vanmaekelbergh, D.; Liljeroth, P., *Chem. Soc. Rev.* **2005**, *34* (4), 299-312.
66. Zabet-Khosousi, A.; Trudeau, P.-E.; Suganuma, Y.; Dhirani, A.-A.; Statt, B., *Phys. Rev. Lett.* **2006**, *96* (15), 156403.
67. Zabet-Khosousi, A.; Dhirani, A.-A., *Chem. Rev.* **2008**, *108* (10), 4072-4124.
68. Morgan, N. Y.; Leatherdale, C. A.; Drndić, M.; Jarosz, M. V.; Kastner, M. A.; Bawendi, M., *Phys. Rev. B* **2002**, *66* (7), 075339.
69. Ginger, D. S.; Greenham, N. C., *J. Appl. Phys.* **2000**, *87* (3), 1361-1368.
70. Yu, D.; Wang, C.; Wehrenberg, B. L.; Guyot-Sionnest, P., *Phys. Rev. Lett.* **2004**, *92* (21), 216802.
71. Lee, J.-S.; Kovalenko, M. V.; Huang, J.; Chung, D. S.; Talapin, D. V., *Nat. Nanotechnol.* **2011**, *6* (6), 348-352.
72. Fafarman, A. T.; Koh, W.-K.; Diroll, B. T.; Kim, D. K.; Ko, D.-K.; Oh, S. J.; Ye, X.; Doan-Nguyen, V.; Crump, M. R.; Reifsnyder, D. C.; Murray, C. B.; Kagan, C. R., *J. Am. Chem. Soc.* **2011**, *133* (39), 15753-15761.

73. Arachchige, I. U.; Brock, S. L., *Acc. Chem. Res.* **2007**, *40* (9), 801-809.
74. Gaponik, N.; Herrmann, A.-K.; Eychemüller, A., *J. Phys. Chem. Lett.* **2012**, *3* (1), 8-17.
75. Arachchige, I. U.; Brock, S. L., *J. Am. Chem. Soc.* **2007**, *129* (7), 1840-1841.
76. Gacoin, T.; Lahlil, K.; Larregaray, P.; Boilot, J. P., *J. Phys. Chem. B* **2001**, *105* (42), 10228-10235.
77. Sargent, E. H., *Nat. Photonics* **2012**, *6* (3), 133-135.
78. Brinker, C. J.; Scherer, G. W., *Sol-gel Science : The Physics and Chemistry of Sol-gel Processing*; Academic: Boston, 1990.
79. Xu, R., *Particle Characterization: Light Scattering Methods*; Kluwer: New York, 2002.
80. Berne, B. J.; Pecora, R., *Dynamic Light Scattering: With Applications to Chemistry, Biology, and Physics*; Dover: New York, 2000.
81. Brown, W., *Dynamic Light Scattering: The Method and Some Applications*; Clarendon: New York, 1993.
82. Koppel, D. E., *J. Chem. Phys.* **1972**, *57* (11), 4814-4820.
83. Pecharsky, V. K.; Zavalij, P. Y., *Fundamentals of Powder Diffraction and Structural Characterization of Materials*; Kluwer: Boston, 2003.
84. Borchert, H.; Shevchenko, E. V.; Robert, A.; Mekis, I.; Kornowski, A.; Grübel, G.; Weller, H., *Langmuir* **2005**, *21* (5), 1931-1936.
85. GuoZhong, C., *Nanostructures & Nanomaterials: Synthesis, Properties & Applications*; Imperial College: London, 2004.
86. Glatter, O.; Kratky, O., *Small Angle X-ray Scattering*; Academic: New York, 1982.
87. Feigin, L. A.; Svergun, D. I., *Structure Analysis by Small-angle X-ray and Neutron Scattering*; Plenum: New York, 1987.

88. Murray, C. B.; Kagan, C. R.; Bawendi, M. G., *Annu. Rev. Mater. Sci.* **2000**, *30*, 545-610.
89. Goodhew, P. J.; Humphreys, J.; Beanland, R., *Electron Microscopy and Analysis*; Taylor & Francis: London, 2001
90. Urban, K. W., *Science* **2008**, *321* (5888), 506-510.
91. Drelich, J.; Mittal, K. L., *Atomic Force Microscopy in Adhesion Studies*; VSP: Boston, 2005.
92. Zhang, J. Z., *Optical Properties and Spectroscopy of Nanomaterials*; World Scientific: Hackensack, 2009.
93. Pesika, N. S.; Stebe, K. J.; Searson, P. C., *Adv. Mater.* **2003**, *15* (15), 1289-1291.
94. Brus, L., *J. Phys. Chem.* **1986**, *90* (12), 2555-2560.
95. Lakowicz, J. R., *Principles of Fluorescence Spectroscopy*; Springer: New York, 2006.
96. Stuart, B. H., *Infrared Spectroscopy: Fundamentals and Applications*; Wiley: Hoboken, 2004.
97. Van der Pauw, L. J., *Philips Tech. Rev.* **1958**, *20*, 220-224.
98. Bard, A. J.; Faulkner, L. R., *Electrochemical Methods: Fundamentals and Applications* Wiley: New York, 2004.
99. van der Krol, R.; Grätzel, M., *Photoelectrochemical Hydrogen Production*; Springer: New York, 2012.
100. Peng, Z. A.; Peng, X., *J. Am. Chem. Soc.* **2001**, *123* (1), 183-184.
101. Qu, L.; Peng, X., *J. Am. Chem. Soc.* **2002**, *124* (9), 2049-2055.
102. Lin, M. Y.; Lindsay, H. M.; Weitz, D. A.; Ball, R. C.; Klein, R.; Meakin, P., *Nature* **1989**, *339* (6223), 360-362.

103. Lin, M. Y.; Lindsay, H. M.; Weitz, D. A.; Ball, R. C.; Klein, R.; Meakin, P., *Phys. Rev. A* **1990**, *41* (4), 2005-2020.
104. Lin, M. Y.; Lindsay, H. M.; Weitz, D. A.; Klein, R.; Ball, R. C.; Meakin, P., *J. Phys. Condens. Matter* **1990**, *2* (13), 3093.
105. Umbach, P.; Georgalis, Y.; Saenger, W., *J. Am. Chem. Soc.* **1998**, *120* (10), 2382-2390.
106. Hanus, L. H.; Sooklal, K.; Murphy, C. J.; Ploehn, H. J., *Langmuir* **2000**, *16* (6), 2621-2626.
107. Jasmine, M. J.; Prasad, E., *J. Phys. Chem. B* **2010**, *114* (23), 7735-7742.
108. Yu, W. W.; Qu, L.; Guo, W.; Peng, X., *Chem. Mater.* **2003**, *15* (14), 2854-2860.
109. Burns, J. L.; Yan, Y.-d.; Jameson, G. J.; Biggs, S., *Langmuir* **1997**, *13* (24), 6413-6420.
110. Shibayama, M.; Norisuye, T., *Bull. Chem. Soc. Jpn.* **2002**, *75* (4), 641-659.
111. Shibayama, M., *Bull. Chem. Soc. Jpn.* **2006**, *79* (12), 1799-1819.
112. Martin, J. E.; Wilcoxon, J. P., *Phys. Rev. Lett.* **1988**, *61* (3), 373.
113. Martin, J. E.; Wilcoxon, J.; Odinek, J., *Phys. Rev. A* **1991**, *43* (2), 858.
114. Miyazaki, S.; Endo, H.; Karino, T.; Haraguchi, K.; Shibayama, M., *Macromolecules* **2007**, *40* (12), 4287-4295.
115. Schaefer, D. W.; Keefer, K. D., *Phys. Rev. Lett.* **1984**, *53* (14), 1383.
116. Vacher, R.; Woignier, T.; Pelous, J.; Courtens, E., *Phys. Rev. B* **1988**, *37* (11), 6500-6503.
117. Emmerling, A.; Petricevic, R.; Beck, A.; Wang, P.; Scheller, H.; Fricke, J., *J. Non-Cryst. Solids* **1995**, *185* (3), 240-248.
118. Beurroies, I.; Duffours, L.; Delord, P.; Woignier, T.; Phalippou, J., *J. Non-Cryst. Solids* **1998**, *241* (1), 38-44.

119. Luther, J. M.; Law, M.; Song, Q.; Perkins, C. L.; Beard, M. C.; Nozik, A. J., *ACS Nano* **2008**, *2* (2), 271-280.
120. Haverinen, H. M.; Myllyla, R. A.; Jabbour, G. E., *Appl. Phys. Lett.* **2009**, *94* (7), 073108.
121. Law, M.; Luther, J. M.; Song, Q.; Hughes, B. K.; Perkins, C. L.; Nozik, A. J., *J. Am. Chem. Soc.* **2008**, *130* (18), 5974-5985.
122. Drndic, M.; Jarosz, M. V.; Morgan, N. Y.; Kastner, M. A.; Bawendi, M. G., *J. Appl. Phys.* **2002**, *92* (12), 7498-7503.
123. Dong, A.; Ye, X.; Chen, J.; Kang, Y.; Gordon, T.; Kikkawa, J. M.; Murray, C. B., *J. Am. Chem. Soc.* **2010**, *133* (4), 998-1006.
124. Kovalenko, M. V.; Scheele, M.; Talapin, D. V., *Science* **2009**, *324* (5933), 1417-1420.
125. Kovalenko, M. V.; Bodnarchuk, M. I.; Zaumseil, J.; Lee, J.-S.; Talapin, D. V., *J. Am. Chem. Soc.* **2010**, *132* (29), 10085-10092.
126. Lee, J.-S.; Kovalenko, M. V.; Huang, J.; Chung, D. S.; Talapin, D. V., *Nat. Nanotechnol.* **2011**, *6* (6), 348-352.
127. Nag, A.; Kovalenko, M. V.; Lee, J.-S.; Liu, W.; Spokoyny, B.; Talapin, D. V., *J. Am. Chem. Soc.* **2011**, *133* (27), 10612-10620.
128. Zhang, H.; Hu, B.; Sun, L.; Hovden, R.; Wise, F. W.; Muller, D. A.; Robinson, R. D., *Nano Lett.* **2011**, *11* (12), 5356-5361.
129. Yu, D.; Wehrenberg, B. L.; Jha, P.; Ma, J.; Guyot-Sionnest, P., *J. Appl. Phys.* **2006**, *99* (10), 104315.
130. Jarosz, M. V.; Porter, V. J.; Fisher, B. R.; Kastner, M. A.; Bawendi, M. G., *Phys. Rev. B* **2004**, *70* (19), 195327.

131. Talgorn, E.; Moysidou, E.; Abellon, R. D.; Savenije, T. J.; Goossens, A.; Houtepen, A. J.; Siebbeles, L. D. A., *J. Phys. Chem. C* **2010**, *114* (8), 3441-3447.
132. Klem, E. J. D.; Shukla, H.; Hinds, S.; MacNeil, D. D.; Levina, L.; Sargent, E. H., *Appl. Phys. Lett.* **2008**, *92* (21), 212105.
133. Lefrancois, A.; Couderc, E.; Faure-Vincent, J.; Sadki, S.; Pron, A.; Reiss, P., *J. Mater. Chem.* **2011**, *21* (31), 11524-11531.
134. Zarghami, M. H.; Liu, Y.; Gibbs, M.; Gebremichael, E.; Webster, C.; Law, M., *ACS Nano* **2010**, *4* (4), 2475-2485.
135. Gaponik, N.; Wolf, A.; Marx, R.; Lesnyak, V.; Schilling, K.; Eychmüller, A., *Adv. Mater.* **2008**, *20* (22), 4257-4262.
136. Jasieniak, J.; Smith, L.; Embden, J. v.; Mulvaney, P.; Califano, M., *J. Phys. Chem. C* **2009**, *113* (45), 19468-19474.
137. Wuister, S. F.; de Mello Donegá, C.; Meijerink, A., *J. Phys. Chem. B* **2004**, *108* (45), 17393-17397.
138. Williams, K. J.; Tisdale, W. A.; Leschkies, K. S.; Haugstad, G.; Norris, D. J.; Aydil, E. S.; Zhu, X. Y., *ACS Nano* **2009**, *3* (6), 1532-1538.
139. Artemyev, M. V.; Woggon, U.; Jaschinski, H.; Gurinovich, L. I.; Gaponenko, S. V., *J. Phys. Chem. B* **2000**, *104* (49), 11617-11621.
140. Webber, D. H.; Brutchey, R. L., *J. Am. Chem. Soc.* **2011**, *134* (2), 1085-1092.
141. Porter, V. J.; Geyer, S.; Halpert, J. E.; Kastner, M. A.; Bawendi, M. G., *J. Phys. Chem. C* **2008**, *112* (7), 2308-2316.
142. Sambur, J. B.; Parkinson, B. A., *J. Am. Chem. Soc.* **2010**, *132* (7), 2130-2131.
143. Shen, Q.; Kobayashi, J.; Diguna, L. J.; Toyoda, T., *J. Appl. Phys* **2008**, *103* (8), 084304.

144. Zhu, H.; Song, N.; Lian, T., *J. Am. Chem. Soc.* **2010**, *132* (42), 15038-15045.
145. Dias, E. A.; Sewall, S. L.; Kambhampati, P., *J. Phys. Chem. C* **2006**, *111* (2), 708-713.
146. Makhil, A.; Yan, H.; Lemmens, P.; Pal, S. K., *J. Phys. Chem. C* **2009**, *114* (1), 627-632.
147. Liang, Y.; Xu, Z.; Xia, J.; Tsai, S.-T.; Wu, Y.; Li, G.; Ray, C.; Yu, L., *Adv. Mater.* **2010**, *22* (20), E135-E138.
148. Saunders, B. R.; Turner, M. L., *Adv. Colloid Interface Sci.* **2008**, *138* (1), 1-23.
149. Sun, B.; Greenham, N. C., *Phys. Chem. Chem. Phys.* **2006**, *8* (30), 3557-3560.
150. Arici, E.; Hoppe, H.; Schäffler, F.; Meissner, D.; Malik, M. A.; Sariciftci, N. S., *Thin Solid Films* **2004**, *451-452* (0), 612-618.
151. McDonald, S. A.; Konstantatos, G.; Zhang, S.; Cyr, P. W.; Klem, E. J. D.; Levina, L.; Sargent, E. H., *Nat. Mater.* **2005**, *4* (2), 138-142.
152. Cui, D.; Xu, J.; Zhu, T.; Paradee, G.; Ashok, S.; Gerhold, M., *Appl. Phys. Lett.* **2006**, *88* (18), 183111.
153. Dayal, S.; Kopidakis, N.; Olson, D. C.; Ginley, D. S.; Rumbles, G., *Nano Lett.* **2009**, *10* (1), 239-242.
154. Wu, Y.; Zhang, G., *Nano Lett.* **2010**, *10* (5), 1628-1631.
155. Radychev, N.; Lokteva, I.; Witt, F.; Kolny-Olesiak, J.; Borchert, H.; Parisi, J. R., *J. Phys. Chem. C* **2011**, *115* (29), 14111-14122.
156. Seo, J.; Kim, W. J.; Kim, S. J.; Lee, K.-S.; Cartwright, A. N.; Prasad, P. N., *Appl. Phys. Lett.* **2009**, *94* (13), 133302.
157. Zhou, Y.; Riehle, F. S.; Yuan, Y.; Schleiermacher, H.-F.; Niggemann, M.; Urban, G. A.; Kruger, M., *Appl. Phys. Lett.* **2010**, *96* (1), 013304.
158. Mohanan, J.; Brock, S., *J. Sol-Gel Sci. Technol.* **2006**, *40* (2-3), 341-350.

159. Greenham, N. C.; Peng, X.; Alivisatos, A. P., *Phys. Rev. B* **1996**, *54* (24), 17628-17637.
160. Green, M. A. *Conference Record of the 2006 IEEE 4th World Conference* **2006**, 15-19.
161. Günes, S.; Neugebauer, H.; Sariciftci, N. S., *Chem. Rev.* **2007**, *107* (4), 1324-1338.
162. Kumar, S.; Scholes, G. D., *Microchim. Acta.* **2008**, *160* (3), 315-325.
163. Günes, S.; Neugebauer, H.; Sariciftci, N. S., *Chem. Rev.* **2007**, *107* (4), 1324-1338.
164. Watt, A.; Eichmann, T.; Rubinsztein-Dunlop, H.; Meredith, P., *Appl. Phys. Lett.* **2005**, *87* (25), 253109.
165. Ip, A. H.; Thon, S. M.; Hoogland, S.; Voznyy, O.; Zhitomirsky, D.; Debnath, R.; Levina, L.; Rollny, L. R.; Carey, G. H.; Fischer, A.; Kemp, K. W.; Kramer, I. J.; Ning, Z.; Labelle, A. J.; Chou, K. W.; Amassian, A.; Sargent, E. H., *Nat. Nanotechno.* **2012**, *7* (9), 577-582.

**ABSTRACT****CHALCOGENIDE SOL–GEL ASSEMBLY: CONTROLLING THE KINETICS OF NANOCRYSTAL AGGREGATION AND FILM FORMATION FOR APPLICATIONS IN OPTOELECTRONICS**

by

**LASANTHA KORALA****August 2013****Advisor:** Dr. Stephanie L. Brock**Major:** Chemistry (Inorganic)**Degree:** Doctor of Philosophy

The dissertation work is focused on 1) optimization of gelation conditions in order to tune the properties of the resultant gel structures with the aim of addressing application-specific needs; 2) incorporation of gel materials into device architectures for evaluation of intrinsic properties and assessment of suitability for optoelectronic applications.

Sol–gel assembly of CdSe/ZnS core/shell NCs typically results in opaque gel materials, which is one of the major obstacles for their use in optoelectronic applications such as LEDs. Macroscopic properties (i.e. transparency) of CdSe/ZnS gel structures were tuned by controlling the aggregation and gelation kinetics by means of oxidant concentration. The mechanism and kinetics of aggregation of 11-mercaptoundecanoic acid (MUA)-capped CdSe/ZnS NCs, as a function of oxidant concentration [tetranitromethane, (TNM)], were studied by means of time resolved dynamic light scattering (TRDLS). The structural characteristics of the resultant gels were probed by optical transmission, transmission electron microscopy (TEM), and small-angle X-ray scattering (SAXS). Transparent gel structures were achieved for small NCs (~4.5 nm) at

relatively low NC concentration ( $\sim 4 \times 10^{-7}$  M) and oxidant concentration ( $\sim 4\text{--}10$   $\mu\text{L}$ ) enabling the tuning of macroscopic properties for application-specific needs in optoelectronics.

In order to incorporate chalcogenide gel materials into device architectures, it is essential to fabricate gel materials in film form. The synthesis of transparent micron-thick xerogel films of CdSe/ZnS NCs was achieved by employing gelation conditions that resulted in transparent gel structures. Films were deposited by immersing a glass substrate horizontally in the pre-oxidized sols, gelling and drying under ambient conditions. CdSe/ZnS xerogel films exhibited strong photoluminescence and high conductivities ( $\sim 10^{-3}$  S $\cdot\text{cm}^{-1}$ ). However, the films were rough, and attempts to make crack-free thinner films by this approach were not successful.

High quality thin (ca 70 nm) sol–gel NC films were deposited by spin coating sols of thioglycolic acid-capped CdSe and CdSe/ZnS NCs onto substrates and dipping the films into an oxidizing solution (TNM in acetone). Optical, structural and electrical properties of the sol–gel films were evaluated and the films were found to exhibit superior charge transport properties, as shown by a dramatic enhancement of electrochemical photocurrent under white light illumination relative to thin films composed of ligand-capped NCs. This suggests that the sol–gel approach may yield NC thin films suitable for a range of optoelectronic applications.

Composite films of poly(3-hexylthiophene) (P3HT) with either CdSe and CdSe/ZnS aerogels, were evaluated for hybrid photovoltaic devices by analyzing the variation of morphology and photocurrent generation with the composition of the hybrid film. Compared to films composed of ligand-capped, physically aggregated NCs and P3HT, aerogel/P3HT films showed increased photocurrent and charge generation attributed to the interconnected NC network. These data suggest that the use of chalcogenide aerogel materials for hybrid photovoltaic applications is feasible.

**AUTOBIOGRAPHICAL STATEMENT****LASANTHA KORALA****Education**

- **2008–2013 Ph.D.** Inorganic Chemistry, Wayne State University, Detroit, MI  
Dissertation: Chalcogenide Sol–gel Assembly: Controlling the Kinetics of Nanocrystal Aggregation and Film Formation for Applications in Optoelectronics  
Advisor: Prof. Stephanie L. Brock
- **2003–2007 B.S.** (honors) in Chemistry, University of Kelaniya, Sri Lanka

**Research and Teaching Experience**

- **01/2011–05/2013** Graduate Research Assistant, Department of Chemistry, Wayne State University, Detroit, MI
- **08/208–12/2010** Graduate Teaching Assistant, Department of Chemistry, Wayne State University, Detroit, MI
- **05/2007–05/2008** Graduate Teaching Assistant, Department of Chemistry, University of Kelaniya, Sri Lanka

**Awards and Fellowships**

- Esther and Stanley Kirschner Graduate Inorganic Chemistry Award, 2013
- ACS Division of Inorganic Chemistry Travel Award, Spring 2013
- Schaap Graduate Student Fellowship, 2012-2013

**Publications**

- **Korala, L.**; Wang, Z.; Liu, Y.; Maldonado, S.; Brock, S. L. Uniform Thin Films of CdSe and CdSe/ZnS Core/shell Quantum Dots by Sol–gel Assembly: Enabling Photoelectrochemical Characterization and Electronic Applications. *ACS Nano* **2013**, *7*, 1215-1223.
- **Korala, L.**; Li, L.; Brock, S. L. Transparent Conducting Films of CdSe/ZnS Core/shell Quantum Dot Xerogels. *Chem. Commun.* **2012**, *48*, 8523-8525.
- **Korala, L.**; Brock, S. L. Aggregation Kinetics of Metal Chalcogenide Nanocrystals: Generation of Transparent CdSe/ZnS Core/shell Gels. *J. Phys. Chem. C* **2012**, *116*, 17110-17117.
- De Freitas, J. N.; **Korala, L.**; Reynolds, L. X.; Haque, S. A.; Brock, S. L.; Nogueira, A. F. Connecting the (Quantum) Dots: Toward Hybrid Photovoltaic Devices Based on Chalcogenide Gels. *Phys. Chem. Chem. Phys.* **2012**, *14*, 15180-15184.
- De Freitas, J. N.; Alves, J. P. C.; **Korala, L.**; Brock, S. L.; Nogueira, A. F. Hybrid Photovoltaic Devices Based on Chalcogenide Nanostructures. *Proc. of SPIE* **2012**, 847711.